Electromagnetic Dimensionality of Deterministic Multi-Polarization MIMO Systems

by

Michel Elnaggar

A thesis
presented to the University of Waterloo
in fulfillment of the
thesis requirement for the degree of
Doctor of Philosophy
in
Electrical and Computer Engineering

Waterloo, Ontario, Canada, 2007

I hereby declare that I am the sole author of this thesis. This is a true copy of the thesis, including any required final revisions, as accepted by my examiners.

I understand that my thesis may be made electronically available to the public.

Abstract

Multiple-Input Multiple-Output (MIMO) systems are viewed as the last available supply for the ever-growing demand on higher data rates in modern wireless communication systems. Smart exploitation of the traditional wireless resources (time-slots or bandwidth under the same transmit power level) has reached its saturation point. By making better use of the free space between the radio links, based on the multipath radio wave propagation, MIMO systems have shown significant capacity improvement with the same traditional wireless resources.

In this multi-disciplinary research, we are exploring the link between the electromagnetic propagation and the information theory. Unlike the majority of recent research work, we model the propagation channel matrix between the transmit/receive elements in a deterministic manner under the Maxwellian framework. Having included the environment properties and the characteristics of the radiating elements, the deterministic approach provides a realistic assessment of the MIMO system performance in specific scenarios. The problem addressed in this research is the evaluation of the multi-antenna systems degrees of freedom (DOF) by employing all the available electromagnetic diversity resources (spatial, pattern and polarization).

Based on a developed well-defined power independent dimensionality (PID) metric, we start by investigating the information-bearing potential of the collocated multi-polarization MIMO system. We study the hexapole system (exploiting both electric and magnetic fields in conveying independent information) and compare it to the tripole systems (exploiting the vectorial polarization diversity of one field only). We present numerical results for 3

deterministic scenarios: a canonical free-space (near and far field exact solution), a canonical perfect electric conductor (PEC) corridor using rigorous modal analysis, and a lossy-wall corridor using image ray tracing (IRT).

Next, we provide deterministic results for the more interesting sampling problem of the electromagnetic vector fields: given a specific MIMO array size, what is the optimum number of packed multi-polarization antennas (i.e. multi-polarization 1D, 2D or 3D sampling) that yields the largest PID for a given environment and what is the estimate of this PID? Using a canonical case of multi-polarized arrays inside a multipath-rich PEC corridor, we show that the spatial frequency spectrum of the electromagnetic field governs the optimum PID of the site-specific scenario. The problem is analogous to the DOF determination of an essentially time-limited-band-limited 1D scalar function using the framework of the prolate spheroidal wave functions. We also present simulation results for the same sampling problem in a lossy-wall indoor environment using IRT.

Acknowledgements

I would like to thank my co-supervisors Profs Sujeet K. Chaudhuri and Safieddin Safavi-Naeini for giving me the opportunity to pursue my graduate studies at the University of Waterloo under their supervision. I also wish to thank my Ph.D. committee members Prof. Achim Kempf for the fruitful dimensionality and multi-polarization discussions, Profs Tapan Sarkar, Raafat Mansour and Murat Uysal for taking the time to examine the thesis and for their constructive feedback. Many thanks go to Prof. Hyo Eom for his time regarding the electromagnetic boundary-value problems and Prof. Liang-Liang Xie for the insightful MIMO dimensionality discussions. It was a pleasure to have frequent discussions with Dr. Chandra Kudsia and to assist him in his book.

I am grateful to all who financially supported this work: NSERC scholarship, CITO, RIM, and awards from UW and the ECE department. Thank you to all the administrative staff as well as the technical and support staff for their tireless effort. I wish also to thank the library and interlibrary loan staff for their indispensable services. Thank you to my colleagues and friends inside and outside Waterloo (the list is so long) who made my learning and social experience enjoyable.

My everlasting gratitude goes to my family for their love and support. I will always be indebted to them for all my achievements. Last, but definitely not least, thank you my Lord, you are always watching over me.

"*Thou hast beset me behind and before, and laid thine hand upon me.*
Such knowledge is too wonderful for me; it is high, I cannot attain unto it."
(Ps. 139)

To my beloved great family

Table of Contents

List of Tables

List of Figures

Chapter 1
Introduction

1.1 Basic Information

The advance in the successful applications of wireless communications puts a persistently growing demand on the wireless physical layer resources in order to achieve higher data rates. The traditional smart management techniques of the wireless resources (time-slots, bandwidth and transmit power level) have been exhausted. The last frontier remaining as a new physical layer resource is Space, which is essentially based on smart exploitation of the multipath propagation.

Multipath radio propagation has long been viewed as an adverse phenomenon for wireless communications. This view has been established because multipath propagation leads to fading when the wireless system is Single-Input Single-Output (SISO) i.e. having only one radiator at either ends. Fortunately, the situation is greatly improved once a Multiple-Input Multiple-Output (MIMO) system is employed [Win87, Tel95, Fos96, FG98, RC98, Mar01]. Employing multiple antennas at both ends has been shown to provide

"multiple spatial data modes" [PGN03] (which we call throughout this thesis the *parallel sub-channels*) between the transmit/receive ends while using the same traditional wireless resources.

A well-established metric for the MIMO channel performance is the channel capacity (evaluated in bit/sec/Hz), which is the general case of the Shannon SISO channel capacity [CT91, JW04]. For a multi-antenna system of (N_R, N_T) receive and transmit antennas, respectively, the propagation environment is modeled by the channel matrix $\mathbf{H} \in \mathbb{C}^{N_R \times N_T}$. Each entry h_{mn} represents the response at the m^{th} receive to the excitation at the n^{th} transmit. The input-output relation has the form

$$\mathbf{y}(f) = \mathbf{H}(f)\mathbf{x}(f) + \boldsymbol{\eta}(f), \tag{1.1}$$

where $\mathbf{y} \in \mathbb{C}^{N_R \times 1}$ and $\mathbf{x} \in \mathbb{C}^{N_T \times 1}$ are the receive and transmit signal vectors, respectively, $\boldsymbol{\eta} \in \mathbb{C}^{N_R \times 1}$ is the additive noise vector at the receive end and f is the temporal frequency. The following assumptions are made [JW04]:

- The system operates in narrowband (flat fading within the frequency band of operation), therefore we omit the frequency dependence from (1.1).
- $\mathbf{x}$ has Gaussian independent identically distributed (iid) elements. Therefore, the unencoded transmit vector elements are independent.
- $\boldsymbol{\eta}$ has Gaussian iid elements.
- $\mathbf{H}$ is normalized such that its Frobenius norm is $\|\mathbf{H}\|_F = \sqrt{N_R N_T}$, which is equivalent to that, on the average, each entry h_{mn} has a unit variance.
- Perfect channel state information (CSI) is available at the receiver but not at the transmitter. Therefore the total transmit power is equally divided on the transmit antennas.

Under the aforementioned assumptions, the MIMO channel capacity is given by [FG98]

$$C = \log_2\left(\det(\mathbf{I} + \frac{\mathrm{SNR}}{N_T}\mathbf{H}\mathbf{H}^H) \right), \tag{1.2}$$

where $\mathbf{I}$ is the identity matrix of size $N_R \times N_R$ and SNR is the average signal to noise ratio at the receive elements (also called the SISO-SNR [JW04]).

The capacity encompasses both effects of the SNR and the propagation environment (including the radiating elements characteristics). The channel capacity is the upper bound of error-free transmission rate between the transmit/receive ends, when optimum coding and modulation are employed. Using singular value decomposition, (1.2) can be expressed as [PGN03]

$$C = \sum_{i=1}^{K} \log_2(1 + \frac{\mathrm{SNR}}{N_T}\sigma_i^2), \tag{1.3}$$

where $\{\sigma_i\}$ are the singular values of $\mathbf{H}$ and $K = \min\{N_R, N_T\}$. Equation (1.3) shows that there are at most K parallel sub-channels. The contribution of each individual sub-channel to the MIMO capacity is evaluated by the square of its singular value σ_i^2.

1.1.1 Statistical and Deterministic Channel Modeling

In order to evaluate the MIMO channel capacity for a specific scenario, we need to know, either statistically or deterministically, the channel matrix $\mathbf{H}$. In the statistical approach, $\mathbf{H}$ is constructed with random entries having a distribution and a correlation which model the simulated scenario such as: outdoor, urban, rural, rich scattering, strong Line-of-Sight (LOS), etc. The statistical properties of the scenario are determined from measurements or simulations [e.g. SV87, ZFDW00, WJ02, ZFW02]. The ergodic (average) capacity is then found using Monte-Carlo simulations. In fact, a "universal" statistical channel model for MIMO systems does not exist. Furthermore, the statistical approach does not explicitly consider the dependence of the capacity on the specific propagation environment (layout geometry and material properties) nor does it allow to

accurately include the electromagnetic (EM) effects (antenna pattern/polarization or the array geometry/position/orientation), which are collectively called the Maxwellian framework [SSWB03, SBY+06].

In the deterministic approach, based on the simulation of the EM wave propagation, $\mathbf{H}$ is predicted for specific scenarios. The cost is obviously the heavy computational burden. There are several ways to model the EM propagation: either by numerical analysis methods (e.g. Finite-Difference Time-Domain FDTD) or by using the high frequency approximation (e.g. ray tracing). Using FDTD provides an accurate solution at all points of the solution space at the expense of the dramatic increase of the computation cost even if the layout is very simple. Consequently, FDTD is used for small structures or in conjunction with another computationally efficient method [WSC00]. Practically, when FDTD is used for propagation simulation, the environment is usually modeled as 2D to reduce the computational complexity [e.g. WSC00, YIZ04]. Such and other over-simplifications of the EM simulation parameters have been reported to underestimate, in general, the predicted capacity value since it does not accurately include the full multipath richness of the environment [SGWJ01, ESC04a, JW04].

In this work, we perform deterministic simulations in rectangular empty structures. By deterministic simulations, we mean to construct $\mathbf{H}$ according to the predicted EM fields such that:

- Maxwell's equations are obeyed.
- The scenario setup (array geometry and boundary conditions) is defined.
- The vectorial nature of the EM field (polarization) is taken into consideration.

In case of perfect electric conductor (PEC) walls, we use modal analysis as described in appendix B to construct $\mathbf{H}$. For other practical lossy-walls environments, we use the Image Ray Tracing (IRT), which belongs to the high frequency approximation solutions [MH91, TVD98, TVDD99, TVDL99,

AN00]. The IRT is applicable when the site dimensions are much larger than the wavelength. We briefly discuss the IRT in chapter 3; more details can be found in [Eln03].

The most general matrix representation for the wide-band (frequency-selective) channel is four-dimensional [XCV04], with dimensions $N_R \times N_T \times N_L \times N_N$, where N_L is the number of resolvable multipath rays and N_N represents the discrete-time samples of the channel. This general form is intended to model a time-dependent (the N_N-dimension) frequency selective channel (through multipath delays over the N_L-dimension). As previously stated, we assume that the indoor environment is narrowband, frequency-flat and quasi-static. Therefore, $\mathbf{H}$ is constant along the N_N-dimension and we coherently sum over the N_L-dimension (the multipath rays) as described in chapter 3. For a more comprehensive review of the MIMO wireless communications (propagation aspects), the reader can refer to [JW04].

1.1.2 Dimensionality Perspective

Low correlation between the elements of $\mathbf{H}$ is necessary in order to allow independent data streams to be transmitted simultaneously and hence increase the capacity. Nonetheless, low correlation is not sufficient for capacity increase [CFGV02, PGN03, JW04], since a low-correlation rank-deficient $\mathbf{H}$ yields low capacity as in the case of the keyhole channels [LCV01, CFGV02, ATM06].

From (1.3), the capacity value is determined by the SNR and the normalized singular values *distribution*. An even distribution of the singular values makes the MIMO system equivalent to K parallel SISO channels (also called having K dimensions). When we have $k \leq K$ equal non-zero singular values satisfying the Frobenius normalization

$$\|\mathbf{H}\|_F^2 = \sum_{i=1}^{K} \sigma_i^{\,2} = N_R N_T \,, \tag{1.4}$$

the capacity from (1.3) is expressed as

$$C_k = k \cdot \log_2(1 + \frac{N_R}{k}\mathrm{SNR}) \qquad k = 1, 2, ...K \,. \tag{1.5}$$

Equation (1.5) shows that the capacity increases almost linearly with the dimensionality k because the multiplication by k outside the logarithm has a stronger effect than the division by k inside the logarithm [JW04]. Table 1.1 shows the capacity of a (4,4) MIMO system for different values of SNR and dimensionality (k) according to (1.5). Obviously, by creating one additional dimension, we can get the same capacity while achieving a huge power gain. This is particularly true for low-dimensionality values (rank-deficient cases).

Table 1.1

(4,4) MIMO Capacity [bps/Hz]

SNR and Dimensionality Effects

	Dimensionality (k)			
SNR [dB]	**1**	**2**	**3**	**4**
7	4.40	6.93	**8.82**	10.35
10	5.36	**8.78**	11.52	13.84
14	6.66	11.36	**15.32**	18.83
17	7.65	13.32	18.25	**22.70**
20	**8.65**	**15.30**	21.21	26.63
21	8.98	15.96	**22.20**	**27.95**
27	10.97	19.94	**28.16**	35.89
30	11.97	**21.93**	31.15	39.87
31	12.30	22.60	32.14	**41.20**
40	**15.29**	**28.58**	**41.11**	53.15
60	**21.93**	**41.86**	61.04	79.73

The SNR is a common parameter in all communication systems, whereas the dimensionality is a unique feature of MIMO systems, which depends solely on the singular values *distribution*. The dimensionality is also known as the degrees of freedom (DOF) of MIMO systems and is the number of the parallel

sub-channels which are simultaneously available to convey information. When Shannon derived his celebrated formula of channel capacity in the presence of noise [Sha49], he was building on the previous work of Hartley [Har28]. Namely, Hartley's law states that " *the upper limit of the amount of information, which may be transmitted by means of magnitude-time functions, is set by the sum for the various available lines of the product of the line-frequency-range of each by the time during which it is available for use*" [Har28 page 557, Sha49 page 16]. This law should be regarded as a starting point rather than a final formula to compute the capacity for 2 reasons:

- It yields the dimensionality of the lines of essentially time-band-limited functions (i.e. the Shannon number $2WT$, based on optimum sampling using finite samples, which was rigorously proven afterward [LP62]).
- It presumes that coding is only based on the signal amplitude quantization [Sha49].

The point to be made is that dimensionality is a precursor of the channel capacity. One cannot estimate the channel capacity before evaluating first its dimensionality (DOF). When the target is to estimate the dimensionality, it should not be evaluated through the capacity. Since antenna elements are EM field samplers, the MIMO-DOF problem should be investigated based on a dimensionality framework (of essentially space-wavenumber-limited functions) rather than capacity comparison. The space-wavenumber product was also predicted by Hartley [Har28 page 560].

The core of this thesis is to investigate the MIMO-DOF according to the electromagnetic propagation characteristics of the environment. In other words, we are trying to establish a link between electromagnetism and information theory, which is a recent topic attracting many researchers. The problem can be stated as follows: Given a specific environment and a fixed array size at the transmit/receive ends, what is the maximum dimensionality that we can achieve by using a multi-antenna system? What is the optimum number of antennas needed to obtain this maximum dimensionality? Certainly, the MIMO-DOF is a

problem of utmost theoretical and practical importance because it explores the fundamental limit for the antenna packing within a given aperture according to the environment characteristics. The MIMO-DOF problem is investigated in this thesis by using deterministic vectorial sampling through polarized EM perfect samplers (polarized point sources/detectors). The following assumptions are made regarding the ideal EM sampler:

- It is not isotropic (its pattern has a null at the endfire direction).
- It makes no field disturbance (perfect detector).
- There is no mutual coupling between the EM samplers within the array.

The EM-DOF problem has been investigated from various perpectives: regarding the EM field sampling [BF87, BF89, BGS98], optical systems [Mil00, PM00], and recently, MIMO systems [PBT05, Loy05, LM06, Mig06, XJ06]. Bucci et al. [BF87, BF89, BGS98] investigated the non-redundant number of samples to represent the electromagnetic fields over arbitrary surfaces. Migliore [Mig06] followed this approach in the MIMO-DOF investigation which is more suitable for outdoor environments.

Miller and Piestun [Mil00, PM00] showed that singular value decomposition (SVD) is equivalent to finding the orthogonal communication modes (EM-DOF) of an optical system. Xu and Janaswamy [XJ06] followed this approach for MIMO-DOF investigation in 2D environments.

Poon et al. [PBT05] considered the problem in a way similar to the optics space-bandwidth product [Goo96] and used the clustered angular domain model with the free space Green's function.

Loyka [Loy05] studied the problem in an enclosure (waveguide or cavity) from a mode orthogonality perspective, assuming that the field is sampled across the whole cross section of the guide. More recently, Loyka and Mosig [LM06] tackled this problem based on the bandlimitedness of the spatial

spectrum of the EM fields. This is the same path we are following in this dissertation (chapter 5).

1.2 Motivation and Objectives

At an early phase of this research, our interest was focused on the site-specific EM-adaptive techniques to improve the MIMO capacity [ESC04b, ESC05, ESC06a]. Such techniques included adaptive phased-arrays (Fig. 1.1) and/or adaptive polarization selection (Fig. 1.2). The optimization parameter was the capacity at a given SNR.

Two main observations have been made from the results of the adaptive MIMO system in a deterministic scenario (lossy-wall corridor):

1. The capacity was sensitive to the array orientation (broadside orientation yields better capacity), which was confirmed earlier by measurements in similar scenarios [ATKM03, LDBD03].
2. For each array orientations (broadside or endfire), there was a capacity limit that was not exceeded even after combining the 2 adaptive techniques [ESC05].

These observations along with the recent interest in the MIMO-DOF problem in the literature motivated this current research.

Our objective in this work is threefold:

- Finding a well-defined metric dedicated to measure the MIMO systems dimensionality according to the singular values distribution (i.e. isolate the power consideration from the dimensionality).
- Making a careful study of the multi-polarization dimensionality under the Maxwellian framework.
- Investigating the MIMO-DOF for a fixed array size including all the available diversity (spatial, pattern and polarization) through a vectorial-EM sampling approach.

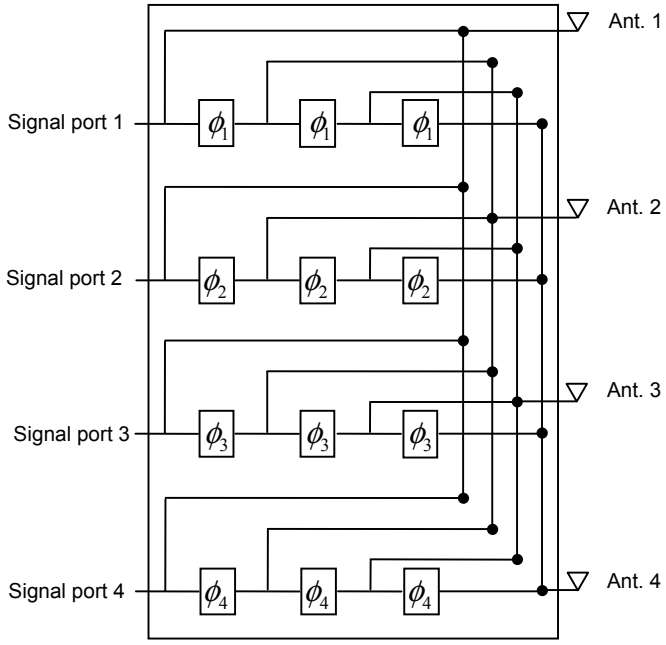

Fig. 1.1 Adaptive uniform phased-array (4,4) MIMO system [ESC04b].

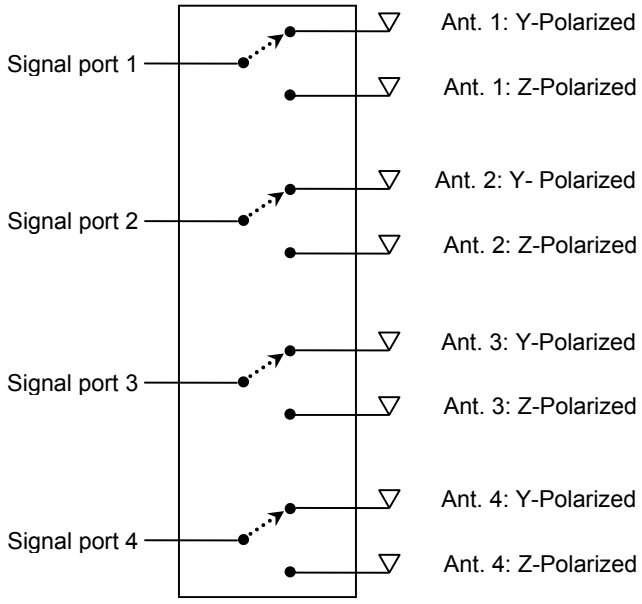

Fig. 1.2 Adaptive polarization selection (4,4) MIMO system [ESC06a].

1.3 Thesis Organization

The thesis is logically organized in 6 chapters. In chapter 2, we introduce a new metric: the Power-Independent Dimensionality (PID). The PID quantifies the effective parallel sub-channels available in a multi-antenna system. We present the properties and merits of the PID metric. We also make a comparison of the PID to similar power-dependent metrics in the literature, namely, the Effective Degrees of Freedom (EDOF) [SFGK00] and the Effective Dimensionality (ED) [LK03].

The electromagnetic modeling of deterministic indoor environments for MIMO systems is discussed in chapter 3. Working in the angular domain, we apply the high frequency approximation (ray modeling) and plane wave-front approximation in order to obtain an intuitive multi-keyhole matrix form [LL06a, LL06b]. Afterward, we include the full available diversity (multi-polarization and space-diversity) in the model. We provide some PID results of multi-polarization MIMO systems in lossy-walls rectangular environments, simulated using the image ray tracing (IRT) algorithm. We also show PID results, obtained through rigorous modal analysis, in a similar PEC wave-guide.

Chapter 4 is devoted to measure the available dimensionality, which can be captured through a collocated multi-polarization MIMO system. We rely on the deterministic model of chapter 3, which obeys Maxwell's equations. We investigate and quantify the capability of the electric and magnetic fields to carry independent information between 2 radiating structures in several scenarios: free space (near and far field), PEC and lossy-walls rectangular structures.

In chapter 5, we explore the maximum parallel sub-channels performance (DOF) of MIMO systems. For an array of a fixed size in a site-specific environment, we investigate the maximum achievable PID through the

combination of both the spatial and the pattern/polarization diversity. We show the effect of the environment properties and array orientation on the DOF in the context of the k-domain region of existence (ROE). Next, we extend the 1D optimum sampling results to the 2D and 3D array cases. We also present numerical results for the PID of multi-polarized MIMO system of a given array size (1D, 2D and 3D) in a PEC and lossy-walls corridor.

Chapter 6 concludes the thesis by listing the main contributions and proposing directions for future work. Because of the multi-disciplinary nature of this research, the required background information is briefly stated alongside the corresponding discussion when necessary. The appendices are allotted to background information, which are frequently needed throughout different parts of the dissertation. A list of the symbols, notation and acronyms is located at the end of the thesis.

Chapter 2
Power-Independent Dimensionality Metric

In this chapter, we introduce a new Power-Independent Dimensionality (PID) metric quantifying the effective parallel sub-channels available in a multi-antenna system. The main motivation hereof is to provide a handy measure which will be used in the subsequent chapters to evaluate the degrees of freedom (DOF) of MIMO systems in deterministic environments. The MIMO-DOF problem addresses the question of the optimum number of antenna elements needed to fully exploit a given environment diversity richness (spatial, pattern and/or polarization) according to the available spatial sub-channels. The answer to this question requires the knowledge of the spatial properties of the environment (expressed through the singular values *distribution* of the channel matrix) rather than the power level (SNR). The parallel sub-channels performance is also known as the channel dimensionality [LK03] or degrees of freedom (DOF) [SFGK00, PBT05, Mig06].

There are 2 approaches in the literature to compare the dimensionality performance of specific MIMO scenarios given the singular values sets. The first, which is power-dependent, is by using SNR-dependent dimensionality metrics [SFGK00, LK03] or by normalizing the channel matrix and then comparing the MIMO capacity at some "artificial" SNR values. The second approach, which is power-independent, is to use an *integer* number, determined by the channel matrix rank [e.g. RC98, PBT05] or its *effective* rank [Mig06, Str88], which depends on the number of *significant* non-zero singular values. The first approach suffers from the inability to separate the power from the dimensionality effect, whereas the second suffers from some subjectivity such as how to define *significant* and how to characterize the singular values *distribution* by a single metric. Moreover, both approaches are inadequate when it comes to comparing the dimensionality performance of 2 MIMO systems having a different number of transmit/receive elements.

The novel PID metric is based on the equivalence between the trace and Frobenius norms of the actual channel matrix and a fictitious one modeling an equi-useable sub-channels MIMO system. MIMO-DOF comparison using the PID metric is particularly meaningful in essentially *power-similar* situations such as packing/selecting antenna elements within an aperture size in a given environment or when we study the dimensionality of a moving MIMO system while normalizing the large scale fading. In the case of dimensionality-adaptive MIMO systems (e.g. adaptive beamforming or polarization [ESC05, ESC06a]), the PID provides a handy single parameter for optimization that can be fed back to the transmitter rather than the full channel entries or its singular values.

We emphasize that the proposed PID metric is not by any means a substitute of the capacity as a measure of the MIMO performance. For instance, the PID is not useful for the power-adaptive MIMO systems (based on water-filling), where the full set of singular values needs to be known for transmit power allocation. The PID is rather a complementary metric dedicated to measure the

unique feature of a MIMO communication system: the *number* of the available parallel data pipes in a given environment. Capacity is a global measure of MIMO performance comprising both the SNR effect (common to all communication systems) and the parallel sub-channels effect (unique to MIMO systems). Answering the DOF question in terms of the capacity or other power-dependent metrics can obscure some spatial phenomena of the environment due to the inseparability of the SNR effect. Capacity cannot experimentally be measured in the lab (being an upper limit performance measure) whereas, at least in theory, one can measure the number of *practically* available parallel data channels (dimensionality).

After introducing the PID definition, we present its properties and merits. We also make a comparison of the PID to similar power-dependent metrics in the literature, namely, the Effective Degrees of Freedom (EDOF) [SFGK00] and the Effective Dimensionality (ED) [LK03]. Further applications of the developed PID metric regarding the MIMO systems dimensionality are discussed in the subsequent chapters.

2.1 Equivalence-Based Power-Independent Dimensionality Metric

A MIMO channel matrix $\mathbf{H} \in \mathbb{C}^{N_R \times N_T}$, where (N_R, N_T) are the number of receive and transmit elements, respectively, can have up to $K = \min\{N_R, N_T\}$ parallel sub-channels. Consider another fictitious channel $\mathbf{H}^{(\mathbf{eq})}$, which has k equally contributing (out of K available) eigen channels whereas the remaining $(K-k)$ sub-channels have zero contribution. Obviously, $\mathbf{H}^{(\mathbf{eq})}$ has k communication dimensions and its singular values are given by

$$\sigma_i^{(eq)} = \begin{cases} \sigma_0 & i = 1, 2, ..., k \\ 0 & i = k+1, ..., K \end{cases}. \tag{2.1}$$

The normalized matrix $\frac{1}{\sigma_0}\mathbf{H}^{(\mathbf{eq})}$ is known as rank k partial isometry [HJ94].

In order to estimate the PID, we impose the following 2 Schatten-norm-based equivalence conditions on the 2 matrices $\mathbf{H}$ and $\mathbf{H}^{(\mathbf{eq})}$: both are to have the same Schatten 1-norm (trace norm $\|\bullet\|_{tr}$) and the same Schatten 2-norm (Frobenius norm $\|\bullet\|_F$). Consequently,

$$\|\mathbf{H}\|_{tr} \equiv \left\|\mathbf{H}^{(\mathbf{eq})}\right\|_{tr} = k\,\sigma_0 \tag{2.2a}$$

$$\|\mathbf{H}\|_F^2 \equiv \left\|\mathbf{H}^{(\mathbf{eq})}\right\|_F^2 = k\,{\sigma_0}^2 . \tag{2.2b}$$

Solving for k in (2.2) in terms of $\|\mathbf{H}\|_{tr}$ and $\|\mathbf{H}\|_F$, we obtain the equivalence-based PID

$$k \triangleq \mathrm{PID} = \left(\frac{\|\mathbf{H}\|_{tr}}{\|\mathbf{H}\|_F}\right)^2 = \frac{\left(\sum_{i=1}^{K}\sigma_i\right)^2}{\sum_{i=1}^{K}{\sigma_i}^2}. \tag{2.3}$$

For non-integer values of the PID, we understand that the dimensionality performance is better than that of $\lfloor \mathrm{PID} \rfloor$ equi-contributing sub-channels, where $\lfloor x \rfloor$ is the largest integer $\le x$.

In general, we are free to choose the Schatten p- and q-norms for the equivalence condition, where $1 \le p,q < \infty$ and the generic Schatten-norm-based PID is

$$\mathrm{PID}_{pq} = \left[\left(\sum_{i=1}^{K}\sigma_i^{\,q}\right)^p \Big/ \left(\sum_{i=1}^{K}\sigma_i^{\,p}\right)^q\right]^{\frac{1}{p-q}}. \tag{2.4}$$

However, the choice of 1 and 2 for p and q in (2.3) has a mathematical and physical justification. For large p and q, the Schatten norm tends to the spectral norm (the largest singular value) [HJ87] and the PID will be more biased to the largest singular value yielding a value close to 1 except for multiplicity of the

largest singular value. Therefore, a choice of small p and q makes the PID more sensitive to the small singular values, which justifies the choice of the Schatten 1-norm (minimum allowed value of p or q). Moreover, the Frobenius norm is readily connected to the power performance of the channel matrix, which justifies the choice of the Schatten 2-norm.

2.2 Properties and Merits of the PID

In this section, we present some useful properties of the PID metric, many of which will be used in the subsequent chapters.

2.2.1 Unitary Invariance

The PID, as given by (2.3), is a universal metric of any matrix and depends solely on its singular values distribution (a unitarily invariant quantity [HJ87]).

2.2.2 Matrix-Scaling Invariance

The ratio definition of the PID as given by (2.3) makes it invariant to any matrix scaling. Therefore, PID($\alpha\mathbf{H}$)=PID($\mathbf{H}$) for any complex scalar α. A direct consequence of this property is that the PID is *not* a matrix norm because it violates one of the 5 axioms defining the matrix norms [HJ87]: $|||\alpha\mathbf{H}|||=|\alpha|\cdot|||\mathbf{H}|||$. Another consequence is that the MIMO channel matrix does not require any normalization prior to computing its PID.

2.2.3 Range of the PID Values

For any non-zero matrix, it is straightforward to show that the PID ranges from 1 to $\text{rank}(\mathbf{H})$. The lower limit indicates the worst rank-deficient case ($\text{rank}(\mathbf{H})=1$ i.e. only one non-zero singular value), whereas the upper limit is

achieved in the case of partial or full isometry (all the non-zero singular values are equal). One can interpret $\mathrm{PID}(\mathbf{H})/\mathrm{rank}(\mathbf{H})$ as the "fraction of the average energy" (ranging from $1/\mathrm{rank}(\mathbf{H})$ to 1) of the discrete signal represented by the plot of $\{\sigma_i\}$.

2.2.4 Matrix-Size Independence

The PID does not depend on the matrix-size. This property makes the PID very suitable for dimensionality comparison of 2 MIMO systems having different number of elements. The other SNR-dependent metrics, including the capacity, are based on a size-dependent Frobenius normalization applied on the channel matrix, which can lead to inaccurate dimensionality evaluation. Suppose $\mathbf{Q}_1$, $\mathbf{Q}_2$ and $\mathbf{Q}_3$ are full-rank matrices of very small Frobenius-norm compared to $\|\mathbf{H}_1\|_F$. Then, the 2 matrices $\mathbf{H}_1$ and $\mathbf{H}_2 = \begin{pmatrix} \mathbf{H}_1 & \mathbf{Q}_1 \\ \mathbf{Q}_2 & \mathbf{Q}_3 \end{pmatrix}$ have essentially the same dimensionality (PID) and Frobenius-norm. However, their ranks are different and there is a discrepancy in their capacity value because of the applied size-dependent Frobenius normalization. $\mathbf{H}_2$ can represent a situation where some elements suffer from severe polarization mismatch and are still counted active in a multi-polarization MIMO system. Other matrix-size-sensitive situations are encountered when we are investigating the MIMO-DOF in essentially power-similar scenarios such as packing elements within a given array size or using an adaptive element-selection technique. A numerical comparison with other metrics regarding the matrix-size effect on the dimensionality is included in the next section.

2.2.5 Relation to the Kronecker Product

The relation between the Schatten p-norm $N_p(\bullet)$ and the Kronecker product of 2 matrices $\mathbf{A} \otimes \mathbf{B}$ is such that [HJ94]

$$N_p(\mathbf{A}\otimes\mathbf{B}) = N_p(\mathbf{A})N_p(\mathbf{B}). \tag{2.5}$$

Therefore, based on (2.3), we have a similar PID relation

$$\mathrm{PID}(\mathbf{A}\otimes\mathbf{B}) = \mathrm{PID}(\mathbf{A})\mathrm{PID}(\mathbf{B}), \tag{2.6}$$

which is useful in modeling the effect of combining multi-polarization with spatial diversity on the MIMO-DOF.

2.2.6 Matrix Product Inequality

Since the PID objective is to count the number of "significant" singular values in a well-defined manner, it can be viewed as an effective rank of the matrix. It is then naturally to check whether the following rank inequality of the matrix product [HJ87]

$$\mathrm{rank}(\mathbf{AB}) \le \min\{\mathrm{rank}(\mathbf{A}), \mathrm{rank}(\mathbf{B})\} \tag{2.7}$$

is true as well for the PID. Should the PID be a unitarily invariant matrix *norm*, (2.7) would have been straightforwardly true for the PID [HJ87]. Indeed, the PID is a unitarily invariant quantity (property 2.2.1), nevertheless, it is not a matrix norm (property 2.2.2). Therefore, we can not assert that (2.7) is strictly true for the PID. However, based on some Monte-Carlo simulations reported hereafter, we can say that it is "essentially" true that

$$\mathrm{PID}(\mathbf{AB}) \le \min\{\mathrm{PID}(\mathbf{A}), \mathrm{PID}(\mathbf{B})\} \qquad \mathrm{PID}(\mathbf{A}), \mathrm{PID}(\mathbf{B}) \gg 1. \tag{2.8}$$

The result (2.8) is important in evaluating the MIMO dimensionality bottle-neck as will be discussed in the next chapters. This is the reason why we are providing some simulation results to shed light on its validity. In the first simulation, $\mathbf{A}$ and $\mathbf{B} \in \mathbb{C}^{N\times N}$ are square matrices. The entries of each are independent Gaussian distributed complex scalars of zero mean and unit variance. We denote $\min\{\mathrm{PID}(\mathbf{A}), \mathrm{PID}(\mathbf{B})\}$ and $\max\{\mathrm{PID}(\mathbf{A}), \mathrm{PID}(\mathbf{B})\}$ by $\mathrm{PID}_{\min}$ and $\mathrm{PID}_{\max}$, respectively. Based on 10^6 incidences, we evaluate the probability $P[\mathrm{PID}(\mathbf{AB}) > \mathrm{PID}_{\min}]$ and $P[\mathrm{PID}(\mathbf{AB}) \ge \mathrm{PID}_{\max}]$. We also report

the maximum error value of $(\mathrm{PID}(\mathbf{AB}) - \mathrm{PID}_{\min})$ over all incidences. The results are shown in Table 2.1.

From Table 2.1, we can see that the maximum error does not surpass 1. Also as N increases, the probability that (2.8) is false decreases and so does the maximum error. We repeated the simulations for rectangular $\mathbf{A} \in \mathbb{C}^{N\times 20}$ and square $\mathbf{B} \in \mathbb{C}^{20\times 20}$. The results are shown in Table 2.2, where we can notice that the maximum error is generally smaller than in Table 2.1.

Table 2.1

Monte-Carlo PID Inequality Results of Matrix Product.

$\mathbf{A}$ and $\mathbf{B} \in \mathbb{C}^{N\times N}$

N	$P[\mathrm{PID}(\mathbf{AB}) > \mathrm{PID}_{\min}]$	$P[\mathrm{PID}(\mathbf{AB}) \geq \mathrm{PID}_{\max}]$	Maximum Error
2	2.75×10^{-1}	6.59×10^{-2}	0.8433
3	1.07×10^{-1}	1.15×10^{-2}	0.9707
4	3.11×10^{-2}	1.70×10^{-3}	0.9549
5	6.70×10^{-3}	1.92×10^{-4}	0.7254
6	1.10×10^{-3}	1.20×10^{-5}	0.4349
7	1.33×10^{-4}	$<1.00\times10^{-6}$	0.3235
8	1.30×10^{-5}	$<1.00\times10^{-6}$	0.2322
9	2.00×10^{-6}	$<1.00\times10^{-6}$	0.0247

Table 2.2

Monte-Carlo PID Inequality Results of Matrix Product.

$\mathbf{A} \in \mathbb{C}^{N\times 20}$ and $\mathbf{B} \in \mathbb{C}^{20\times 20}$

N	$P[\mathrm{PID}(\mathbf{AB}) > \mathrm{PID}_{\min}]$	$P[\mathrm{PID}(\mathbf{AB}) \geq \mathrm{PID}_{\max}]$	Maximum Error
2	2.21×10^{-1}	$<1.00\times10^{-6}$	0.1662
3	9.15×10^{-2}	$<1.00\times10^{-6}$	0.2128
4	3.10×10^{-2}	$<1.00\times10^{-6}$	0.2478
5	8.40×10^{-3}	$<1.00\times10^{-6}$	0.2385
6	1.80×10^{-3}	$<1.00\times10^{-6}$	0.2638
7	2.75×10^{-4}	$<1.00\times10^{-6}$	0.1653
8	2.20×10^{-5}	$<1.00\times10^{-6}$	0.1112
9	5.00×10^{-6}	$<1.00\times10^{-6}$	0.1001

We perform one more Monte-Carlo simulation regarding the PID matrix product inequality when $\mathrm{PID}(\mathbf{A})$ is varying over a wide range. We assume that both $\mathbf{A}$ and $\mathbf{B} \in \mathbb{C}^{100\times100}$ and the entries of $\mathbf{B}$ are complex Gaussian as before. Moreover, we assume that $\mathbf{A}$ is a deterministic diagonal matrix such that $\mathbf{A} = \mathrm{diag}(\sigma_1, 1, 1, ..., 1)$, where $\sigma_1 \in \{1, 2, ..., 100\}$. Accordingly, $\mathrm{PID}(\mathbf{A})$ takes values from 100 down to close to 1. For each value of σ_1, we evaluate the average of $\mathrm{PID}(\mathbf{B})$ and $\mathrm{PID}(\mathbf{AB})$ over 1000 incidences. The results are plotted in Fig. 2.1.

We can make 2 observations from Fig. 2.1. First, (2.8) is valid, on the average, over the entire range of $\mathrm{PID}(\mathbf{A})$. Second, the discrepancy between $\mathrm{PID}(\mathbf{AB})$ and $\mathrm{PID}_{\min}$ increases as $\mathrm{PID}(\mathbf{A})$ gets closer to $\mathrm{PID}(\mathbf{B})$. Therefore, the upper bound of (2.8) is tighter when there is a wide difference between the dimensionality of the 2 matrices.

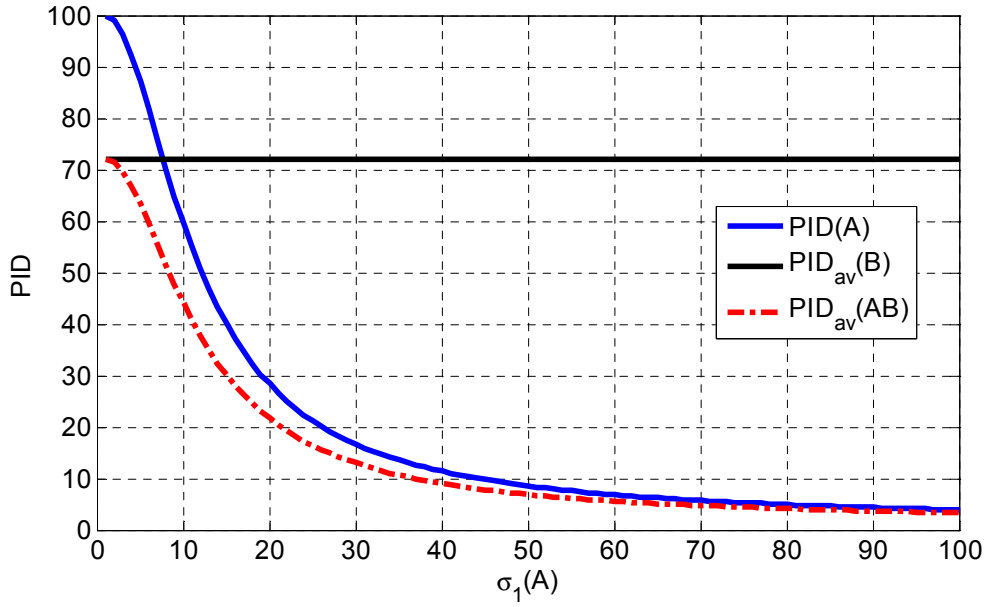

Fig. 2.1 Average PID inequality results of the matrix product. PID(A) is varying over a wide range.

2.2.7 Comparison with the PSWF Eigen Values (Shannon Number)

We present the following matrix normalization, which is independent of the matrix size (N_R, N_T)

$$\overline{\mathbf{H}} = \frac{\mathbf{H}}{\|\mathbf{H}\|_F / \sqrt{\mathrm{PID}}} = \frac{\mathbf{H}}{\|\mathbf{H}\|_F^2 / \|\mathbf{H}\|_{tr}}, \tag{2.9}$$

or, in terms of the normalized singular values $\{\overline{\sigma}_i\}$,

$$\overline{\sigma}_i = \sigma_i \frac{\sum_{i=1}^{K} \sigma_i}{\sum_{i=1}^{K} \sigma_i^2}, \tag{2.10}$$

which leads to

$$\text{PID}=\sum_{i=1}^{K}\bar{\sigma}_i=\sum_{i=1}^{K}\bar{\sigma}_i^{\,2}=\left\|\bar{\mathbf{H}}\right\|_{tr}=\left\|\bar{\mathbf{H}}\right\|_F^2 \quad . \tag{2.11}$$

Interestingly, (2.11) is consistent with a similar property of the optimum basis functions $\psi_i(c,t)$, where $c=\pi WT$, used to determine the DOF of "essentially" time-limited ($|t|\le T/2$) bandlimited ($|f|\le W$) *continuous* functions $y(t)$. In appendix A, we report from the literature some properties of ψ_i and its fractional energy $\lambda_i(c)$ within $|t|\le T/2$, where $(1>\lambda_0>\lambda_1>\ldots\ge 0)$. In the MIMO-DOF problem, the finite aperture size in the space-domain is analogous to the finite time-window T of $y(t)$. Similarly, the bandlimited spatial spectrum of the electromagnetic far-field is analogous to the bandlimited temporal spectrum of $y(t)$ [LM06]. Hence, λ_i and $\bar{\sigma}_i^{\,2}$ represent the energy/power contribution of the orthogonal i^{th} basis/channel, respectively. In appendix A, we report the following identity (A.20) regarding the Shannon number $2WT$ [GG73]

$$\sum_{i=0}^{\infty}\lambda_i(c)=2WT=\text{DOF} \qquad \text{every } c\ . \tag{2.12}$$

Moreover, we conjecture in (A.22) the following asymptotic relation

$$\sum_{i=0}^{\infty}\sqrt{\lambda_i(c)}\xrightarrow[c\to\infty]{}2WT=\text{DOF}\,. \tag{2.13}$$

Clearly, (2.12-13) are consistent with (2.11) such that, under the normalization (2.9), both the *finite* set $\{\bar{\sigma}_i^{\,2}\}$ and the *infinite* set $\{\lambda_i\}$ summation yields exactly the DOF (Shannon number) of the respective *discrete* and *continuous* problems. The same is true with $\{\bar{\sigma}_i\}$ and could asymptotically be viewed as true (for large $2WT$) with $\left\{\sqrt{\lambda_i}\right\}$. However, unlike the values of $\{\lambda_i\}$, it should be noted that some $\bar{\sigma}_i$ are ≥ 1. Under the normalization (2.9), it can be shown that the largest singular value $\bar{\sigma}_1\ge 1$, where the equality holds if and only if all the non-zero singular values are equal (i.e. in the case of partial isometry).

2.3 Comparison with Other Power-Dependent Metrics

In this section, we make a comparison between the PID and 2 SNR-dependent dimensionality metrics in the literature, namely, the Effective Degrees of Freedom (EDOF) [SFGK00] and the Effective Dimensionality (ED) [LK03]. We assume a MIMO system with equal transmit power allocation (no Channel State Information at the transmit side). Therefore, under the normalization

$$\overline{\mathbf{H}} = \frac{\mathbf{H}}{\|\mathbf{H}\|_F / \sqrt{N_R N_T}}, \tag{2.14}$$

the capacity is given by [FG98]

$$C = \sum_{i=1}^{K} \log_2(1 + \frac{\mathrm{SNR}}{N_T}\sigma_i^{\,2}). \tag{2.15}$$

The EDOF is defined as [SFGK00]

$$\mathrm{EDOF} \equiv \frac{d}{d\delta} C(2^{\delta} \cdot \mathrm{SNR})\Big|_{\delta=0}, \tag{2.16}$$

where $C(\bullet)$ is the MIMO channel capacity at the given SNR. The EDOF in (2.16) can be expressed in other forms such as [KRK05]

$$\mathrm{EDOF} = \frac{d\,C(\mathrm{SNR})}{d(\log_2 \mathrm{SNR})}, \tag{2.17}$$

or, after simplification using (2.15) [ESC06b],

$$\mathrm{EDOF}(\mathrm{SNR}, \sigma_i) = \sum_{i=1}^{K} \frac{1}{1 + \frac{N_T}{\sigma_i^{\,2}\,\mathrm{SNR}}}. \tag{2.18}$$

It is obvious from (2.18) that, regardless of the distribution of $\{\sigma_i\}$, the EDOF yields rank($\mathbf{H}$) and 0 for high and low SNR, respectively [SFGK00]. Therefore, a Power-Independent EDOF (PIEDOF), defined as

$\text{PIEDOF} \triangleq \lim_{\text{SNR}\to\infty} \frac{d\,C(\text{SNR})}{d(\log_2 \text{SNR})}$, is also *singular-values-independent* and always yields rank(**H**) [SSEV06]. Hence, unlike the proposed singular-values-based PID metric, the PIEDOF is not a suitable measure of the environment-specific MIMO-DOF performance since it ignores the singular values distribution. Also, the PIEDOF fails to give an acceptable estimate of the MIMO-DOF in the moderate SNR region (10-20 dB), which is more important from a system design perspective.

We move now to another power-dependent DOF metric in the literature. The effective dimensionality (ED) [LK03] is defined as the number of parallel equi-useable channels yielding the same capacity at a given SNR. Hence, under the normalization (2.14), it is found by solving the transcendental equation

$$\sum_{i=1}^{K} \log_2\left(1+\frac{\text{SNR}}{N_T}\sigma_i{}^2\right) = \text{ED}(\text{SNR},\sigma_i)\cdot\log_2\left(1+\text{SNR}\,\frac{N_R}{\text{ED}(\text{SNR},\sigma_i)}\right). \qquad (2.19)$$

We present some numerical comparisons of EDOF, ED and PID for 6 cases as described in Table 2.3. The singular value sets $\{\sigma_i\}$ are selected such that

1. they satisfy the normalization (2.14),
2. they are designed to have a fixed integer PID according to Table 2.3, and
3. their distribution is characterized by a "knee" at the B^{th} singular value i.e. for each set, there are B large and $K-B$ small singular values, where B can take any value from $\{1,2,...,\text{PID}\}$. The steepest drop between any 2 adjacent singular values occurs between σ_B and σ_{B+1}, typically of about 10 dB or more.

The classification of $\{\sigma_i\}$ into 2 sub-sets - "large" and "small" - is motivated by the singular values behavior of the MIMO spatial-DOF problems where they exhibit a step-like distribution [PBT05, Mig06] analogous to the eigen values $\{\lambda_i\}$ behavior in the temporal DOF problems [SP61, LP62, Sle83].

In appendix A, we report that for $i \ll 2WT$, most of $\lambda_i(c)$ are close to unity whereas for $i \gg 2WT$, most of $\lambda_i(c)$ are close to zero. The interval of transition from 1 to 0, around $i \sim 2WT$, grows as $\log(c)$ [LP62, Sle83]. The singular values in the MIMO-DOF problems are expected to follow the same pattern [PBT05, Mig06] and accordingly, the value of B is expected to be close to PID. Our intention by allowing B taking all the possible values $\{1, 2, ..., \text{PID}\}$ is to investigate how the PID will compare with the other metrics in pathological cases when the difference ($\text{PID} - B$) is large.

For the cases 1-3 in Table 2.3, we employ 2 distributions regarding both large and small sub-sets: a) flat distribution, and b) 1 dB linearly decreasing distribution. The PID and the matrix size are fixed for each case. We compare the ED and EDOF to the fixed PID for several values of B. Fig. 2.2-4 show the numerical results of the SNR-dependence of the EDOF and ED in the 3 cases. The numerical values of $\{\sigma_i\}$ are given in Table 2.4 and their distribution is sketched at the top left corner of Fig. 2.2-4.

Table 2.3

Matrix Size and Singular Values Distribution for Numerical Comparison

	Matrix Size	PID and B	Singular Values Distribution (dB)
1	$\mathbf{H}_1 : 50\times 50$	$\text{PID} = 10$ $B = \{1,2,...,10\}$	$\sigma_i(\mathbf{H}_1) = \begin{cases} \sigma_1 - a(i-1) & i = 1,2,...,B \\ \sigma_{B+1} - a(i-B-1) & i = B+1,...,K \end{cases}$ $a = 0$ or 1 for flat or 1 dB decreasing distribution, respectively.
2	$\mathbf{H}_1 : 10\times 10$	$\text{PID} = 5$ $B = \{1,2,3,4,5\}$	
3	$\mathbf{H}_1 : 4\times 4$	$\text{PID} = 3$ $B = \{1,2,3\}$	
4	$\mathbf{H}_1 : 50\times 50$ $\mathbf{H}_2 : 100\times 100$	$\text{PID} = 10$ $B = 10$	$\sigma_i(\mathbf{H}_2) = \begin{cases} \sigma_i(\mathbf{H}_1) & a = 1 \\ & i = 1,2,...,K \\ \sigma_{B+1} - (i-B-1) & i = K+1,...,2K \end{cases}$
5	$\mathbf{H}_1 : 10\times 10$ $\mathbf{H}_2 : 20\times 20$	$\text{PID} = 5$ $B = 5$	
6	$\mathbf{H}_1 : 4\times 4$ $\mathbf{H}_2 : 8\times 8$	$\text{PID} = 3$ $B = 3$	

Table 2.4

Numerical Values of the Singular Values Distribution of Table 2.3

Knee Drop (dB)	26.44	25.22	25.12	25.56	26.44	27.80	29.79	32.85	38.45	inf	10.23	9.06	8.83	9.03	9.53	10.33	11.48	13.13	15.59	19.75
PID=10	Flat SV (dB)										1 dB decreasing SV (dB)									
	B=1	B=2	B=3	B=4	B=5	B=6	B=7	B=8	B=9	B=10	B=1	B=2	B=3	B=4	B=5	B=6	B=7	B=8	B=9	B=10
SV1	33.52	30.67	29.00	27.82	26.90	26.15	25.50	24.94	24.43	23.98	32.33	30.41	29.47	28.89	28.49	28.20	27.98	27.81	27.67	27.56
SV2	7.08	30.67	29.00	27.82	26.90	26.15	25.50	24.94	24.43	23.98	22.10	29.41	28.47	27.89	27.49	27.20	26.98	26.81	26.67	26.56
SV3	7.08	5.44	29.00	27.82	26.90	26.15	25.50	24.94	24.43	23.98	21.10	20.36	27.47	26.89	26.49	26.20	25.98	25.81	25.67	25.56
SV4	7.08	5.44	3.89	27.82	26.90	26.15	25.50	24.94	24.43	23.98	20.10	19.36	18.64	25.89	25.49	25.20	24.98	24.81	24.67	24.56
SV5	7.08	5.44	3.89	2.26	26.90	26.15	25.50	24.94	24.43	23.98	19.10	18.36	17.64	16.86	24.49	24.20	23.98	23.81	23.67	23.56
SV6	7.08	5.44	3.89	2.26	0.46	26.15	25.50	24.94	24.43	23.98	18.10	17.36	16.64	15.86	14.96	23.20	22.98	22.81	22.67	22.56
SV7	7.08	5.44	3.89	2.26	0.46	-1.65	25.50	24.94	24.43	23.98	17.10	16.36	15.64	14.86	13.96	12.87	21.98	21.81	21.67	21.56
SV8	7.08	5.44	3.89	2.26	0.46	-1.65	-4.29	24.94	24.43	23.98	16.10	15.36	14.64	13.86	12.96	11.87	10.50	20.81	20.67	20.56
SV9	7.08	5.44	3.89	2.26	0.46	-1.65	-4.29	-7.92	24.43	23.98	15.10	14.36	13.64	12.86	11.96	10.87	9.50	7.68	19.67	19.56
SV10	7.08	5.44	3.89	2.26	0.46	-1.65	-4.29	-7.92	-14.02	23.98	14.10	13.36	12.64	11.86	10.96	9.87	8.50	6.68	4.08	18.56
SV11	7.08	5.44	3.89	2.26	0.46	-1.65	-4.29	-7.92	-14.02	-inf	13.10	12.36	11.64	10.86	9.96	8.87	7.50	5.68	3.08	-1.19
SV12	7.08	5.44	3.89	2.26	0.46	-1.65	-4.29	-7.92	-14.02	-inf	12.10	11.36	10.64	9.86	8.96	7.87	6.50	4.68	2.08	-2.19
SV13	7.08	5.44	3.89	2.26	0.46	-1.65	-4.29	-7.92	-14.02	-inf	11.10	10.36	9.64	8.86	7.96	6.87	5.50	3.68	1.08	-3.19
SV14	7.08	5.44	3.89	2.26	0.46	-1.65	-4.29	-7.92	-14.02	-inf	10.10	9.36	8.64	7.86	6.96	5.87	4.50	2.68	0.08	-4.19
SV15	7.08	5.44	3.89	2.26	0.46	-1.65	-4.29	-7.92	-14.02	-inf	9.10	8.36	7.64	6.86	5.96	4.87	3.50	1.68	-0.92	-5.19
SV16	7.08	5.44	3.89	2.26	0.46	-1.65	-4.29	-7.92	-14.02	-inf	8.10	7.36	6.64	5.86	4.96	3.87	2.50	0.68	-1.92	-6.19
SV17	7.08	5.44	3.89	2.26	0.46	-1.65	-4.29	-7.92	-14.02	-inf	7.10	6.36	5.64	4.86	3.96	2.87	1.50	-0.32	-2.92	-7.19
SV18	7.08	5.44	3.89	2.26	0.46	-1.65	-4.29	-7.92	-14.02	-inf	6.10	5.36	4.64	3.86	2.96	1.87	0.50	-1.32	-3.92	-8.19
SV19	7.08	5.44	3.89	2.26	0.46	-1.65	-4.29	-7.92	-14.02	-inf	5.10	4.36	3.64	2.86	1.96	0.87	-0.50	-2.32	-4.92	-9.19
SV20	7.08	5.44	3.89	2.26	0.46	-1.65	-4.29	-7.92	-14.02	-inf	4.10	3.36	2.64	1.86	0.96	-0.13	-1.50	-3.32	-5.92	-10.19
SV21	7.08	5.44	3.89	2.26	0.46	-1.65	-4.29	-7.92	-14.02	-inf	3.10	2.36	1.64	0.86	-0.04	-1.13	-2.50	-4.32	-6.92	-11.19
SV22	7.08	5.44	3.89	2.26	0.46	-1.65	-4.29	-7.92	-14.02	-inf	2.10	1.36	0.64	-0.14	-1.04	-2.13	-3.50	-5.32	-7.92	-12.19
SV23	7.08	5.44	3.89	2.26	0.46	-1.65	-4.29	-7.92	-14.02	-inf	1.10	0.36	-0.36	-1.14	-2.04	-3.13	-4.50	-6.32	-8.92	-13.19
SV24	7.08	5.44	3.89	2.26	0.46	-1.65	-4.29	-7.92	-14.02	-inf	0.10	-0.64	-1.36	-2.14	-3.04	-4.13	-5.50	-7.32	-9.92	-14.19
SV25	7.08	5.44	3.89	2.26	0.46	-1.65	-4.29	-7.92	-14.02	-inf	-0.90	-1.64	-2.36	-3.14	-4.04	-5.13	-6.50	-8.32	-10.92	-15.19
SV26	7.08	5.44	3.89	2.26	0.46	-1.65	-4.29	-7.92	-14.02	-inf	-1.90	-2.64	-3.36	-4.14	-5.04	-6.13	-7.50	-9.32	-11.92	-16.19
SV27	7.08	5.44	3.89	2.26	0.46	-1.65	-4.29	-7.92	-14.02	-inf	-2.90	-3.64	-4.36	-5.14	-6.04	-7.13	-8.50	-10.32	-12.92	-17.19
SV28	7.08	5.44	3.89	2.26	0.46	-1.65	-4.29	-7.92	-14.02	-inf	-3.90	-4.64	-5.36	-6.14	-7.04	-8.13	-9.50	-11.32	-13.92	-18.19
SV29	7.08	5.44	3.89	2.26	0.46	-1.65	-4.29	-7.92	-14.02	-inf	-4.90	-5.64	-6.36	-7.14	-8.04	-9.13	-10.50	-12.32	-14.92	-19.19
SV30	7.08	5.44	3.89	2.26	0.46	-1.65	-4.29	-7.92	-14.02	-inf	-5.90	-6.64	-7.36	-8.14	-9.04	-10.13	-11.50	-13.32	-15.92	-20.19
SV31	7.08	5.44	3.89	2.26	0.46	-1.65	-4.29	-7.92	-14.02	-inf	-6.90	-7.64	-8.36	-9.14	-10.04	-11.13	-12.50	-14.32	-16.92	-21.19
SV32	7.08	5.44	3.89	2.26	0.46	-1.65	-4.29	-7.92	-14.02	-inf	-7.90	-8.64	-9.36	-10.14	-11.04	-12.13	-13.50	-15.32	-17.92	-22.19
SV33	7.08	5.44	3.89	2.26	0.46	-1.65	-4.29	-7.92	-14.02	-inf	-8.90	-9.64	-10.36	-11.14	-12.04	-13.13	-14.50	-16.32	-18.92	-23.19
SV34	7.08	5.44	3.89	2.26	0.46	-1.65	-4.29	-7.92	-14.02	-inf	-9.90	-10.64	-11.36	-12.14	-13.04	-14.13	-15.50	-17.32	-19.92	-24.19
SV35	7.08	5.44	3.89	2.26	0.46	-1.65	-4.29	-7.92	-14.02	-inf	-10.90	-11.64	-12.36	-13.14	-14.04	-15.13	-16.50	-18.32	-20.92	-25.19
SV36	7.08	5.44	3.89	2.26	0.46	-1.65	-4.29	-7.92	-14.02	-inf	-11.90	-12.64	-13.36	-14.14	-15.04	-16.13	-17.50	-19.32	-21.92	-26.19
SV37	7.08	5.44	3.89	2.26	0.46	-1.65	-4.29	-7.92	-14.02	-inf	-12.90	-13.64	-14.36	-15.14	-16.04	-17.13	-18.50	-20.32	-22.92	-27.19
SV38	7.08	5.44	3.89	2.26	0.46	-1.65	-4.29	-7.92	-14.02	-inf	-13.90	-14.64	-15.36	-16.14	-17.04	-18.13	-19.50	-21.32	-23.92	-28.19
SV39	7.08	5.44	3.89	2.26	0.46	-1.65	-4.29	-7.92	-14.02	-inf	-14.90	-15.64	-16.36	-17.14	-18.04	-19.13	-20.50	-22.32	-24.92	-29.19
SV40	7.08	5.44	3.89	2.26	0.46	-1.65	-4.29	-7.92	-14.02	-inf	-15.90	-16.64	-17.36	-18.14	-19.04	-20.13	-21.50	-23.32	-25.92	-30.19
SV41	7.08	5.44	3.89	2.26	0.46	-1.65	-4.29	-7.92	-14.02	-inf	-16.90	-17.64	-18.36	-19.14	-20.04	-21.13	-22.50	-24.32	-26.92	-31.19
SV42	7.08	5.44	3.89	2.26	0.46	-1.65	-4.29	-7.92	-14.02	-inf	-17.90	-18.64	-19.36	-20.14	-21.04	-22.13	-23.50	-25.32	-27.92	-32.19
SV43	7.08	5.44	3.89	2.26	0.46	-1.65	-4.29	-7.92	-14.02	-inf	-18.90	-19.64	-20.36	-21.14	-22.04	-23.13	-24.50	-26.32	-28.92	-33.19
SV44	7.08	5.44	3.89	2.26	0.46	-1.65	-4.29	-7.92	-14.02	-inf	-19.90	-20.64	-21.36	-22.14	-23.04	-24.13	-25.50	-27.32	-29.92	-34.19
SV45	7.08	5.44	3.89	2.26	0.46	-1.65	-4.29	-7.92	-14.02	-inf	-20.90	-21.64	-22.36	-23.14	-24.04	-25.13	-26.50	-28.32	-30.92	-35.19
SV46	7.08	5.44	3.89	2.26	0.46	-1.65	-4.29	-7.92	-14.02	-inf	-21.90	-22.64	-23.36	-24.14	-25.04	-26.13	-27.50	-29.32	-31.92	-36.19
SV47	7.08	5.44	3.89	2.26	0.46	-1.65	-4.29	-7.92	-14.02	-inf	-22.90	-23.64	-24.36	-25.14	-26.04	-27.13	-28.50	-30.32	-32.92	-37.19
SV48	7.08	5.44	3.89	2.26	0.46	-1.65	-4.29	-7.92	-14.02	-inf	-23.90	-24.64	-25.36	-26.14	-27.04	-28.13	-29.50	-31.32	-33.92	-38.19
SV49	7.08	5.44	3.89	2.26	0.46	-1.65	-4.29	-7.92	-14.02	-inf	-24.90	-25.64	-26.36	-27.14	-28.04	-29.13	-30.50	-32.32	-34.92	-39.19
SV50	7.08	5.44	3.89	2.26	0.46	-1.65	-4.29	-7.92	-14.02	-inf	-25.90	-26.64	-27.36	-28.14	-29.04	-30.13	-31.50	-33.32	-35.92	-40.19

Knee Drop (dB)	15.56	15.56	17.29	21.67	inf	11.75	11.70	13.25	17.07	33.61
PID=5	Flat SV					1 dB decreasing SV				
	B=1	B=2	B=3	B=4	B=5	B=1	B=2	B=3	B=4	B=5
SV1	19.03	16.53	15.04	13.94	13.01	18.91	16.96	15.95	15.28	14.78
SV2	3.47	16.53	15.04	13.94	13.01	7.16	15.96	14.95	14.28	13.78
SV3	3.47	0.97	15.04	13.94	13.01	6.16	4.26	13.95	13.28	12.78
SV4	3.47	0.97	-2.25	13.94	13.01	5.16	3.26	0.70	12.28	11.78
SV5	3.47	0.97	-2.25	-7.74	13.01	4.16	2.26	-0.30	-4.79	10.78
SV6	3.47	0.97	-2.25	-7.74	-inf	3.16	1.26	-1.30	-5.79	-22.83
SV7	3.47	0.97	-2.25	-7.74	-inf	2.16	0.26	-2.30	-6.79	-23.83
SV8	3.47	0.97	-2.25	-7.74	-inf	1.16	-0.74	-3.30	-7.79	-24.83
SV9	3.47	0.97	-2.25	-7.74	-inf	0.16	-1.74	-4.30	-8.79	-25.83
SV10	3.47	0.97	-2.25	-7.74	-inf	-0.84	-2.74	-5.30	-9.79	-26.83

Knee Drop (dB)	9.54	11.44	inf	8.54	10.34	36.50
PID=3	Flat SV			1 dB dec.		
	B=1	B=2	B=3	B=1	B=2	B=3
SV1	10.79	8.73	7.27	10.77	9.19	8.19
SV2	1.25	8.73	7.27	2.23	8.19	7.19
SV3	1.25	-2.71	7.27	1.23	-2.15	6.19
SV4	1.25	-2.71	-inf	0.23	-3.15	-30.31

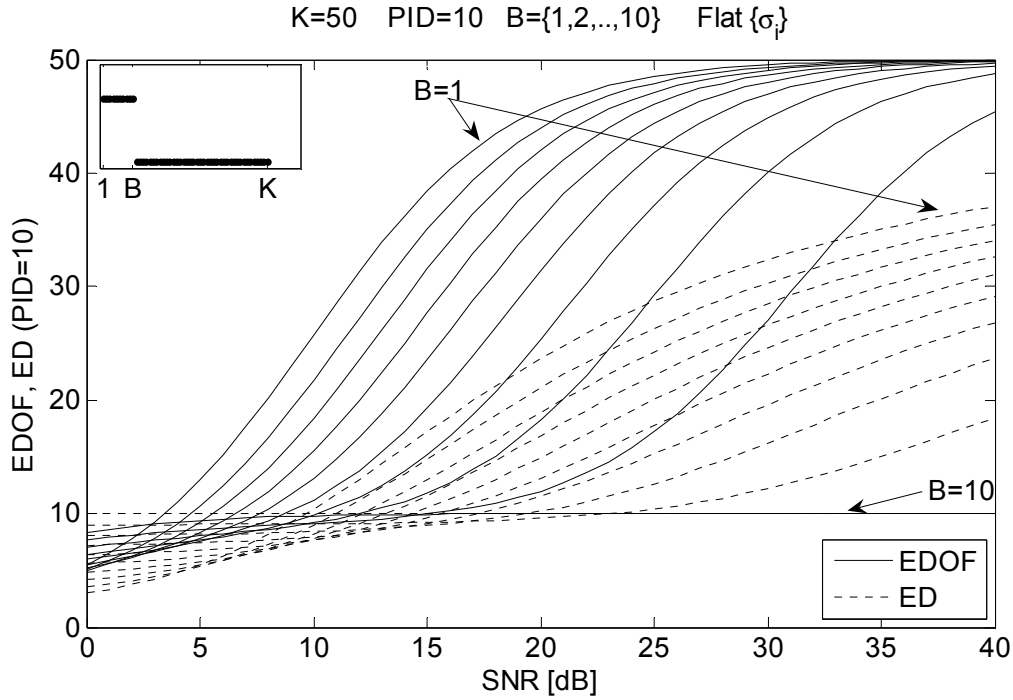

(a)

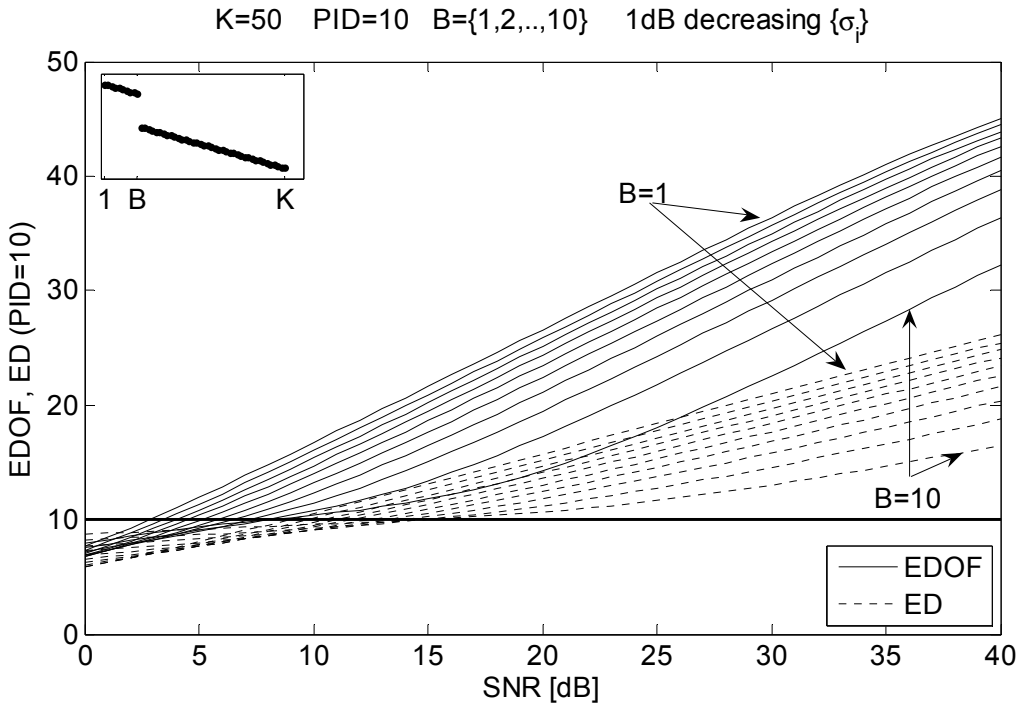

(b)

Fig. 2.2

EDOF, ED and PID comparison for case 1: (50,50) MIMO system and PID=10 Singular values distribution: (a) flat and (b) 1 dB decreasing.

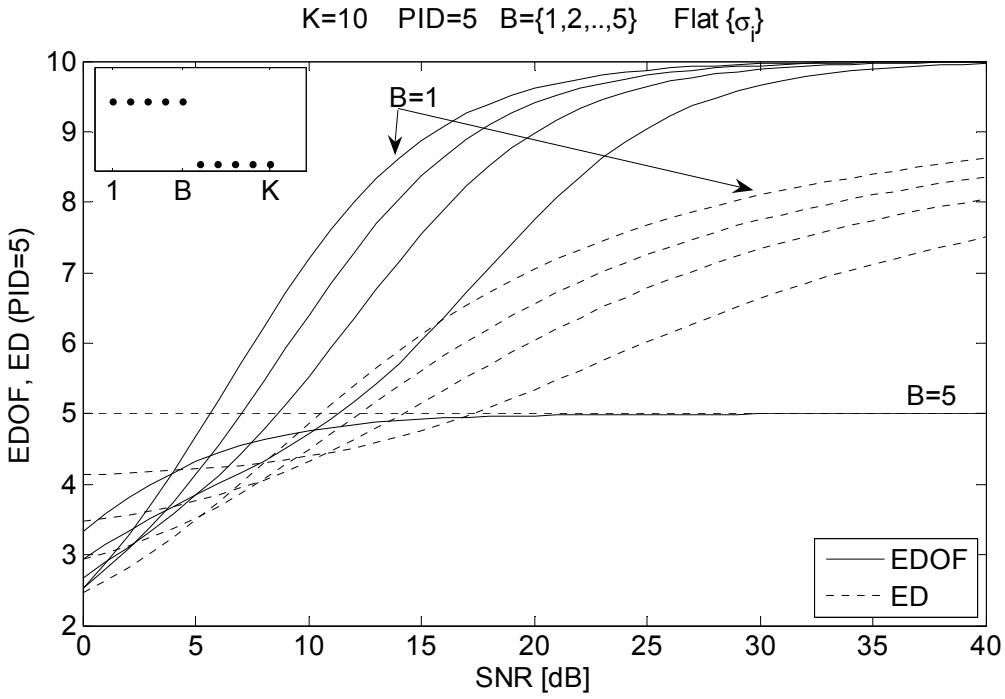

(a)

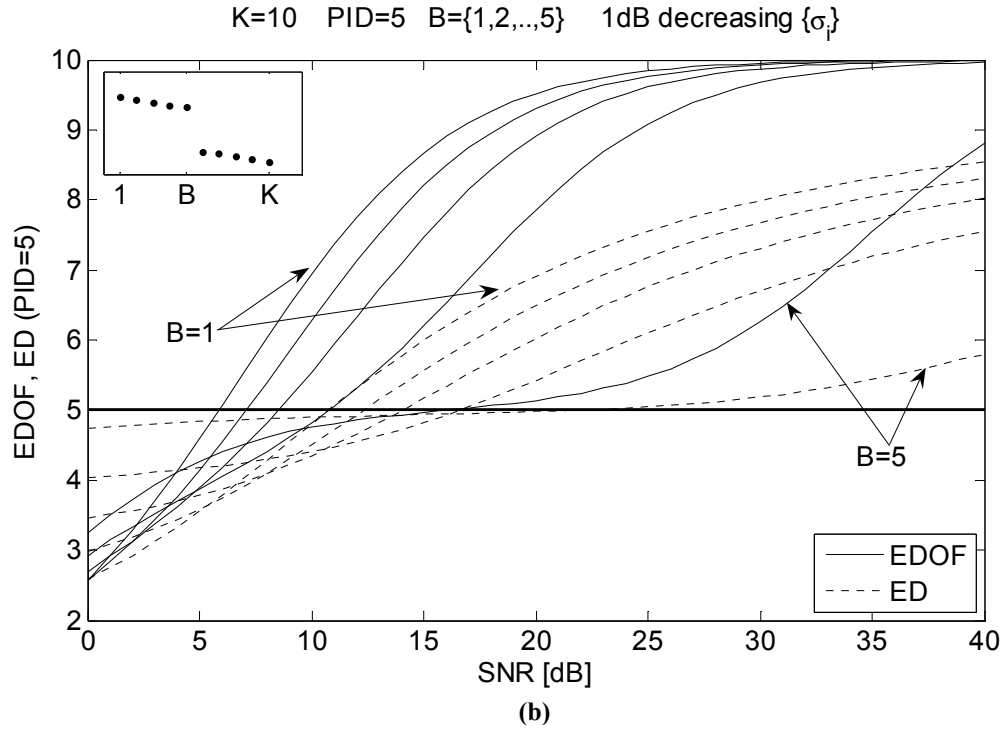

(b)

Fig. 2.3

EDOF, ED and PID comparison for case 2: (10,10) MIMO system and PID=5 Singular values distribution: (a) flat and (b) 1 dB decreasing.

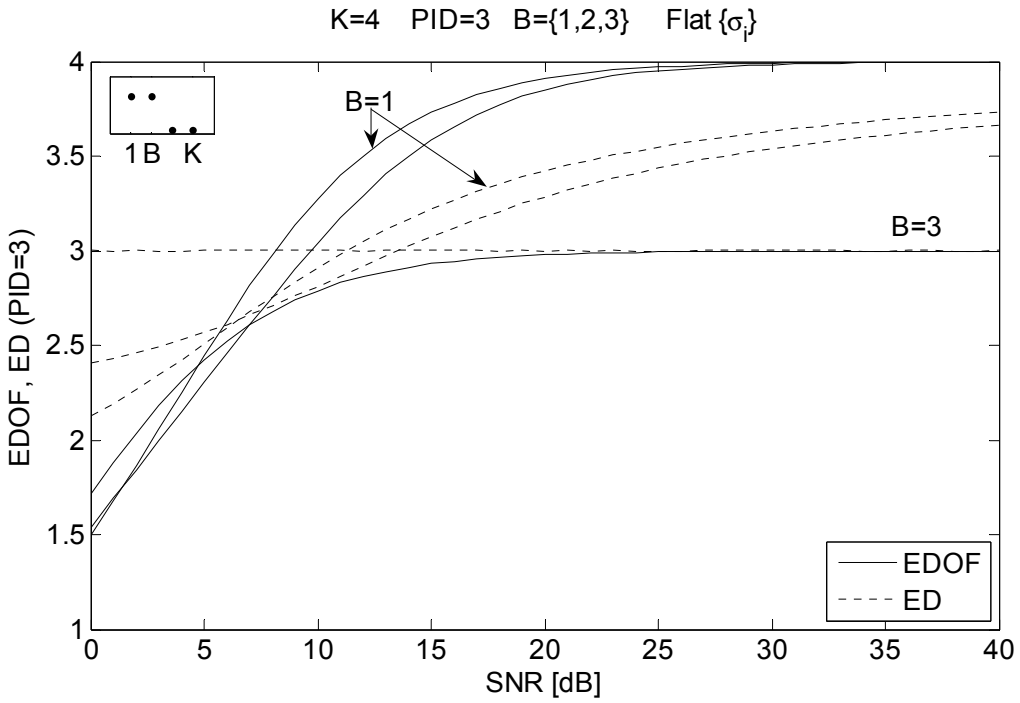

(a)

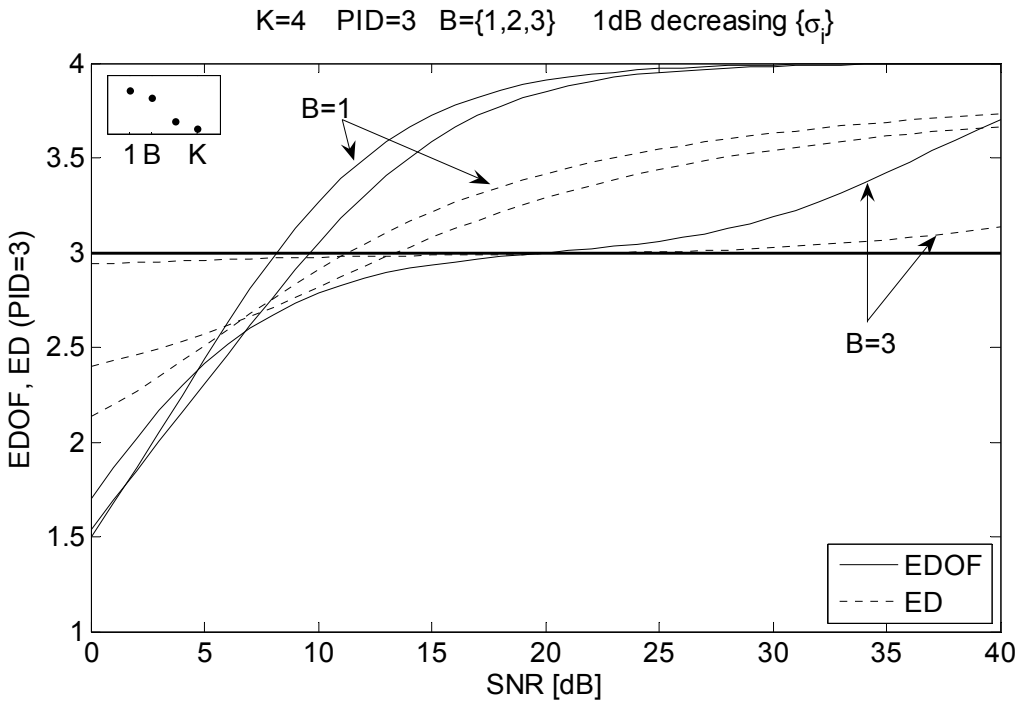

(b)

Fig. 2.4

EDOF, ED and PID comparison for case 3: (4,4) MIMO system and PID=3 Singular values distribution: (a) flat and (b) 1 dB decreasing.

As depicted in Fig. 2.2-4, for cases 1-3, there is a large discrepancy between PID and both metrics at high SNR. Compared to the fixed PID, ED is showing a smaller deviation than EDOF. The same observation holds at the low SNR extreme. This is due to the equivalence definition of ED (2.19) in contrast with the differential definition of EDOF (2.16) resulting in the previously mentioned asymptotic tendency to rank($\mathbf{H}$) and 0 at high and low SNR, respectively [SFGK00]. Within the moderate SNR range (10-20 dB), which is widely assumed in practical MIMO capacity evaluation, the discrepancy between PID and both metrics decreases, again ED being closer. In general, PID shows better agreement with both metrics as B approaches the fixed PID, which is likely to occur in the MIMO-DOF problems. In fact, the case of $B = 1$ along with flat *small* singular values represent the most severe pathological distribution of $\{\sigma_i\}$ having a given $\text{PID} \gg 1$ because the contribution of many weak channels largely exceeds that of a single strong one.

For the cases 4-6, we set $B = \text{PID}$ and we choose the 1 dB linearly decreasing distribution of the singular values. The 2 matrices $\mathbf{H}_1$ and $\mathbf{H}_2$ (of essentially the same dimensionality) have different sizes and ranks. The objective is to show the dependence of the SNR-based metrics, including the capacity, on the matrix size even when the 2 matrices have essentially the same dimensionality and Frobenius norm. The singular values of $\mathbf{H}_2$ encompass those of $\mathbf{H}_1$ (1 dB-decreasing "large" and "small" singular values), appended by additional 1 dB-decreasing "small" singular values as described in Table 2.3.

In order to correctly account for the relative power ratio of N channel matrices $\mathbf{H}_n, 1 \le n \le N$, the normalization (2.14) should be generalized to [JW04]

$$\bar{\mathbf{H}}_n = \frac{\mathbf{H}_n}{\sqrt{\sum_{n=1}^{N} \frac{\|\mathbf{H}_n\|_F^2}{N}} \Big/ \sqrt{N_R^{(n)} N_T^{(n)}}}, \tag{2.20}$$

where $\mathbf{H}_n \in \mathbb{C}^{N_R^{(n)} \times N_T^{(n)}}$. In each of cases 4-6, we have $N = 2$. However, since the Frobenius norms of $\mathbf{H}_1$ and $\mathbf{H}_2$ are essentially the same, both normalizations (2.14) and (2.20) yield approximately the same dimensionality and capacity results. In Fig. 2.5-7, we compare ED and EDOF to PID of $\mathbf{H}_1$ and $\mathbf{H}_2$. In addition, we plot the capacity values for $\mathbf{H}_1$ and $\mathbf{H}_2$ on the right vertical axis.

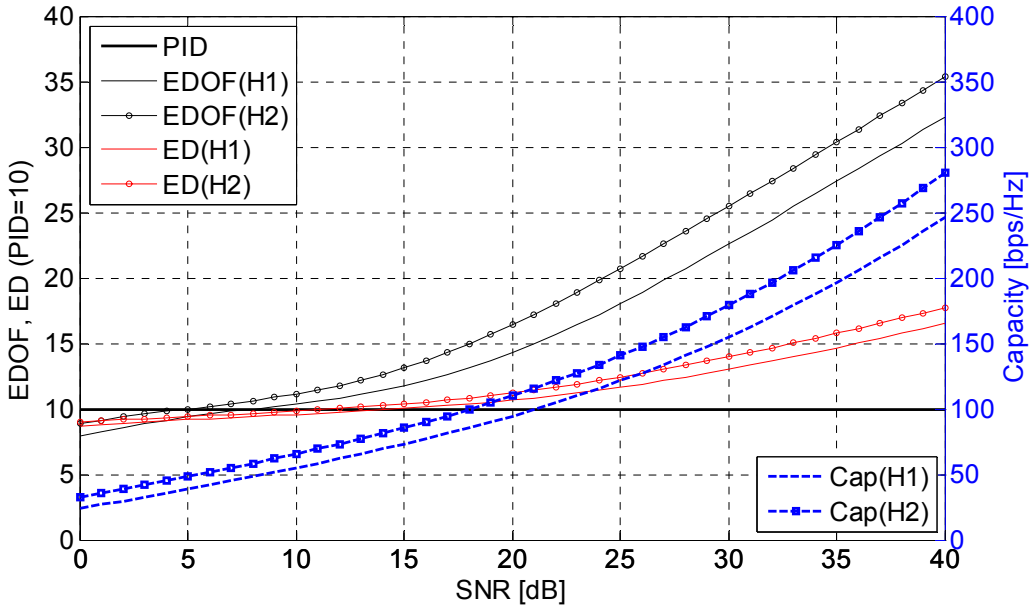

Fig. 2.5 (50,50) and (100,100) MIMO systems

Case 4 *B*=PID=10 1 dB decreasing singular values distribution

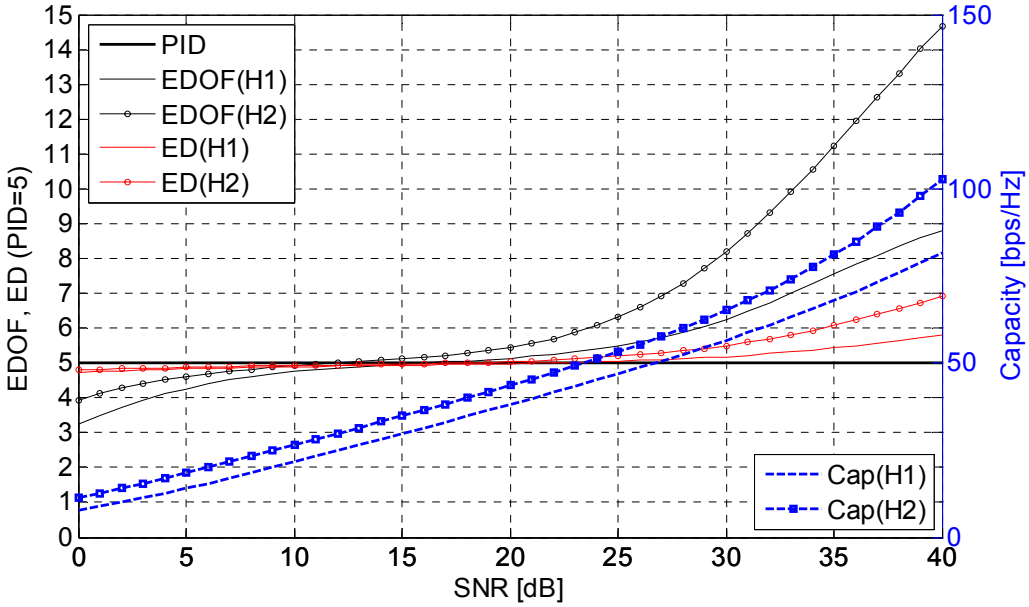

Fig. 2.6 (10,10) and (20,20) MIMO systems

Case 5 *B*=PID=5 1 dB decreasing singular values distribution

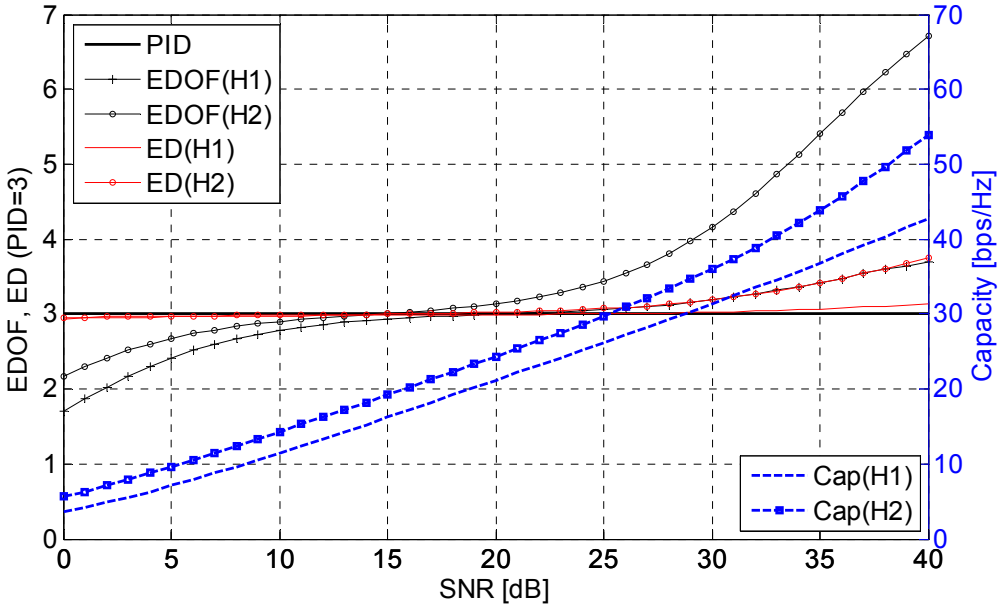

Fig. 2.7 (4,4) and (8,8) MIMO systems

Case 6 *B*=PID=3 1 dB decreasing singular values distribution

As expected, EDOF tends to the matrix rank at high SNR and ED shows smaller variation compared to the PID. Again, within the 10-20 dB range, the metrics results are close to the PID. However, Fig. 2.5-7 indicate a discrepancy in the EDOF and ED values, which can be quite large for EDOF, due to the different sizes of $\mathbf{H}_1$ and $\mathbf{H}_2$, even though their dimensionality is essentially the same. We also show the discrepancy of the capacity values for $\mathbf{H}_1$ and $\mathbf{H}_2$ on the right vertical axis. The matrix-size-dependent Frobenius normalization (2.14) or (2.20) can result in a wide discrepancy of the dimensionality result when evaluated through a power-dependent metric. Hence, cases 4-6 illustrate the merit of the proposed PID when it comes to the dimensionality evaluation for matrices of different sizes, as discussed in the previous section.

2.4 Summary and Discussion

In this chapter, we presented a well-defined metric for dimensionality comparison of multi-antenna systems. The power dependence is isolated and the PID depends only on the singular values distribution of the channel matrix. The PID was compared to 2 power-dependent metrics in the literature (EDOF and ED) showing that ED is closer to PID. Within the moderate SNR range (10-20 dB), PID is in good agreement with both ED and EDOF. We have also shown that the matrix-size-dependent normalization can yield significant discrepancy in the dimensionality evaluation by using power-dependent metrics, including the capacity. Both power- and matrix-size- independence properties make the PID suitable for the MIMO-DOF evaluation. Besides, in adaptive scenarios, the PID provides one single optimization parameter that can be fed back to the transmitter rather than the full channel entries or its singular values.

A recent power-independent metric, the ellipticity statistic (ES), has been proposed in the literature as a measure of *multipath richness* [SSEV06] rather than the DOF of MIMO systems. ES is defined as the ratio of the geometric and

arithmetic means of the non-zero $\{\sigma_i^2\}$. Therefore, $\mathrm{ES} = \dfrac{\left(\prod_{i=1}^{\mathrm{rank}(\mathbf{H})} \sigma_i^2\right)^{1/\mathrm{rank}(\mathbf{H})}}{\sum_{i=1}^{\mathrm{rank}(\mathbf{H})} \sigma_i^2 / \mathrm{rank}(\mathbf{H})}$ and has real positive values ≤ 1, with equality only in the case of partial isometry. ES is supposed to measure the deviation from the optimum case of even-distribution of the singular values. Nevertheless, ES is not suitable as a dimensionality measure, even after being multiplied by $\mathrm{rank}(\mathbf{H})$, for 2 reasons:

1. When there is at least one non-zero small singular value, the geometric mean significantly reduces the value of ES.
2. ES is very sensitive to $\mathrm{rank}(\mathbf{H})$ (i.e. matrix-size-dependent) even when the 2 different-size matrices have essentially the same dimensionality.

In [SSEV06], the non-positive quantity $\mathrm{rank}(\mathbf{H}) \cdot \log_2(\mathrm{ES})$ is regarded as the degradation of the mutual information compared to the optimum case (equi-useable channels), again with the exception of the rank deficient cases. For these reasons, in addition to the fact that it was not intended to measure the DOF, we did not include the ES in the numerical comparison.

It has been brought to our attention recently that another dimensionality metric can be defined, based on an entropy concept rather than the Schatten-norm equivalence, which exhibits *most* of the properties mentioned herein. This interesting metric provides similar results to the PID and needs more investigation [Kem07]. In the subsequent chapters, we will extensively use the PID for the dimensionality evaluation of MIMO systems in deterministic scenarios. A complete chapter is dedicated to investigate the multi-polarization MIMO systems, using the PID, showing interesting results for tripole and hexapole systems. Another chapter is dedicated to the MIMO-DOF evaluation for a size-specific aperture (1D, 2D or 3D) including the multi-polarization effect and thus investigating the ultimate dimensionality using all the available spatial diversity.

Chapter 3
Electromagnetic Modeling of Deterministic Indoor Multi-Antenna Systems

We present in this chapter an electromagnetic modeling of deterministic indoor environments for MIMO systems. We begin by using the angular domain modeling. Then, we apply the high frequency approximation (ray modeling) and plane wavefront approximation (PWA). We follow this by exhaustively including the full available diversity (multi-polarization and space-diversity) in the model. We also discuss the image ray tracing (IRT) algorithm, which is employed to simulate the MIMO systems in lossy-walls rectangular environments.

Next, we provide numerical results for some scenarios in a rectangular structure. We use the IRT algorithm in a lossy-walls environment to obtain the PID when using 1D and 2D arrays of various sizes. We also make a comparison

of the PID results with those obtained in a similar PEC wave-guide using modal analysis.

3.1 Ray Modeling of Electromagnetic Propagation in MIMO Systems

3.1.1 Symbols and Notation

We state hereafter the symbols and notations used in the modeling for easy reference.

- (r,t): (Rx,Tx) link indices superscripts respectively
- (m,n): (Rx,Tx) elements (i.e. ports) indices subscripts respectively
- $\bar{\mathbf{D}}$: denotes a dyad
- $\mathbf{M}$: boldface upper case denotes a matrix
- m_{ij}: denotes a scalar entry within $\mathbf{M}$
- $[m_{ij}]$: matrix constructed from the entries m_{ij}
- $\mathbf{v}$: boldface lower case denotes a vector (in the exception of the electric and magnetic field vectors)
- $[v_k]$: vector constructed from the components v_k
- $\Omega^{(r)}$: Rx solid spherical direction $(\theta^{(r)},\varphi^{(r)})$
- $\Omega^{(t)}$: Tx solid spherical direction $(\theta^{(t)},\varphi^{(t)})$
- $\bar{\mathbf{G}}_{mn}^{(rt)}(\Omega_m^{(r)},\Omega_n^{(t)})$: Generic *environment dyad* relating the n^{th} Tx field radiated at $\Omega_n^{(t)}$ to the m^{th} Rx field received at $\Omega_m^{(r)}$
- $\bar{\mathbf{G}}_{mnl}^{(rt)}$: Environment ray-dyad relating the n^{th} Tx field to the m^{th} Rx field along the l^{th} ray path

- $\bar{\mathbf{G}}^{(rt)}(\Omega^r, \Omega^t)$: array phase-centre-to-phase-centre (PC-to-PC) dyad obtained by applying the plane wavefront approximation (PWA). It relates the Tx field radiated at $\Omega^{(t)}$ to the Rx field received at $\Omega^{(r)}$.
- $\mathbf{a}_m^{(r)}$ and $\mathbf{a}_n^{(t)}$: position vector of the m^{th} and n^{th} array element referred to the Rx/Tx-PC, respectively
- $\hat{\mathbf{a}}_l^{(r)}$ and $\hat{\mathbf{a}}_l^{(t)}$: unit vectors for the l^{th} ray direction of arrival/departure (DOA/DOD) referred to the Rx/Tx-PC, respectively, under the PWA
- $\hat{\mathbf{a}}_\theta$ and $\hat{\mathbf{a}}_\varphi$: transverse directions unit vectors in the spherical coordinate system.
- $\mathbf{e}$: far-field pattern/polarization vector (also known as the *effective length* or height). For a transmitting antenna having a current I_{in} at its terminals, the radiated far-field $\overline{E}$ is related to $\mathbf{e}$ by $\overline{E} \equiv -j\,\omega\mu_0 I_{in} \frac{e^{-jk_0 r}}{4\pi r}\mathbf{e}$. For a receiving antenna, the open-circuit voltage $V^{(oc)}$ is related to the incident electric field $\overline{E}^{(i)}$ by $V^{(oc)} = \mathbf{e} \cdot \overline{E}^{(i)}$. In spherical coordinates, the vector effective length has 2 transverse components such that $\mathbf{e} = e_\theta(\theta,\varphi)\hat{\mathbf{a}}_\theta + e_\varphi(\theta,\varphi)\hat{\mathbf{a}}_\varphi$ [Bal97, Mey00].
- $\{\bullet\}^T$ and $\{\bullet\}^H$: denotes the transpose and conjugate transpose operation, respectively
- (N_R, N_T): number of (Rx,Tx) antennas respectively
- $\mathbf{y}$: Rx signal vector $\in \mathbb{C}^{N_R \times 1}$
- $\mathbf{x}$: Tx signal vector $\in \mathbb{C}^{N_T \times 1}$
- $\boldsymbol{\eta}$: iid spatially white Gaussian noise vector at Rx $\in \mathbb{C}^{N_R \times 1}$
- $\mathbf{H}$: narrowband channel matrix $\in \mathbb{C}^{N_R \times N_T}$
- $\sigma\{\bullet\}$: singular values of the matrix

3.1.2 Angular Domain Modeling of a Deterministic Environment

As mentioned in chapter 1, the MIMO system model, in narrowband operation, is given by

$$\mathbf{y} = \mathbf{H}\mathbf{x} + \boldsymbol{\eta}. \tag{3.1}$$

Assuming a propagation environment with a continuum of solid angles at the transmit/receive ends, the channel matrix entry h_{mn} is expressed as [e.g. ZFDW00, MJW05]

$$h_{mn} = \oint_{\Omega_m^{(r)}} d\Omega_m^{(r)} \oint_{\Omega_n^{(t)}} d\Omega_n^{(t)} \mathbf{e}_m^{(r)T}(\Omega_m^{(r)}) \cdot \bar{\mathbf{G}}_{mn}^{(rt)}(\Omega_m^{(r)}, \Omega_n^{(t)}) \cdot \mathbf{e}_n^{(t)}(\Omega_n^{(t)}). \tag{3.2}$$

Careful examination of (3.2) reveals 2 facts:

1. We are using the angular domain (discussed in appendix C) to compute h_{mn}. The general angular domain, which is also called the k-domain, includes both the far-field traveling wave components (visible angular domain) and the near-field evanescent ones.
2. The environment effect (defined to include the transmit/receive geometrical configuration as well as the scatterers/boundaries geometrical and electrical properties), is included in the *environment dyad* $\bar{\mathbf{G}}_{mn}^{(rt)}(\Omega_m^{(r)}, \Omega_n^{(t)})$ for each transmit/receive angular direction. The transmit/receive antenna properties (pattern and polarization) are included in effective lengths $\mathbf{e}_n^{(t)}(\Omega_n^{(t)})$ and $\mathbf{e}_m^{(r)}(\Omega_m^{(r)})$ according to the transmit/receive angular direction.

The objective is to formulate the dependence of h_{mn} on the site-specific environment. We will apply some assumptions and approximations in order to express (3.2) in a more useful form, which explicitly shows all the available space diversity for a given set-up. First, we assume far-field operation, such that the transmit and receive are sufficiently remote to neglect the near-field (evanescent components) effect. Then, we apply the high-frequency approximation [Bal89]. Consequently, the solid angles continuum is discretized

since the transmitted and received waves are modeled as ray tubes. Therefore, (3.2) can be expressed in a double summation form

$$h_{mn} = \sum_{l_m^{(r)}=1}^{\infty} \sum_{l_n^{(t)}=1}^{\infty} \mathbf{e}_m^{(r)T}(l_m^{(r)}) \cdot \bar{\mathbf{G}}_{mn}^{(rt)}(l_m^{(r)}, l_n^{(t)}) \cdot \mathbf{e}_n^{(t)}(l_n^{(t)}), \tag{3.3}$$

where $l_m^{(r)}$ and $l_n^{(t)}$ denote the receive/transmit ray order for the elements m and n, respectively. Moreover, we assume that each ray is *deterministically* known and traced. This modeling is the deterministic equivalent of the joint correlation of angle of arrival (AOA) and angle of departure (AOD) in the statistical counterpart (e.g. [XCV04]). In other words, by using the deterministic modeling (through ray tracing or other deterministic techniques e.g. modal analysis), there is no need (and it is not correct) to include a transmit/receive correlation matrix, which would have been required if we had used a stochastic "environmentless" channel matrix. The deterministic ray assumption further simplifies (3.3) to only one summation, having l as the ray index

$$h_{mn} = \sum_{l=1}^{\infty} \mathbf{e}_{ml}^{(r)T} \cdot \bar{\mathbf{G}}_{mnl}^{(rt)} \cdot \mathbf{e}_{nl}^{(t)}. \tag{3.4}$$

Next, we apply the plane wavefront approximation (PWA) at both transmit/receive ends [JI05]. Accordingly, the plane wave modeling takes place only between the transmit/receive PCs, independent of (m,n). In order to model the transmit/receive array geometry, we add a phase factor based on the PWA. Thus, the environment ray-dyad $\bar{\mathbf{G}}_{mnl}^{(rt)}$ can be expressed as

$$\bar{\mathbf{G}}_{mnl}^{(rt)} = \bar{\mathbf{G}}_{l}^{(rt)} \exp[jk_0(\mathbf{a}_m^{(r)} \cdot \hat{\mathbf{a}}_l^{(r)} + \mathbf{a}_n^{(t)} \cdot \hat{\mathbf{a}}_l^{(t)})], \tag{3.5}$$

where $\bar{\mathbf{G}}_{l}^{(rt)}$ represents the environment PC-to-PC ray-dyad for the l^{th} ray and k_0 is the free space wave number. The array phase delay has the same sign at both transmit/receive ends since, by reciprocity, both transmit/receive arrays are considered operating in the transmit mode.

From (3.4) and (3.5), we have

$$h_{mn} = \sum_{l=1}^{\infty} \mathbf{e}_{ml}^{(r)T} \cdot \bar{\mathbf{G}}_l^{(rt)} \cdot \mathbf{e}_{nl}^{(t)} \exp[jk_0(\mathbf{a}_m^{(r)} \cdot \hat{\mathbf{a}}_l^{(r)} + \mathbf{a}_n^{(t)} \cdot \hat{\mathbf{a}}_l^{(t)})]. \quad (3.6)$$

Moreover, for each ray, the environment PC-to-PC dyad $\bar{\mathbf{G}}_l^{(rt)}$ can be separated into a free space spherical propagation factor $\exp(-jk_0R_l)/R_l$, where R_l is the distance traveled by the l^{th} ray, and a dyad $\bar{\mathbf{D}}_l^{(rt)}$ encompassing the other propagation mechanisms (reflection, transmission, diffraction) so that

$$\bar{\mathbf{G}}_l^{(rt)} = \frac{\exp(-jk_0R_l)}{R_l} \bar{\mathbf{D}}_l^{(rt)}, \quad (3.7)$$

and accordingly, from (3.6) and (3.7),

$$h_{mn} = \sum_{l=1}^{\infty} \mathbf{e}_{ml}^{(r)T} \cdot \bar{\mathbf{D}}_l^{(rt)} \cdot \mathbf{e}_{nl}^{(t)} \frac{\exp[jk_0(\mathbf{a}_m^{(r)} \cdot \hat{\mathbf{a}}_l^{(r)} + \mathbf{a}_n^{(t)} \cdot \hat{\mathbf{a}}_l^{(t)} - R_l)]}{R_l}. \quad (3.8)$$

From (3.8), we can readily link the following propagation effects with each specific parameter as follows:

- Environment electrical properties (scattering processes including material properties and geometrical setup): $\bar{\mathbf{D}}_l^{(rt)}$
- Environment geometry and set-up: any parameter with the subscript l (related to each ray direction), namely, $\bar{\mathbf{D}}_l^{(rt)}$, $\mathbf{e}_{ml}^{(r)}$, $\mathbf{e}_{nl}^{(t)}$, $\hat{\mathbf{a}}_l^{(r)}$, $\hat{\mathbf{a}}_l^{(t)}$ and R_l
- Space diversity: $\mathbf{a}_m^{(r)}$ and $\mathbf{a}_n^{(t)}$
- Pattern/Polarization diversity: $\mathbf{e}_{ml}^{(r)}$ and $\mathbf{e}_{nl}^{(t)}$

The environment propagation model in (3.8) can be cast in a 3D matrix form such that

$$\mathbf{H}^{(3D)} = [h_{mnl}] \quad (3.9a)$$

$$h_{mnl} = \mathbf{e}_{ml}^{(r)T} \cdot \bar{\mathbf{D}}_l^{(rt)} \cdot \mathbf{e}_{nl}^{(t)} \frac{\exp[jk_0(\mathbf{a}_m^{(r)} \cdot \hat{\mathbf{a}}_l^{(r)} + \mathbf{a}_n^{(t)} \cdot \hat{\mathbf{a}}_l^{(t)} - R_l)]}{R_l}. \quad (3.9b)$$

$\mathbf{H}$ can be obtained from $\mathbf{H}^{(3D)}$ through the *coherent* summation over the l index (narrowband channel)

$$\mathbf{H} = \sum_{l=1}^{\infty} \mathbf{H}_l \tag{3.10a}$$

$$\mathbf{H}_l = [h_{mn}]_l , \tag{3.10b}$$

where each matrix "page" $\mathbf{H}_l \in \mathbb{C}^{N_R \times N_T}$ models a one-ray propagation channel for the l^{th} ray path.

3.1.3 Identical Radiating Elements: Multi-Keyhole Matrix Form

From (3.9b), we re-write h_{mnl} in a parametric form

$$h_{mnl} = p_{mnl}^{(rt)} v_{ml}^{(r)} v_{nl}^{(t)} \frac{\exp(-jk_0 R_l)}{R_l} \tag{3.11a}$$

$$p_{mnl}^{(rt)} = \mathbf{e}_{ml}^{(r)T} \cdot \overline{\mathbf{D}}_l^{(rt)} \cdot \mathbf{e}_{nl}^{(t)} \tag{3.11b}$$

$$v_{ml}^{(r)} = \exp[jk_0 \mathbf{a}_m^{(r)} \cdot \hat{\mathbf{a}}_l^{(r)}] \tag{3.11c}$$

$$v_{nl}^{(t)} = \exp[jk_0 \mathbf{a}_n^{(t)} \cdot \hat{\mathbf{a}}_l^{(t)}]. \tag{3.11d}$$

In (3.11) $p_{mnl}^{(rt)}$ models the pattern/polarization diversity as well as the environment propagation. The parameters $v_{ml}^{(r)}$ and $v_{nl}^{(t)}$ model the receive/transmit space-diversity *per ray*. It is interesting to note that, for each ray, $v_{ml}^{(r)}$ and $v_{nl}^{(t)}$ have no magnitude effect (only a phase retardation effect). However, this phase-only characteristic is powerful enough to account for a major source of the MIMO diversity.

The deterministic model developed thus far is general for any number of transmit/receive elements, any pattern/polarization per element and any environment subject to the previously mentioned assumptions (far-field, high-frequency and PWA). Our interest in this research is to investigate the EM-dimensionality based on EM-vectorial sampling. Therefore, we make one more assumption: all the transmit elements are identical; and the same goes for the receive elements. In this sub-section we consider arrays of identical elements

having the same polarization. In the next sub-section, we consider arrays of identical elements, which exhaustively include all polarizations.

According to the identical-element same-polarization assumption, the (m,n) indices are omitted from $\mathbf{e}_{ml}^{(r)}$, $\mathbf{e}_{nl}^{(t)}$ and $p_{mnl}^{(rt)}$ in (3.11). Moreover, we define the receive and transmit phase shift vectors, $\mathbf{v}_l^{(r)}$ and $\mathbf{v}_l^{(t)}$, respectively, such that

$$\begin{aligned} \mathbf{v}_l^{(r)} &= [v_m^{(r)}]_l \\ \mathbf{v}_l^{(t)} &= [v_n^{(t)}]_l \,. \end{aligned} \tag{3.12}$$

Hence, (3.10) is expressed as

$$\mathbf{H} = \sum_{l=1}^{\infty} p_l^{(rt)} \frac{\exp(-jk_0 R_l)}{R_l} \mathbf{v}_l^{(r)} \mathbf{v}_l^{(t)T} \,. \tag{3.13}$$

For each term of (3.13), $\mathbf{v}_l^{(r)} \mathbf{v}_l^{(t)T}$ forms a matrix of rank 1, which is known in the literature as the *keyhole dyad effect* having only 1 DOF (e.g. [LCV01, CFGV02, ATM06]). Therefore, (3.13) suggests that we can model the MIMO channel matrix, when there are identical elements at each end, in the *multi-keyhole form* which can be re-written as a product of 3 matrices [LL06a, LL06b]

$$\mathbf{H} = \mathbf{H}^{(r)} \mathbf{A}^{(rt)} \mathbf{H}^{(t)T} \,, \tag{3.14a}$$

where, for L rays, the matrices $\mathbf{H}^{(r)} \in \mathbb{C}^{N_R \times L}$, $\mathbf{H}^{(t)} \in \mathbb{C}^{N_T \times L}$ and $\mathbf{A}^{(rt)} \equiv \mathrm{diag}\left([\alpha_1^{(rt)} ... \alpha_L^{(rt)}]\right) \in \mathbb{C}^{L \times L}$ are constructed such that

$$\mathbf{H}^{(r)} = \left[\mathbf{v}_1^{(r)} ... \mathbf{v}_L^{(r)} \right] \tag{3.14b}$$

$$\mathbf{H}^{(t)} = \left[\mathbf{v}_1^{(t)} ... \mathbf{v}_L^{(t)} \right] \tag{3.14c}$$

$$\begin{aligned} \alpha_l^{(rt)} &= p_l^{(rt)} \frac{\exp(-jk_0 R_l)}{R_l} \\ &= \mathbf{e}_l^{(r)T} \cdot \bar{\mathbf{D}}_l^{(rt)} \cdot \mathbf{e}_l^{(t)} \frac{\exp(-jk_0 R_l)}{R_l} \qquad l \in \{1,2,...,L\} \end{aligned} \tag{3.14d}$$

In order to appreciate the importance of the form (3.14a) for MIMO-dimensionality evaluation, we have recourse to the PID matrix product inequality in chapter 2. From (2.8), we know that the upper bound dimensionality (PID) of a matrix product is the smallest dimensionality of each individual matrix (mostly true for large PID values). Consequently, we have

$$\mathrm{PID}(\mathbf{H}) \le \min\{\mathrm{PID}(\mathbf{H}^{(r)}), \mathrm{PID}(\mathbf{A}^{(rt)}), \mathrm{PID}(\mathbf{H}^{(t)})\}. \tag{3.15}$$

$\mathrm{PID}(\mathbf{H}^{(r)})$ and $\mathrm{PID}(\mathbf{H}^{(t)})$ are governed by the aperture size (1D, 2D or 3D) and orientation at the receive/transmit ends, respectively, as will be discussed in chapter 5. On the other hand, $\mathrm{PID}(\mathbf{A}^{(rt)})$ is governed by the multipath richness of the environment, which depends on the number of rays (L) and the significance of their contribution based on the value of $\alpha_l^{(rt)}$. The latter depends on the propagation mechanism, the setup geometry and the pattern/polarization of the radiation elements. Therefore, for a highly reflective environment such as the PEC corridor, $|\alpha_l^{(rt)}|$ is large over many rays leading to a large value of $\mathrm{PID}(\mathbf{A}^{(rt)})$ and the global dimensionality is bounded by $\min\{\mathrm{PID}(\mathbf{H}^{(r)}), \mathrm{PID}(\mathbf{H}^{(t)})\}$. On the other hand, for poor multipath (e.g. keyhole) environments, we get few significant values of $|\alpha_l^{(rt)}|$, leading to a small global dimensionality bounded by $\mathrm{PID}(\mathbf{A}^{(rt)})$. Also, it is obvious that a ray of a higher reflection order in lossy environments suffers from a large decay due to the combined effect of longer traveled distance and the reflection loss (many bounces).

3.1.4 Exhaustive Identical Polarization: Kronecker Product Form

As a final step to exhaustively include all the polarization diversity in the identical-element model (3.13), we construct the polarization channel matrix $\mathbf{P}_l^{(rt)} \in \mathbb{C}^{6\times 6}$ for the l^{th} ray. $\mathbf{P}_l^{(rt)}$ models the PC-to-PC channel, *per ray*, of a hexapole MIMO system (collocated electric and magnetic polarized point

radiators making 6 independent ports at the transmit/receive phase-centres) [AMC01, SJW04], which will be discussed in mpre details in chapter 4. $\mathbf{P}_l^{(rt)}$ is constructed such that

$$\mathbf{P}_l^{(rt)} = [p_{ij}^{(rt)}]_l , \tag{3.16}$$

where each entry $p_{ijl}^{(rt)}$ characterizes the PC-to-PC contribution of the l^{th} ray path between the j^{th} polarized transmit to the i^{th} polarized receive infinitesimal dipole. According to (3.11b), $p_{ijl}^{(rt)}$ is given by

$$p_{ijl}^{(rt)} = \mathbf{e}_{il}^{(r)T} \cdot \bar{\mathbf{D}}_l^{(rt)} \cdot \mathbf{e}_{jl}^{(t)} . \tag{3.17}$$

The indices j and i take the values of $\{1,2,3\}$ to denote an electric dipole and $\{4,5,6\}$ to denote a magnetic dipole excitation/response, respectively [SJW04]. Based on the ray-polarization matrix $\mathbf{P}_l^{(rt)}$, the full available diversity (pattern, polarization and space) is modeled for each matrix page $\mathbf{H}_l$ by the Kronecker product

$$\mathbf{H}_l = \mathbf{P}_l^{(rt)} \otimes \mathbf{v}_l^{(r)} \otimes \mathbf{v}_l^{(t)T} \frac{\exp(-jk_0 R_l)}{R_l} . \tag{3.18}$$

It is interesting to note that all the entries $p_{ijl}^{(rt)}$ in (3.17) depend on the same ray-environment dyad $\bar{\mathbf{D}}_l^{(rt)}$, which is a direct consequence of the collocation of the hexapole. From a simulation perspective, this common dependence is very useful, because the ray tracing has to be performed only once (evaluating $\bar{\mathbf{D}}_l^{(rt)}$) for the 36 entries of the ray-hexapole matrix $\mathbf{P}_l^{(rt)}$. Then, $\mathbf{e}_{il}^{(r)}$ and $\mathbf{e}_{jl}^{(t)}$ are evaluated in situ at the receive/transmit ends and take care of the corresponding pattern/polarization characteristics, independently of the propagation environment.

An important fact has to be stated regarding the rank and dimensionality of $\mathbf{H}_l$ in (3.18). It is well-known that any far-field electromagnetic wave has a polarization diversity of 2 (commonly known as the vertical and horizontal polarization in free space, see appendix C). Hence, $\text{rank}(\mathbf{P}_l^{(rt)}) = 2$ even when using a hexapole or a tripole system [SJW04]. This far-field rank deficiency results from the *algebraic* dependence between the electric and magnetic fields as well as the absence of the radial field components, which is discussed in more details in chapter 4. Consequently, $\text{PID}(\mathbf{P}_l^{(rt)}) \le 2$, where the equality holds if and only if the 2 transverse electric field components at the receive PC have the same magnitude after all the scattering processes encountered during the propagation. On the other hand, the keyhole dyad $\mathbf{v}_l^{(r)} \otimes \mathbf{v}_l^{(t)T}$ forms a matrix of rank 1 as was previously stated. From the Kronecker product property of the PID in chapter 2 (2.6), we readily get

$$\text{PID}(\mathbf{P}_l^{(rt)} \otimes \mathbf{v}_l^{(r)} \otimes \mathbf{v}_l^{(t)T}) \le 2, \tag{3.19a}$$

and therefore,

$$\text{PID}(\mathbf{H}_l) \le 2. \tag{3.19b}$$

In spite of the rank-deficiency of each individual component $\mathbf{H}_l$, the coherent sum (3.10a) forming $\mathbf{H}$ has, *in general*, a higher rank. This can be shown through singular values inequalities. Let $\mathbf{H}_1$ and $\mathbf{H}_2$ be 2 matrices of size $N_R \times N_T$, where $K = \min\{N_R, N_T\}$. Then, it is shown in [HJ94 page 178] that

$$\begin{aligned} &\sigma_{i+j-1}\{\mathbf{H}_1 + \mathbf{H}_2\} \le \sigma_i\{\mathbf{H}_1\} + \sigma_j\{\mathbf{H}_2\} \\ &\text{for} \quad 1 \le i, j \le K \quad \text{and} \quad i + j \le K + 1 \end{aligned}. \tag{3.20}$$

Applying (3.20) on the 2 environment/polarization matrices $\mathbf{P}_1^{(rt)}$ and $\mathbf{P}_2^{(rt)}$ of rank 2, we get the following inequality for the third singular value of their sum

$$\sigma_3\{\mathbf{P}_1^{(rt)} + \mathbf{P}_2^{(rt)}\} \le \min\left\{\sigma_1\{\mathbf{P}_1^{(rt)}\}, \sigma_1\{\mathbf{P}_2^{(rt)}\}, \sigma_2\{\mathbf{P}_1^{(rt)}\} + \sigma_2\{\mathbf{P}_2^{(rt)}\}\right\}. \tag{3.21}$$

Hence, (3.21) shows that there is a *possibility*, although it is not guaranteed, that we get a non-zero third singular value of the sum. We list 2 counter-examples showing that the sum of 2 rank-deficient matrices can result in another rank-deficient matrix possibly of a lower rank.

- Suppose $\mathbf{A}_2 = \gamma \mathbf{A}_1$, where $\mathbf{A}_1$ is of rank 2 and γ is a constant. Clearly, $\sigma_3\{\mathbf{A}_1 + \mathbf{A}_2\} = 0$ and the sum is a rank-deficient matrix of the same rank.
- Consider the 2 diagonal matrices $\mathbf{A}_1 = \text{diag}(a, b, 0, 0, 0, 0)$ and $\mathbf{A}_2 = \text{diag}(a, -b, 0, 0, 0, 0)$, both of rank 2. Their summation will result in a matrix of rank 1. This can model a case when a destructive interference is only affecting one of the transverse field components.

However, the worst case possibilities mentioned above are not likely to occur in a propagation environment, particularly when we are summing a large number of matrices of comparable Frobenius norms. Typically, we expect a higher rank for $\mathbf{H} = \sum_{l=1}^{\infty} \mathbf{H}_l$.

3.2 The Environment Ray-Dyad in a Lossy-Wall Rectangular Environment

We provide in this section the propagation model in a rectangular lossy structure based on Image Ray Tracing (IRT). Starting from (3.7), we will expand $\bar{\mathbf{G}}_l^{(rt)}$ in the case of a 3D rectangular environment having lossy walls. The propagation mechanism considered, other than direct Line-Of-Sight (LOS) rays, is the off-the-walls reflections. Diffraction at corners and wall edges are not considered. The propagation prediction approach is Image Ray Tracing (IRT). For the l^{th} ray path, there is a total of $K(l)$ reflections taking place between the transmit and receive ends. The following notations concern the l^{th} ray path, so we omit the subscript l for notational convenience:

- $(-,+)$: superscripts to denote the vector before and after the k^{th} reflection, respectively
- $(\mathbf{e}_k^-, \mathbf{e}_k^+)$: electric field vector (2 transverse components) before and after the k^{th} reflection, respectively
- $(\perp_k, \|_k)$: subscripts denoting the 2 components (perpendicular and parallel) to the plane of incidence at the k^{th} reflection, respectively
- $(e_{\perp_k}, e_{\|_k})$: the perpendicular and parallel electric field components to the plane of incidence at the k^{th} reflection, respectively
- $(\Gamma_{\perp_k}, \Gamma_{\|_k})$: the perpendicular and parallel plane reflection coefficients at the k^{th} reflection, respectively
- $(\hat{\mathbf{a}}_{\perp_k}^-, \hat{\mathbf{a}}_{\|_k}^-)$: the perpendicular and parallel unit vectors, respectively, before the k^{th} reflection
- $(\hat{\mathbf{a}}_{\perp_k}^+, \hat{\mathbf{a}}_{\|_k}^+)$: the perpendicular and parallel unit vectors, respectively, after the k^{th} reflection
- $\bar{\mathbf{D}}_k$: k^{th} 2×2 reflection dyad

The k^{th} reflection dyad is given by

$$\bar{\mathbf{D}}_k = \Gamma_{\perp_k} \hat{\mathbf{a}}_{\perp_k}^+ \hat{\mathbf{a}}_{\perp_k}^- + \Gamma_{\|_k} \hat{\mathbf{a}}_{\|_k}^+ \hat{\mathbf{a}}_{\|_k}^-, \tag{3.22}$$

and the transverse electric field vectors along the ray path before and after the k^{th} reflection are related by

$$\mathbf{e}_k^+ = \bar{\mathbf{D}}_k \cdot \mathbf{e}_k^-. \tag{3.23}$$

Over the ray segment between the 2 consecutive reflections, k and $k+1$, the electric fields $\mathbf{e}_k^+$ and $\mathbf{e}_{k+1}^-$ differ only by a spherical wave propagation factor, Therefore,

$$\mathbf{e}_{k+1}^- = \mathbf{e}_k^+ \exp(-jk_0 R_{k,k+1}) \frac{R_{0,k}}{R_{0,k+1}}, \tag{3.24}$$

where $R_{k,k+1}$ is the traveled distance between the 2 reflections and $R_{0,k}$ is the traveled distance between the transmit phase-centre and the k^{th} reflection point. Through recursive combination of (3.23) and (3.24) by applying left dyad multiplication, the environment PC-to-PC ray-dyad $\bar{\mathbf{G}}_l^{(rt)}$ in (3.7) is readily obtained

$$\begin{aligned}\bar{\mathbf{G}}_l^{(rt)} &= \frac{\exp(-jk_0R_l)}{R_l}\prod_{k=1}^{K(l)}\bar{\mathbf{D}}_{kl} \\ &= \frac{\exp(-jk_0R_l)}{R_l}\prod_{k=1}^{K(l)}\left(\Gamma_{\perp_{kl}}\hat{\mathbf{a}}_{\perp_{kl}}^{+}\hat{\mathbf{a}}_{\perp_{kl}}^{-}+\Gamma_{\parallel_{kl}}\hat{\mathbf{a}}_{\parallel_{kl}}^{+}\hat{\mathbf{a}}_{\parallel_{kl}}^{-}\right)\end{aligned}, \tag{3.25}$$

where R_l is the total PC-to-PC traveled distance along the l^{th} ray path. Thus, the first L pages $\mathbf{H}_l$ of *sufficiently strong Frobenius norm* will determine, to a good approximation, the ultimate channel matrix $\mathbf{H}$ such that

$$\mathbf{H} \approx \sum_{l=1}^{L}\mathbf{H}_l \ . \tag{3.26}$$

For computational consideration in the IRT simulation, we make a fast ray-ranking based on the traveled distance and the number of reflections per ray: a shorter traveled distance *and* a smaller number of reflections designate a more significant ray. We do not consider the pattern/polarization mismatch for the sake of time-efficiency and the ranking is performed prior to the actual ray tracing (it depends only on the room geometry and transmit/receive setup). Fig. 3.1 depicts one ray traced in a rectangular structure. In Fig. 3.2, the flow chart of the recursive reflection tracing algorithm is described. More details regarding the IRT used in the simulation of lossy rectangular structures can be found in [Eln03].

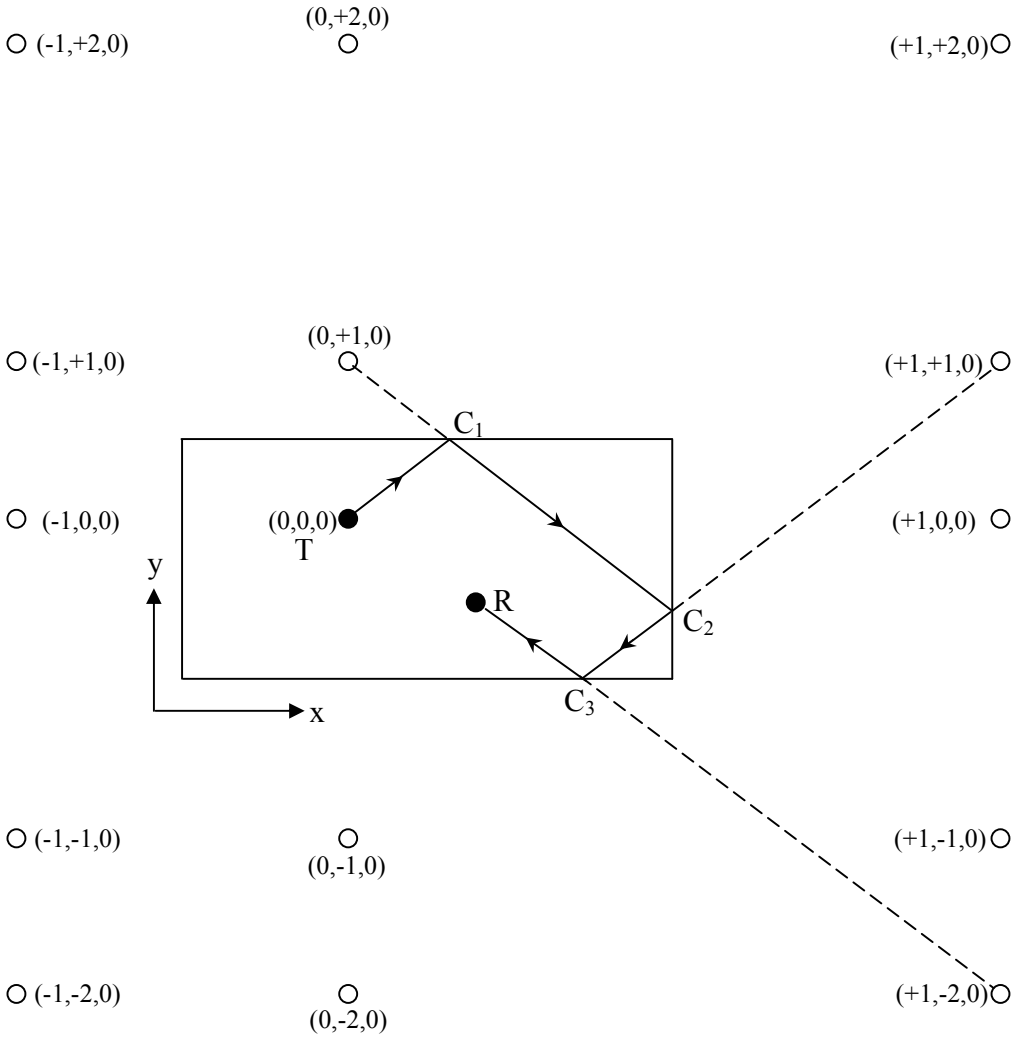

Fig. 3.1 [Eln03]

Image theory in a 3D rectangular structure.

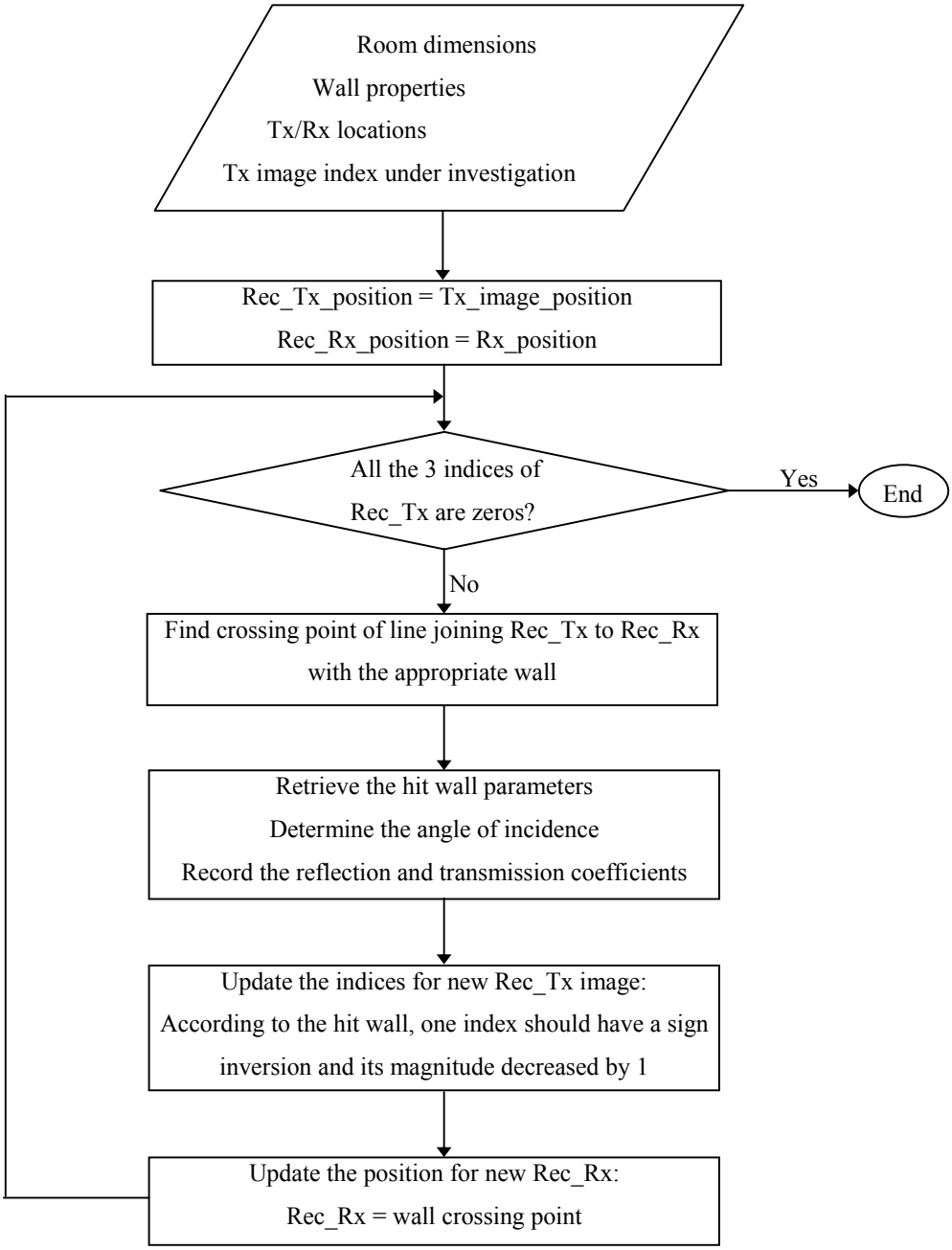

Fig. 3.2 [Eln03]

Algorithm flow chart for the recursive reflection tracing in a rectangular structure.

3.3 Comparison of IRT and Modal Analysis for MIMO-DOF Evaluation

The objective of this section is to validate the developed IRT algorithm for a rectangular structure by using the PID as a benchmark for the deterministic scenario simulated. We apply the IRT algorithm to evaluate the PID of size-specific (fixed aperture size at the transmit/receive ends) multi-polarization MIMO systems in a long corridor of lossy-walls. We make another PID evaluation, using modal analysis, for the same MIMO system in a comparable open waveguide of perfect electric conductor (PEC) walls.

The PEC canonical structure is subject to a straightforward modal analysis [Col90, Eom04], which is described in appendix B, where the exact field (multi-mode Green's function) is found in response to multi-pole point-source excitations. The PEC corridor should not be considered a LOS scenario, but rather a highly multipath-rich environment due to the lossless reflection encountered by each ray as discussed in sub-section 3.1.3. Certainly, a PEC rectangular enclosure (cavity) would have experienced ideal multipath richness [LM06] and is more geometrically comparable to the lossy-wall corridor; however, the former suffers from computational complexity due to resonance/evanescence situations as pointed out in appendix B. This is the reason of our choice of an open PEC waveguide for comparison since it is more computationally friendly in the modal analysis.

As shown in Fig. 3.1, we denote the axis along the corridor length, width and height by (L,W,H), respectively. The lossy-wall rectangular corridor dimensions are $100\times4\times3$ m along (L,W,H), respectively. The transmit and receive phase-centres are located at (50, 2, 2.8) and (75, 1.5, 1.7) along (L,W,H), respectively. The walls thickness is 15 cm with a dielectric constant of 4. The ceiling and floor thicknesses are 30 cm with a dielectric constant of 6.

Similarly, the PEC waveguide dimensions are 4×3 m along (W,H), respectively; the transmit and receive PCs are located at (2, 2.8) and (1.5, 1.7) along (W,H), respectively and are separated 25 m along the L-dimension.

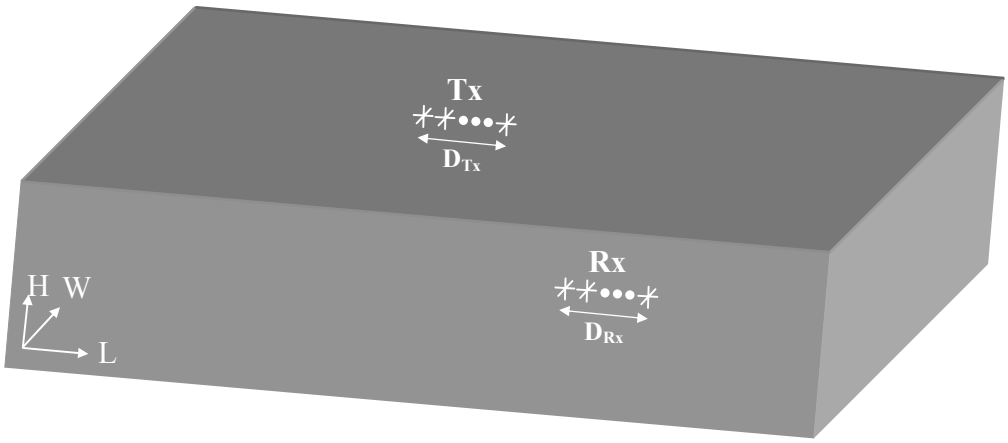

Fig. 3.3

Size-specific 1D MIMO system. The array is oriented along L-L. At each spatial point, there is a collocated tripole (3 physical ports).

The operating frequency is 2.4123 GHz, where such value is chosen to avoid numerical complexity in case any mode happens to be exactly operating at one of the cut-off frequencies. Under such operating conditions (frequency and corridor dimensions), we have multi-mode propagation through the PEC guide (precisely 2495 propagating modes), confirming the multipath richness of the environment. Moreover, we set the system to operate in far-field (transmit/receive separation large enough in comparison with λ) and thus, the evanescent modes can be safely discarded.

As shown in Fig. 3.3, the transmit and receive ends have fixed aperture sizes. We depict the 1D fixed aperture size of D_{Tx} and D_{Rx} at the transmit and receive ends, respectively. Within the array length, a number of tripoles (tri-polarized electric point radiators) is deployed equidistantly and the number of

the physical ports is the triple of the number of the tripoles. The motivation of choosing tripoles rather than a simple unipolarized dipole in the comparison is that we want to consider the full 3D multipath richness. Under the Maxwellian framework, the isotropic radiator does not exist [SSWB03, SBY+06] because of the endfire radiation characteristic even with an infinitesimal dipole. Therefore, employing tripoles neutralize the effect of the endfire null of a unipolarized pattern without deviating from the rigorous Maxwellian framework by assuming an isotropic radiator.

In modal analysis, the transmit polarized point source has its response as given in appendix B whereas at the receive point, it acts as an ideal field sampler according to its specific polarization. In IRT, the transmit and receive antennas, both in the transmit mode of operation, are modeled through the far-field normalized effective length (after omitting the common factors and assuming the same current excitation). Accordingly, for a point electric current source, polarized in the $\hat{\mathbf{a}}_\xi$ direction, the normalized effective length is given by the following decomposition over $\hat{\mathbf{a}}_\theta$ and $\hat{\mathbf{a}}_\varphi$

$$\mathbf{e} = -(\hat{\mathbf{a}}_\xi \cdot \hat{\mathbf{a}}_\theta)\hat{\mathbf{a}}_\theta - (\hat{\mathbf{a}}_\xi \cdot \hat{\mathbf{a}}_\varphi)\hat{\mathbf{a}}_\varphi . \tag{3.27}$$

We plot the PID results versus the number of rays for 3 orientations of the 1D transmit-receive arrays along L-L, W-W and H-H in Fig. 3.4-6, respectively. For each orientation, we use different array lengths within which a number of tripoles is packed equidistantly. The number of tripoles within each array is chosen to be the minimum after which the PID tends to saturate (more details about this space-constrained DOF are discussed in chapter 5). In the lossy-wall scenario, we repeat the simulations for various loss-tangent (LT) values of the walls ranging from "transparent" lossy-dielectric ($\mathrm{LT} \sim 10^{-2}$) to "reflective" lossy-conductor ($\mathrm{LT} \sim 10^{2}$). The PID in the IRT simulations is evaluated using different number of rays, ordered according to their contribution significance as previously discussed, and their number ranges from 500 to 10^4 rays.

In general, there is a common trend of saturation of the PID value as the number of the rays increases. For large LT, more rays are needed (several thousands) to reach some oscillatory saturation, whereas in the small LT cases, few hundreds rays are sufficient [ESC04a]. Also, as intuitively expected, the more reflective the walls become (larger LT), the higher the PID is achieved because of the more available significant rays. Moreover, we notice that for the reflective walls scenarios ($LT \sim 10^2$), the PID results of the IRT simulation are approaching those obtained through rigorous modal solution in the PEC open waveguide. The discrepancy between the latter results increases in the L-L orientation, where the dimensionality is already low because of the end-fire array configuration [ATKM03, LDBD03, ESC05]. The discrepancy between the results ($LT \sim 10^2$ and PEC) scenarios is attributed to the following reasons:

1. Although the 2 environments are geometrically similar, they are not identical: the wave-guide is open-ended, whereas the corridor is a rectangular enclosure (providing 2 more reflection planes for the rays, albeit of limited impact due to the large separation). Also, the wave-guide has PEC lossless walls while those in the corridor are lossy conductors resulting in a power loss at each reflection.
2. The IRT simulation is based on plane wave-front approximation, which was employed to tremendously reduce the computational time in comparison to the more exact spherical wave-front element-to-element ray tracing.
3. When the array is too close to the wall (e.g. the transmit in the H-H orientation), the far field assumption of the IRT is breached.
4. When the scenario is inherently rank-deficient (such as with the L-L orientation), the dimensionality is small per se and the channel matrix construction, based on IRT, is more sensitive to any applied approximation.
5. The diffraction mechanism is neglected in the implemented IRT. This means that the diffracted rays off the corridor corners are not considered.

In Fig. 3.7-8, we plot the results for 2D arrays at the transmit/receive ends, where the PID is larger in comparison with the 1D cases. The results of the PEC-waveguide and the reflective walls case are closer, in the exception of Fig. 3.8b where the PID is higher in the lossy reflective walls scenario. This latter result occurred because the 2D square array at the transmit, which is oriented along WH-WH, has its edge very close to the ceiling which makes some deviation from the far-field approximation assumption. The trend of PID saturation is similar to that of the 1D cases regarding the required number of rays.

3.4 Summary

In this chapter, we presented the electromagnetic narrowband modeling of the MIMO systems in deterministic environments including all sources of diversity (space, pattern and polarization). The modeling is based on the high-frequency approximation (ray-tracing) as well as the PWA. We applied this model through the IRT in rectangular structures. We made a MIMO-PID comparison between the IRT simulations and the results of a similar PEC open wave-guide structure using rigorous modal analysis with multi-polarized point sources. The results are generally comparable in the case of reflective lossy-walls (large LT), where some thousands of rays are needed to reach a saturated result. In the case of transparent walls (small LT), few hundreds of rays are sufficient to provide a stable result.

In the next chapter, we investigate the multi-polarization effect as the sole source of diversity in MIMO systems, based on the modeling of this chaper. This includes tripoles and hexapoles in PEC and lossy-wall environments. The near-field effect in free-space will also be discussed.

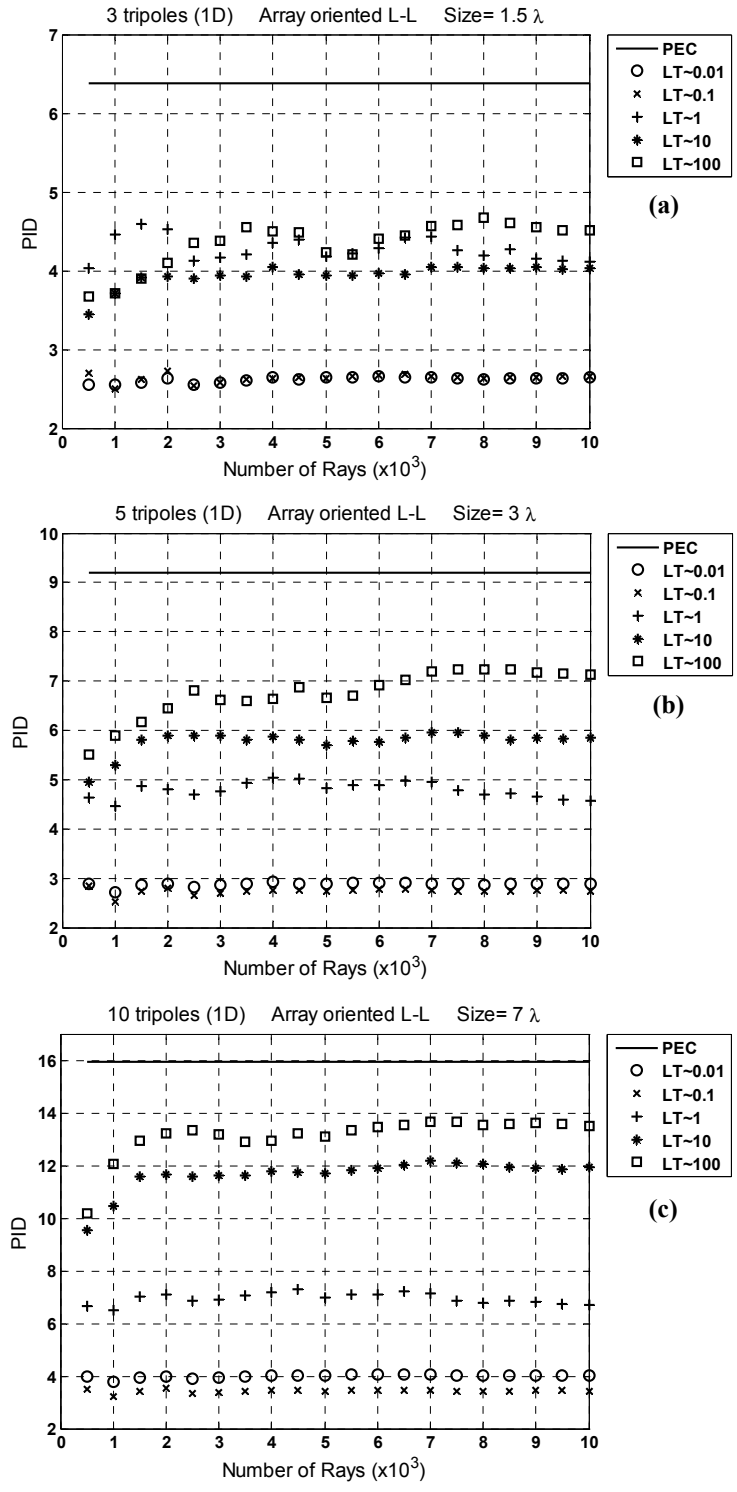

Fig. 3.4

IRT and modal solution comparison of multi-polarization size-specific 1D MIMO system along L-L. Array length (in terms of free-space wavelength) (a) 1.5 (b) 3 (c) 7. Number of tripoles (a) 3 (b) 5 (c) 10.

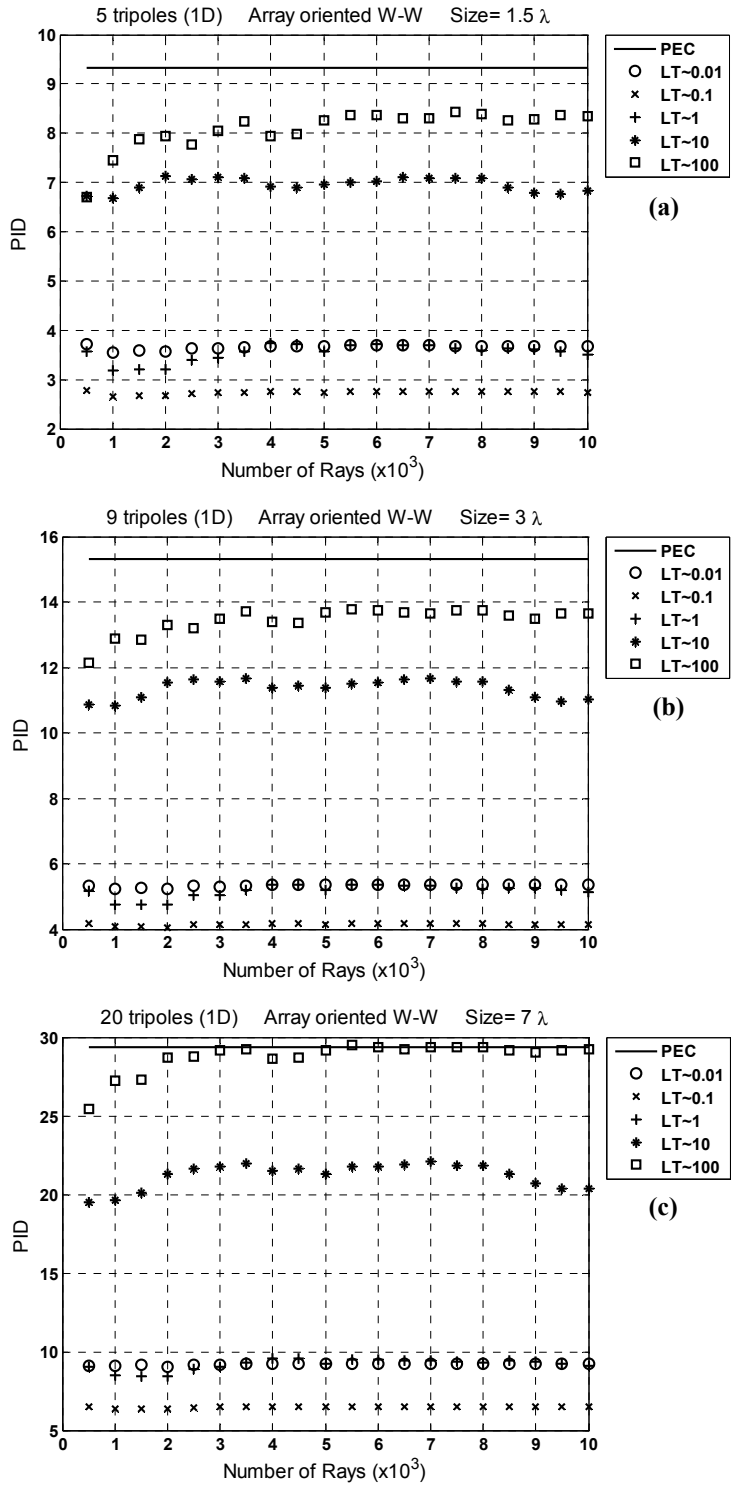

Fig. 3.5

IRT and modal solution comparison of multi-polarization size-specific 1D MIMO system along W-W. Array length (in terms of free-space wavelength) (a) 1.5 (b) 3 (c) 7. Number of tripoles (a) 5 (b) 9 (c) 20.

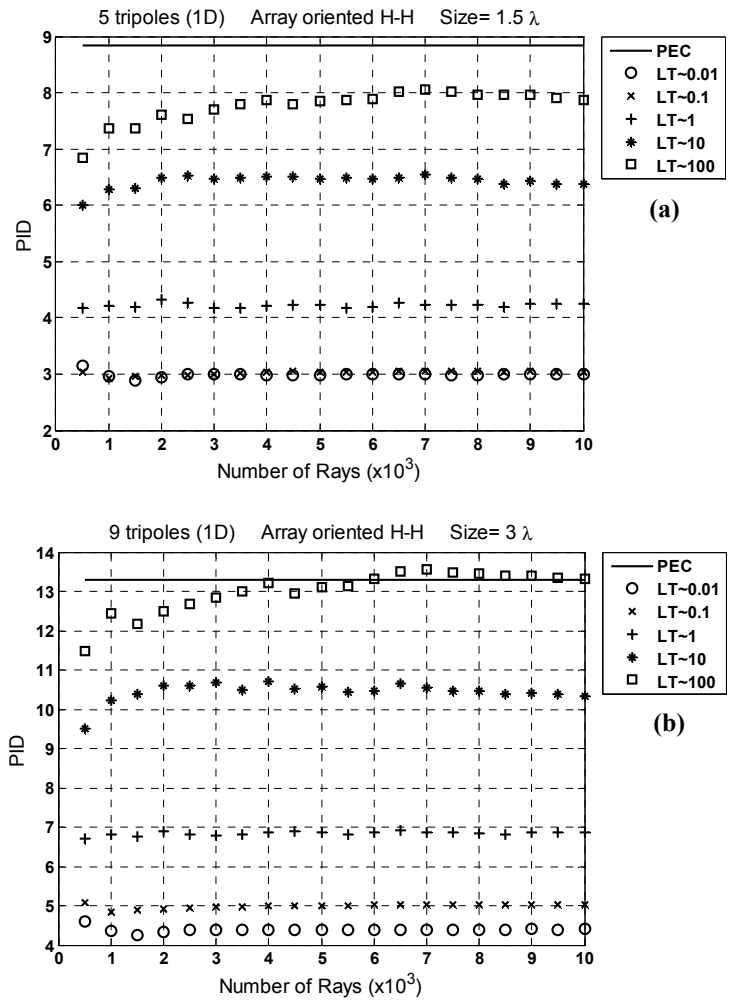

Fig. 3.6

IRT and modal solution comparison of multi-polarization size-specific 1D MIMO system along H-H. Array length (in terms of free-space wavelength) (a) 1.5 (b) 3. Number of tripoles (a) 5 (b) 9.

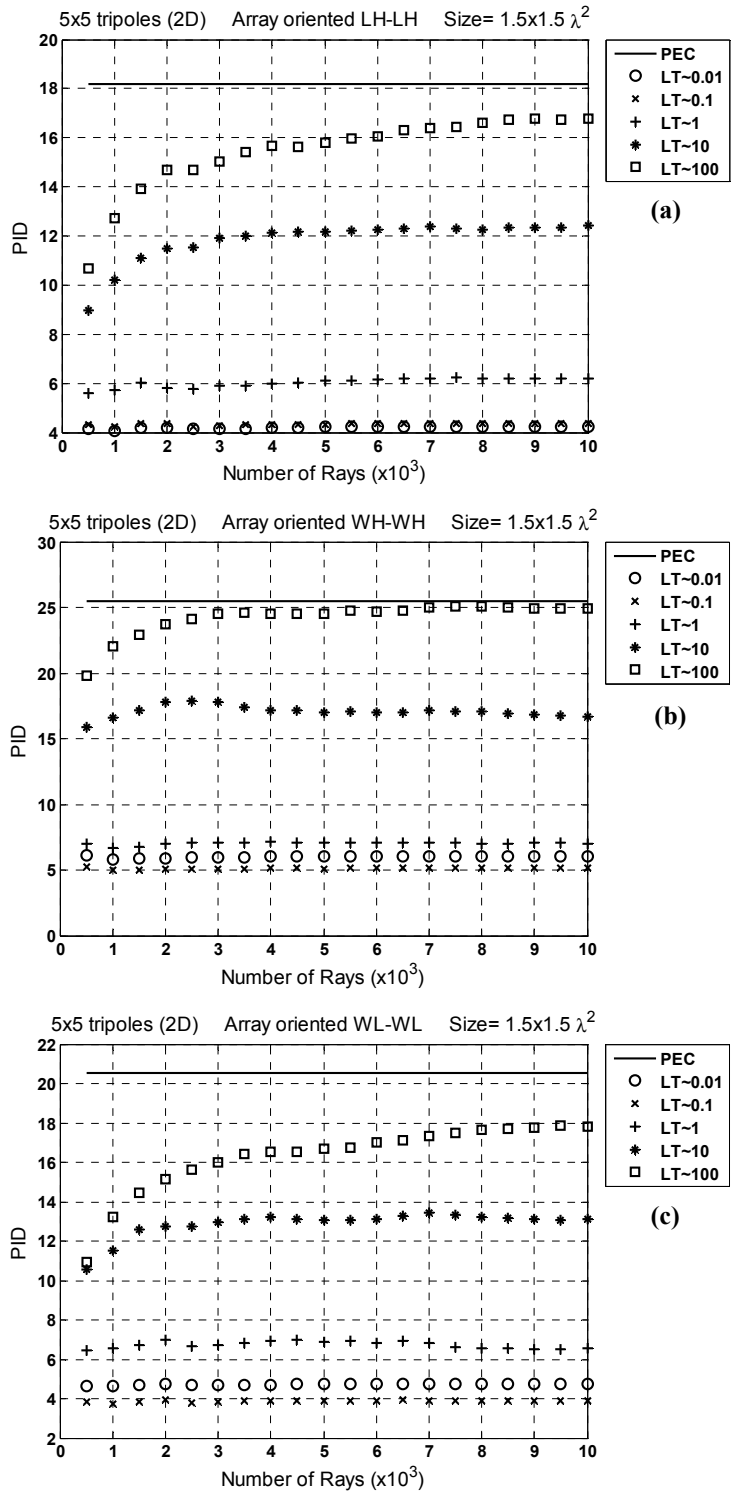

Fig. 3.7

IRT and modal solution comparison of multi-polarization size-specific 2D MIMO system of aperture size $1.5\times1.5\lambda^2$, 5×5 tripoles per aperture and oriented as (a) LH-LH (b) WH-WH (c) WL-WL.

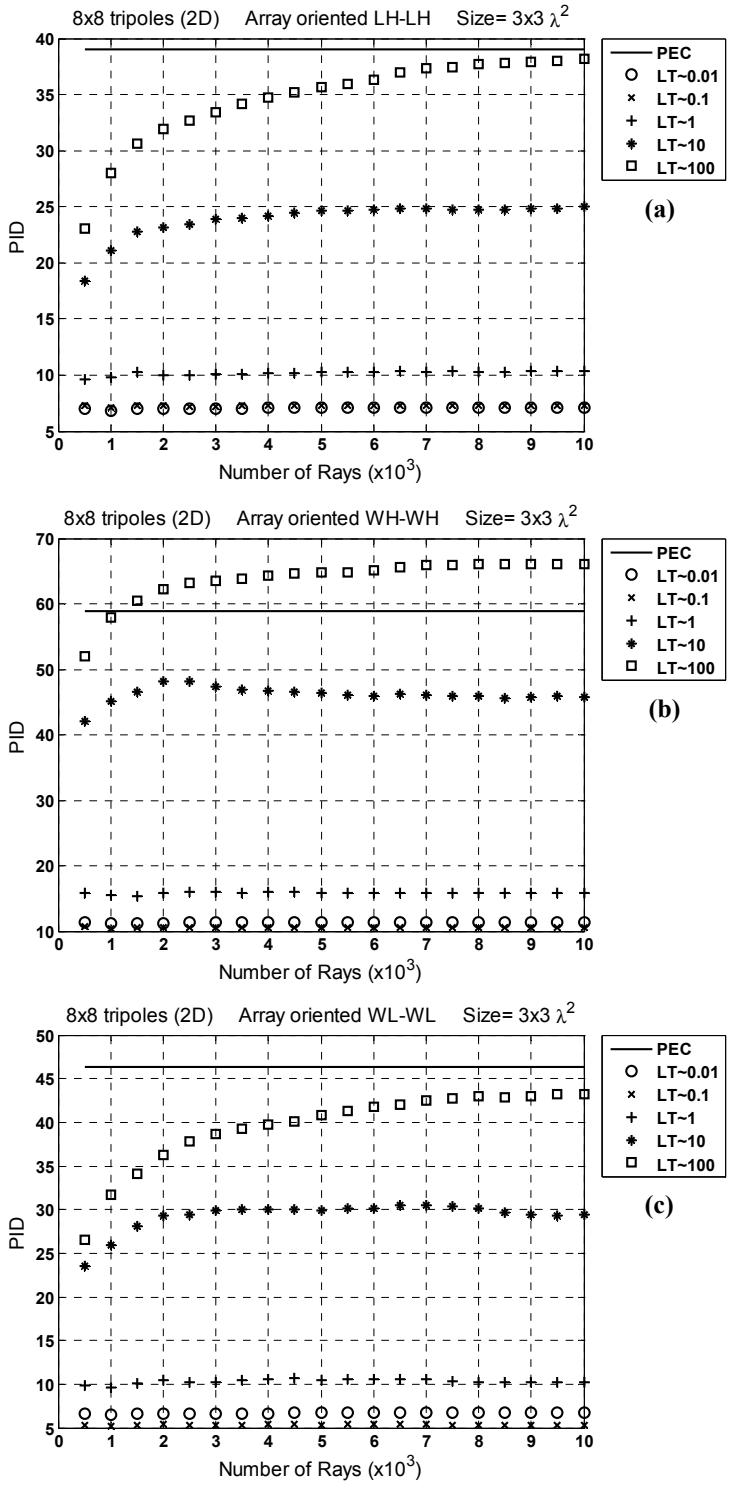

Fig. 3.8

IRT and modal solution comparison of multi-polarization size-specific 2D MIMO system of aperture size $3\times3\lambda^2$, 8×8 tripoles per aperture and oriented as (a) LH-LH (b) WH-WH (c) WL-WL.

Chapter 4
Multi-Polarization Dimensionality

As a first application of the developed PID metric, this chapter is devoted to measure the DOF gain (i.e. creation of new parallel sub-channels) through a collocated multi-polarization MIMO system. "Multi-polarization" designates transmit/receive collocated configurations, namely, tripoles (3 mutually-orthogonal collocated point sources forming 3 independent ports), hexapoles (2 coincident dual tripoles i.e. electric and magnetic as described in [AMC01, SJW04]), or further combined dual polarization cases.

In the next chapter, it will be shown that the DOF problem of a size-specific MIMO aperture is essentially a classical problem of spatial (1D, 2D or 3D) sampling under bandwidth constraints of the spatial frequency. On the contrary, the problem tackled in this chapter is eventually a single-point sampling (through infinitesimal electric/magnetic dipoles) of a vector-field which happens to experience 2 types of spatial orthogonality: *vectorial* and (scalar) *functional* [SJW04]. The former is the essence of the polarization diversity whereas one form of the latter is the pattern diversity in the *far-field* modeling.

Based on deterministic simulations, we will show that the vectorial and functional orthogonality are not necessarily independent due to the inevitable coupling between the electric and magnetic field components. Consequently, the claim of hexapole sixfold dimensionality gain [AMC01, SJW04] under the statistical channel assumption is not practically guaranteed.

We attempt to provide a clear answer to the following controversial question raised in the literature [PM00, AMC01, SJW04, PBT05]: can each of the electric and magnetic fields carry an independent piece of information between 2 radiating structures and thus doubling the one-field communication dimensions? The challenge in this question lies in the fact that the 2 fields are not simultaneously arbitrary since they are related by Maxwell's equations. In this chapter, we will show, through a universal model sustained by numerical results, that the key point of the answer is the 2 inter-winded orthogonality types, which are environment-specific.

The novelty claimed throughout this chapter is the *deterministic* modeling of the multi-polarization problem based on the *Maxwellian framework* [SSWB03, SBY+06], using the *well-defined dimensionality metric* developed in chapter 2 [ESC06b, ESC07a]. We begin by setting a generic framework for multi-polarization scenarios using a 6×6 polarization matrix based on Maxwell's equations. A canonical free-space (near and far field) scenario is then thoroughly investigated showing a particular transmit/receive separation at which full-rank dimensionality is achievable using tripoles. Subsequently, we show multi-polarization results in a PEC corridor scenario using rigorous modal analysis followed by a transparent lossy-wall (small LT) corridor scenario using the IRT algorithm presented in chapter 3. We conclude by showing a histogram of the multi-polarization dimensionality results of the simulated scenarios.

4.1 Universal Multi-Polarization Modeling

The objective of this chapter is to investigate the DOF gain by employing the polarization diversity in multi-antenna systems while deliberately excluding the space diversity. This is the reason of our choice of the infinitesimal (Hertzian) dipole as a perfect multi-polarization "field-probe", having a zero-length and detecting the vectorial nature of the electromagnetic fields. Nevertheless, we must admit that the polarization diversity is inseparable of the pattern diversity, which ultimately makes the multi-polarization zero-length MIMO system founded on the pattern/polarization diversity. In fact, this double-diversity is the base of the 2 aforementioned types of collocated spatial orthogonality (vectorial and functional) in multi-polarization MIMO systems.

The channel under investigation is described by a 6×6 polarization matrix $\mathbf{H}^{(hexa)}$ [SJW04]. For m or $n = \{1,2,3\}$, the element h_{mn} represents an *electrical* receive/transmit, where $(1,2,3)$ denote indices for the 3 mutually orthogonal coordinates. Similarly, for m or $n = \{4,5,6\}$, h_{mn} represents a *magnetic* receive/transmit, where $(4,5,6)$ denote indices for the same 3 mutually orthogonal coordinates, respectively. Thus, the electric and magnetic tripoles, which form the hexapole, are coincident at the transmit/receive points. We assume narrowband operation of the system. Moreover, the following source/detector normalization assumptions are made:

1. The electric $(I_E l)$ and magnetic $(I_M l)$ dipole moments are normalized such that $(I_M l) = \eta_0 (I_E l)$, where $\eta_0 = 120\pi$ ohm is the free-space impedance. Therefore, after normalizing the electric and magnetic dipole moments value to unity, any transmit magnetic field component is multiplied by η_0 in the following analysis.

2. The received signal, either by an electric or magnetic infinitesimal dipole, is detected as a proportional voltage. Therefore, any receive magnetic field component is multiplied by η_0 in the following analysis.

From the duality between the electric and magnetic fields [Har61], the hexapole channel matrix $\mathbf{H}^{(hexa)}$ is expressed as

$$\mathbf{H}^{(hexa)} = \begin{pmatrix} \mathbf{C} & -\mathbf{D} \\ \mathbf{D} & \mathbf{C} \end{pmatrix}, \tag{4.1}$$

where, for $n = \{1,2,3\}$, the column vectors $[c_{\bullet n}]$ and $[d_{\bullet n}]$ of the 3×3 sub-matrices $\mathbf{C}$ and $\mathbf{D}$ represent the receive electric and magnetic fields response, respectively, to the n^{th} polarized transmit *electrical* excitation. Furthermore, at the receive point, the source-free Maxwell's curl equations must be satisfied

$$\nabla \times \overline{E} = -j\,\omega\mu_0 \overline{H} \tag{4.2a}$$

$$\nabla \times \overline{H} = j\,\omega\varepsilon_0 \overline{E}\,. \tag{4.2b}$$

Therefore, from the aforementioned normalization assumptions and (4.2a), the sub-matrices $\mathbf{C}$ and $\mathbf{D}$ are related by

$$\mathbf{D} = \eta_0 \frac{\overline{\nabla}\times\mathbf{C}}{-j\,\omega\mu_0} = \frac{j}{k_0}\overline{\nabla}\times\mathbf{C}\,, \tag{4.3}$$

where $\overline{\nabla}\times\mathbf{C}$ is a dyadic curl (operating on the column vectors of $\mathbf{C}$) and k_0 is the free space wave number. Accordingly, $\mathbf{H}^{(hexa)}$ is expressed as

$$\mathbf{H}^{(hexa)} = \begin{pmatrix} \mathbf{C} & -\frac{j}{k_0}\overline{\nabla}\times\mathbf{C} \\ \frac{j}{k_0}\overline{\nabla}\times\mathbf{C} & \mathbf{C} \end{pmatrix}. \tag{4.4}$$

Equation (4.4) is *universal* at any *source-free* point in any environment (i.e. under any boundary conditions) as long as we are operating the system in narrowband and the environment electrical/magnetic properties are deterministic at any one time. At any point in space where there is an impressed source or medium inhomogeneity (e.g. at the boundaries), (4.4) is not true.

Now, we return back to the question regarding the usage of $\overline{E}$ and $\overline{H}$ as independent information carriers. From (4.4), given the fact that the elements of $\mathbf{H}^{(hexa)}$ are not all independent, can we really achieve 6 DOF? Stated in another way, given that $\overline{E}$ and $\overline{H}$ are not simultaneously arbitrary, according to Maxwell's equations, is it possible that we achieve more than 3 DOF by using a hexapole system? The answer was positive in [AMC01, SJW04] and negative in [PM00, PBT05]. The deterministic results of this chapter provide evidence that by employing a hexapole system, we *can* have more than 3 DOF *if* the environment permits, however, the maximum 6 DOF cannot be attained. So the core of the answer is how to exploit the 2 naturally-available orthogonality types in the *deterministic environment*.

The matrix rank becomes deficient when there exists a *linear algebraic* dependence between the matrix rows or columns. In (4.4), there is a linear dependence, however, it is *differential* rather than algebraic and has therefore no clear impact on the matrix rank. The environment properties, manifested through the boundary conditions, set the explicit *algebraic* dependence between $\mathbf{C}$ and $\mathbf{D}$ in (4.1). We will see in the upcoming case studies that whenever this differential dependence approximates a linear algebraic one (single plane-wave or spherical ray), only then, the rank becomes deficient.

The vectorial orthogonality is exhibited through the 3 components of one vector field (either electric $\overline{E}$ or magnetic $\overline{H}$ but not both) along the 3 mutually orthogonal coordinates. Hence, the vectorial orthogonality is also known as the polarization diversity. If the dual fields ($\overline{E}$ and $\overline{H}$) were independent (uncoupled), a pair of infinitesimal dual tripoles (electric and magnetic) would be sufficient to allow up to 6 DOF through dual vectorial orthogonality. However, the dual fields are indeed coupled; otherwise, the *electromagnetic* propagation would not exist. Therefore, in order to employ the DOF of the dual field, it is mandatory to have another sort of diversity, which is accomplished

through the so-called Field Expansion Diversity (FED), also known as the functional orthogonality or, in the far-field analysis, pattern diversity. The terms functional orthogonality and FED will be used interchangeably.

The FED is best understood when the received field is expressed as an integration (or summation in discrete analysis) of some field expansion components such as in the following situations:

- The spherical propagating multipath rays in the case of high-frequency approximation (IRT). We emphasize that in this case, each ray should be considered inseparably of the transmit/receive pattern-weighting [SJW04]. This is the core of the EM modeling of chapter 3.
- In general, the plane-wave expansion components of the received field [Cle66]. In appendix C, we present a summary of the plane-wave expansion.
- The modes in a PEC waveguide, which can straightforwardly be further decomposed into a summation of plane waves.

As explained in chapter 3, the l^{th} expansion matrix-component $\mathbf{H}_l^{(hexa)}$ is individually rank-deficient (of rank 2 as in the case of plane-wave or ray multipath modeling). Nevertheless, the integration (summation) of all the expansion components *can* produce a higher rank matrix $\mathbf{H}^{(hexa)} = \sum_l \mathbf{H}_l^{(hexa)}$ of better DOF [AMC01, SJW04]. Consequently, a rank-deficient integrand with respect to the continuous angular domain [PBT05] (or a matrix-component in the discrete angular case) in the expansion is not automatically a bottle-neck for the DOF of the multi-polarization MIMO system as was argued in [PBT05]. In case of ray modeling, such FED is traditionally known as the antenna far-field *pattern diversity* [SJW04] since the weighted-integration (summation) of the multipath rays is done through the antenna patterns over the visible angular domain.

As shown in appendix C, for each plane-wave component, there is a linear algebraic dependence between the transverse electric and magnetic field components such that

$$\overline{\widetilde{E}}(\hat{\mathbf{k}})\cdot\hat{\mathbf{k}}=0 \tag{4.5}$$

$$\overline{\widetilde{H}}(\hat{\mathbf{k}})=\frac{\hat{\mathbf{k}}\times\overline{\widetilde{E}}(\hat{\mathbf{k}})}{\eta_0}, \tag{4.6}$$

where $\hat{\mathbf{k}}$ is the complex unit vector in the k-domain (C.6a), $\overline{\widetilde{E}}(\hat{\mathbf{k}})$ and $\overline{\widetilde{H}}(\hat{\mathbf{k}})$ are the electric and magnetic field transforms in the k-domain as given by (C.3) and (C.13), respectively. Hence, for each plane wave component, only one field (either $\overline{\widetilde{E}}(\hat{\mathbf{k}})$ or $\overline{\widetilde{H}}(\hat{\mathbf{k}})$ but not both) can carry independent information. By taking $\overline{\widetilde{E}}(\hat{\mathbf{k}})$ as the independent information carrier for each plane wave, we have the following double-impact when all the plane-wave components impinge on a hexapole receive from *different directions*:

- Even though each plane wave individually allows 2 DOF based on partial vectorial orthogonality (the 2 transverse components of $\overline{\widetilde{E}}(\hat{\mathbf{k}})$ in (4.5)), the plane-wave integration (C.6b) creates a third vectorial electric DOF because the resultant electric field has 3 components [AMC01].
- Each field component (say $\widetilde{E}_z(\hat{\mathbf{k}})$) of an impinging plane wave has the potential to interact with 3 receive elements (electric z-polarized and transverse magnetic x- and y-polarized elements). However, these 3 receive elements interpret differently the same $\widetilde{E}_z(\hat{\mathbf{k}})$ according to the plane wave DOA. Ultimately, when all the plane waves are angularly weighted (C.6b), the functional orthogonality is created and gives room to more DOF [SJW04].

Therefore, in the hexapole system, we are exploiting both the vectorial nature of *one field* along with the angular sensitivity of the *dual-field detector* (rather than the dual-field itself, which is not independent) to convey

independent pieces of information. Accordingly, the aforementioned question of possible 6 DOF becomes whether the same analysis mechanism (plane-wave expansion) can provide 2 *independent* orthogonality effects. The numerical results of this chapter show that there is an inevitable coupling between these 2 effects.

4.2 A Canonical Free-Space Multi-Polarization Scenario

In this section, we investigate the PID distance-dependence (near and far field) of free-space multi-polarization MIMO system. We consider several transmit/receive multi-polarization cases, namely, tripoles, hexapoles and further combined dual polarization cases. Notwithstanding the unusual MIMO scenario (free-space, no multipath) being investigated, the rigorously derived results shed light on possible near field applications such as short-distance/low-frequency indoor MIMO systems based on collocated multi-polarization. Moreover, the free-space near-field can be plane-wave expanded [Cle66] yielding significant spatial bandwidth. Thus, the near-field scenario has a similarity with a super-rich multipath environment.

For a z-polarized infinitesimal electrical dipole in free space, the exact expressions of the field components in spherical coordinates are given by [Str41, Bal97]

$$\begin{aligned} E_r &= (I_E l)\eta_0 \frac{\cos\theta}{2\pi r^2}\left(1+\frac{1}{jk_0 r}\right)e^{-jk_0 r} \\ E_\theta &= j(I_E l)\eta_0 \frac{k_0 \sin\theta}{4\pi r}\left(1+\frac{1}{jk_0 r}-\frac{1}{(k_0 r)^2}\right)e^{-jk_0 r} \\ H_\varphi &= j(I_E l)\frac{k_0 \sin\theta}{4\pi r}\left(1+\frac{1}{jk_0 r}\right)e^{-jk_0 r} \\ E_\varphi &= H_r = H_\theta = 0 \end{aligned} \quad . \tag{4.7}$$

By duality, for a z-polarized infinitesimal magnetic dipole in free space, the field components are given by [Str41, Bal97]

$$
\begin{aligned}
H_r &= \frac{(I_M l)}{\eta_0}\frac{\cos\theta}{2\pi r^2}\left(1+\frac{1}{jk_0 r}\right)e^{-jk_0 r} \\
H_\theta &= j\,\frac{(I_M l)}{\eta_0}\frac{k_0 \sin\theta}{4\pi r}\left(1+\frac{1}{jk_0 r}-\frac{1}{(k_0 r)^2}\right)e^{-jk_0 r} \\
E_\varphi &= -j\,(I_M l)\frac{k_0 \sin\theta}{4\pi r}\left(1+\frac{1}{jk_0 r}\right)e^{-jk_0 r} \\
E_r &= E_\theta = H_\varphi = 0
\end{aligned}
\qquad . \tag{4.8}
$$

We begin by the hexapole $(6,6)$ system and we follow the normalization assumptions of section 4.1. We also assume an orientation as depicted in Fig. 4.1 for the transmit/receive hexapoles (2 broadside/1 endfire setup) and the hexapoles are separated by a distance r . Any arbitrary transmit/receive rotation is modeled by a unitary matrix with has no effect on the singular values of the channel matrix.

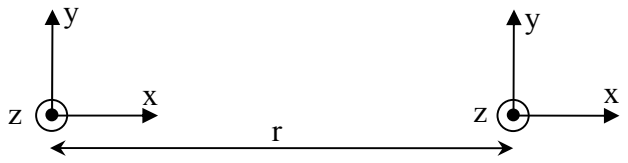

Fig. 4.1 hexapole setup
2 collocated dual tripoles each consisting of 2 broadside and 1 endfire elements.

We choose the Cartesian coordinates to construct $\mathbf{H}^{(hexa)}$ such that the indices $(1,2,3)$ of the elements h_{mn} denote the (x,y,z) coordinates for *electrical* receive/transmit whereas the indices $(4,5,6)$ of the elements h_{mn} denote the (x,y,z) coordinates for *magnetic* receive/transmit, respectively. According to Fig. 4.1, using (4.7-8) along with coordinate transformation and the aforementioned normalization assumptions, $\mathbf{H}^{(hexa)}$ is constructed yielding

$$\mathbf{H}^{(hexa)} = \begin{bmatrix} a_1 & 0 & 0 & 0 & 0 & 0 \\ 0 & a_2 & 0 & 0 & 0 & a_3 \\ 0 & 0 & a_2 & 0 & -a_3 & 0 \\ 0 & 0 & 0 & a_1 & 0 & 0 \\ 0 & 0 & -a_3 & 0 & a_2 & 0 \\ 0 & a_3 & 0 & 0 & 0 & a_2 \end{bmatrix}, \tag{4.9a}$$

where, after multiplying the field components by $4\pi r^2$ and omitting the common factors,

$$\begin{aligned} a_1 &= 2(1+\xi^{-1}) \\ a_2 &= \xi + 1 + \xi^{-1} \\ a_3 &= \xi + 1 \\ \xi &= jk_0 r \end{aligned} . \tag{4.9b}$$

For an arbitrary hexapole orientation in free-space, the generic channel matrix $\tilde{\mathbf{H}}^{(hexa)}$ is given by

$$\tilde{\mathbf{H}}^{(hexa)} = \begin{bmatrix} \mathbf{R} & \mathbf{0} \\ \mathbf{0} & \mathbf{R} \end{bmatrix} \mathbf{H}^{(hexa)} \begin{bmatrix} \mathbf{T} & \mathbf{0} \\ \mathbf{0} & \mathbf{T} \end{bmatrix}, \tag{4.10}$$

where $\underset{3\times3}{\mathbf{R}}$ and $\underset{3\times3}{\mathbf{T}}$ are coordinate rotation transformers at the receive/transmit ends, respectively, and are thus unitary. Consequently, the matrices $\tilde{\mathbf{H}}^{(hexa)}$ and $\mathbf{H}^{(hexa)}$ have the same singular values $\sigma\{\mathbf{H}^{(hexa)}\}$, which are obtained from (4.9) yielding

$$\sigma\{\mathbf{H}^{(hexa)}\} = \left\{|a_1|, |a_1|, |a_2 + a_3|, |a_2 + a_3|, |a_2 - a_3|, |a_2 - a_3|\right\}, \tag{4.11}$$

where each singular value has a multiplicity of 2 [SJW04].

We now turn our attention to the tripole channel described by the 3×3 matrix $\mathbf{H}^{(tri)}$. The tripole matrix $\mathbf{H}^{(tri)}$ can be extracted from $\mathbf{H}^{(hexa)}$ by using either 3 same-field polarizations ($\mathbf{H}^{(tri)} = [h_{mn}],\ \ m,n = \{1,2,3\} or \{4,5,6\}$); or 2 same-field broadside polarizations in addition to 1 dual-field endfire polarization ($\mathbf{H}^{(tri)} = [h_{mn}],\ \ m,n = \{2,3,4\} or \{5,6,1\}$). The latter case is

interesting because it can be implemented using 2 orthogonal electrical dipoles and 1 co-planar loop [KGK+05]. According to the setup of Fig. 4.1, and (4.9),

$$\mathbf{H}^{(tri)} = \mathrm{diag}(a_1, a_2, a_2)\,, \tag{4.12}$$

and therefore,

$$\sigma\{\mathbf{H}^{(tri)}\} = \{|\,a_1\,|, |\,a_2\,|, |\,a_2\,|\}\,. \tag{4.13}$$

The tripole channel is also orientation-independent.

Based on the global hexapole matrix in (4.9), one can examine further orientation-dependent multi-polarization cases. The 4×4 matrices $\mathbf{H}^{(3e)}$ and $\mathbf{H}^{(3b)}$ denote tetrapole channels consisting of (1 tripole, 1 dual endfire) and (1 tripole, 1 dual broadside) polarizations, respectively. The matrices are given by

$$\mathbf{H}^{(3e)} = \mathrm{diag}(a_1, a_2, a_2, a_1) \tag{4.14}$$

$$\mathbf{H}^{(3b)} = \begin{bmatrix} a_1 & 0 & 0 & 0 \\ 0 & a_2 & 0 & 0 \\ 0 & 0 & a_2 & -a_3 \\ 0 & 0 & -a_3 & a_2 \end{bmatrix}. \tag{4.15}$$

Similarly, the 5×5 matrices $\mathbf{H}^{(3eb)}$ and $\mathbf{H}^{(3bb)}$ denote pentapole channels consisting of (1 tripole, 1 dual endfire, 1 dual broadside) and (1 tripole, 2 dual broadside) polarizations, respectively. The matrices are given by

$$\mathbf{H}^{(3eb)} = \begin{bmatrix} a_1 & 0 & 0 & 0 & 0 \\ 0 & a_2 & 0 & 0 & 0 \\ 0 & 0 & a_2 & 0 & -a_3 \\ 0 & 0 & 0 & a_1 & 0 \\ 0 & 0 & -a_3 & 0 & a_2 \end{bmatrix} \tag{4.16}$$

$$\mathbf{H}^{(3bb)} = \begin{bmatrix} a_1 & 0 & 0 & 0 & 0 \\ 0 & a_2 & 0 & 0 & a_3 \\ 0 & 0 & a_2 & -a_3 & 0 \\ 0 & 0 & -a_3 & a_2 & 0 \\ 0 & a_3 & 0 & 0 & a_2 \end{bmatrix}. \tag{4.17}$$

Table 4.1 includes the closed-form singular values as well as the near-field ($a_1/a_2 \to 2$ and $a_3/a_2 \to 0$) and far-field ($a_1/a_2 \to 0$ and $a_3/a_2 \to 1$) PID values. Fig. 4.2 depicts the distance-dependence of the PID for the multi-polarization scenarios. The PID of case 1 and 2 in Table 4.1 reaches its maximum, rank($\mathbf{H}$), at one specific separation when $|a_1| = |a_2|$, which occurs at

$$\frac{r}{\lambda} = \frac{1}{2\pi}\sqrt{\frac{5+\sqrt{37}}{2}} \approx 0.3747, \tag{4.18}$$

where λ is the free space wavelength. For all the other cases, the inevitable coupling between the electric and magnetic field prevents the PID from reaching rank($\mathbf{H}$) and the maximum PID occurs in the near-field region ($k_0 r \ll 1$).

Table 4.1. Summary of Multi-Polarization Results

	Pol. Case	Singular Values	Near-Field PID $k_0 r \ll 1$	Far-Field PID $k_0 r \gg 1$
1	Tripole	$\sigma\{\mathbf{H}^{(tri)}\} = \{\lvert a_1\rvert, \lvert a_2\rvert, \lvert a_2\rvert\}$	8/3 ≈ 2.67	2
2	Tripole 1 endfire	$\sigma\{\mathbf{H}^{(3e)}\} = \{\lvert a_1\rvert, \lvert a_1\rvert, \lvert a_2\rvert, \lvert a_2\rvert\}$	3.6	2
3	Tripole 1 broadside	$\sigma\{\mathbf{H}^{(3b)}\} = \{\lvert a_1\rvert, \lvert a_2\rvert, \lvert a_2+a_3\rvert, \lvert a_2-a_3\rvert\}$	25/7 ≈ 3.57	1.8
4	Tripole 1 endfire 1 broadside	$\sigma\{\mathbf{H}^{(3eb)}\} = \{\lvert a_1\rvert, \lvert a_1\rvert, \lvert a_2\rvert, \lvert a_2+a_3\rvert, \lvert a_2-a_3\rvert\}$	49/11 ≈ 4.45	1.8
5	Tripole 2 broadside	$\sigma\{\mathbf{H}^{(3bb)}\} = \{\lvert a_1\rvert, \lvert a_2+a_3\rvert, \lvert a_2+a_3\rvert, \lvert a_2-a_3\rvert, \lvert a_2-a_3\rvert\}$	4.5	2
6	Hexapole	$\sigma\{\mathbf{H}^{(hexa)}\} = \{\lvert a_1\rvert, \lvert a_1\rvert, \lvert a_2+a_3\rvert, \lvert a_2+a_3\rvert, \lvert a_2-a_3\rvert, \lvert a_2-a_3\rvert\}$	16/3 ≈ 5.33	2

In the far-field region, case 3 and 4 have PID of 1.8, which is less than the expected 2 DOF (far-field polarization diversity) in the other cases. In fact, all the multi-polarization cases approach the dual channel mode in far field (i.e. only 2 non-zero singular values) as pointed out previously. However, for case 3

and 4, the 2 channels have non-equal contributions $\{2|a_2|,|a_2|\}$ whereas the other cases have equal dual-channel contributions $\{|a_2|,|a_2|\}$ or $\{2|a_2|,2|a_2|\}$. Therefore, from a dimensionality perspective, case 3 and 4 dimensionality performance is less than 2, although the power gain of one channel is 6 dB better than the other.

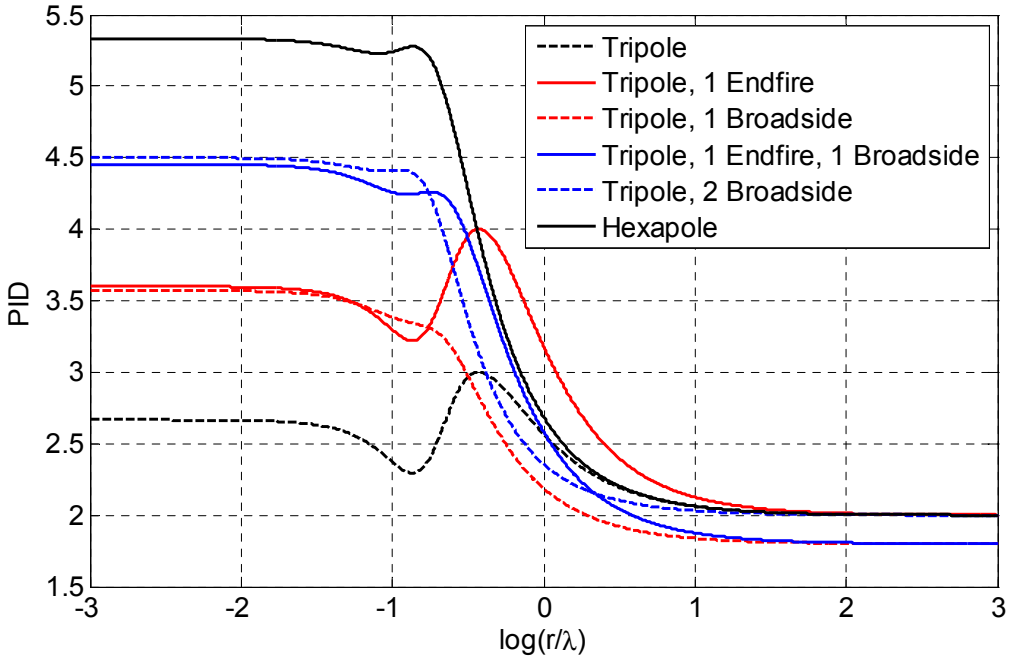

Fig. 4.2 PID vs r/λ (log-scale) for free-space multi-polarization scenarios.

In order to appreciate the merit of the canonical case investigated herein, we use the plane-wave expansion of the spherical wave [Cle66]. We assume a propagation hemisphere cross-section at $z=0$ (the chosen decay direction of the evanescent components is along the positive z-axis). Comparing the field vector potential analysis to the plane-wave expansion of the field of an electrical point source, we get [Cle66]

$$\frac{e^{-jk_0 r}}{r} = \frac{1}{j2\pi}\int_{-\infty}^{\infty}\int_{-\infty}^{\infty}\frac{e^{-jk_0\hat{\mathbf{k}}\cdot\mathbf{r}}}{k_z}dk_x dk_y\,, \tag{4.19}$$

where $\mathbf{r} = (x, y, z)$ is the position vector of the observation point with respect to the point source and $\hat{\mathbf{k}} = \frac{1}{k_0}(k_x, k_y, k_z)$ is in general a *complex* unit vector ($\hat{\mathbf{k}} \cdot \hat{\mathbf{k}} = 1$). According to our choice of the hemisphere cross-section at $z = 0$, k_x and k_y are always real. Accordingly, k_z is either real or pure imaginary as follows:

- For $k_x^2 + k_y^2 < k_0^2$, $k_z = +\sqrt{k_0^2 - k_x^2 - k_y^2}$ (positive real) and $\hat{\mathbf{k}}$ is the propagation direction of the traveling plane wave component.
- For $k_x^2 + k_y^2 > k_0^2$, $k_z = -j\sqrt{k_x^2 + k_y^2 - k_0^2}$ (negative pure imaginary) and the evanescent plane wave component is decaying in the positive z-direction at a rate of $e^{-|k_z|z}$.

In the far-field analysis, the spherical wave approaches a single traveling plane-wave (within a vicinity of some transmit/receive separation r to disregard the $1/r$ decay of the field). Therefore, the far-field scenario lacks any FED orthogonality since there is only one "plane-wave" component. Moreover, the absence of any field radial component reduces the vectorial orthogonality to 2. Consequently, we get the well-known horizontal and vertical polarization diversity for the hexapole system in the far-field region. From a matrix-modeling perspective, the far-field scenario approaches one matrix-component of rank 2, given the fact that there is a *linear algebraic* dependence between the transverse component of $\overline{E}$ and $\overline{H}$.

On the other hand, the near-field analysis of this canonical free-space scenario is more enlightening. Because of the closed-form vector potential in the left-hand side of (4.19), we were able to exactly derive the closed-form field solution (4.7-8) through Maxwell's equations, and the solution includes *all* the evanescent waves components, which is not computationally available in the other bounded electromagnetic problems. In the extended angular domain (both

visible and evanescent spectral domain $k_x, k_y \in (-\infty, \infty)$), the spectrum of (4.7-8) exhibits a wide spatial bandwidth (traveling and evanescent). In other words, the near-field analysis of a free-space scenario resembles a *super-rich* multipath environment (including traveling and evanescent waves). Although each plane-wave (traveling or evanescent) has individually 2 DOF, the integration of all plane-wave components yields a higher DOF, which is against the argument of [PBT05] concerning the strict upper limit of 2 DOF for the multi-polarization systems. Both the FED orthogonality and the existence of a radial field component (full vectorial orthogonality) results in a higher DOF. However, the coupling between the electric and magnetic fields does not allow the PID to reach the full-rank value of 6, which means that the vectorial and FED orthogonality are not strictly independent.

The multi-polarization DOF results in this example shed some light on the expected DOF in a realistic multipath scenario. If the near-field hexapoles (equivalent to a super-rich scattering) rigorously shows that more than 2 DOF are achievable whereas the 6 DOF (full-rank claimed in [AMC01, SJW04]) are not possible, we can expect a similar behavior in other multipath-rich *bounded* environments. The next section presents a case study yielding consistent results with this expectation.

4.3 Multi-Polarization in a PEC Corridor Scenario: Modal Analysis

We move now to investigate the multi-polarization DOF gain in a canonical indoor scenario. The environment is a rectangular open-ended corridor (waveguide) whose walls are perfect electric conductor (PEC). As mentioned in chapter 3, such canonical structure is a highly multipath-rich environment and we refer to appendix B for the modal solution of this multi-polarization excitation. Again, the corridor width and height are 4 m and 3 m, respectively.

The operating frequency is 2.4123 GHz, so chosen to avoid numerical complexity in the modal solution. Under these operating conditions (frequency and corridor dimensions), we have multi-mode propagation through the guide (precisely 2495 propagating modes).

The simulations are performed to show the multi-polarization DOF in the PEC corridor at 3 different scenarios. As shown in Fig. 4.3, we denote the axis along the corridor length, width and height by (L,W,H), respectively. The multi-polarized transmit is located at (2, 2.8) along (W,H), respectively. The multi-polarized receive is moving over a grid of equidistant 100×100 points on the whole cross-section of the corridor. The simulation is repeated over 3 grids situated at 25, 30 and 40 m from the transmit point along the L-axis. Such distances are sufficient to guarantee the suppression of all the evanescent modes.

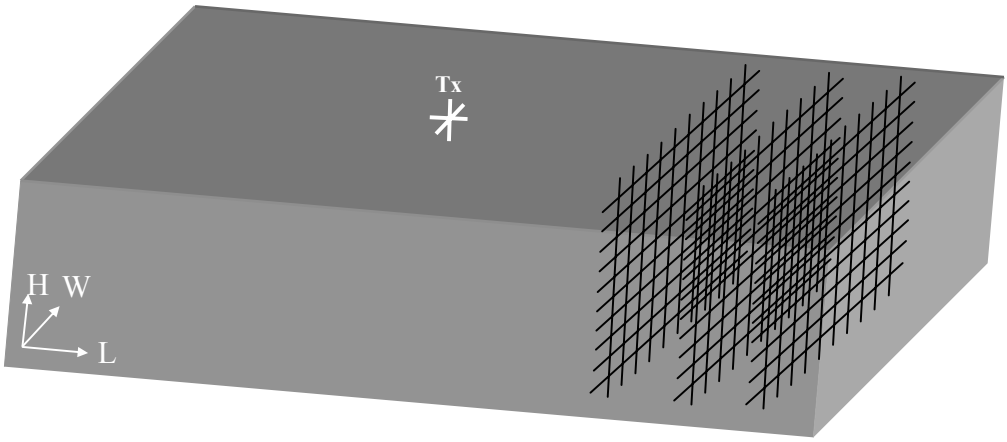

Fig. 4.3 Multi-polarization scenarios in a corridor.

Fig. 4.4a-c and 4.5a-c show the PID over the grid locations using tripoles and hexapoles, where the average PID is 2.35 and 4.3, respectively. These average values were obtained as well when the transmit and grid points were re-located to other positions. We can notice the rapid fluctuation of the PID over a very short distance. However, the standard deviation of the Frobenius norm (in

dB) of the channel matrix over the 10^4 receive points of each cross-section grid is less than 2 dB and 3 dB for the hexapole and tripole system, respectively, which indicates that we are in an essentially power-similar scenarios and the PID results are thus meaningful.

We can make several interesting observations from Fig. 4.4-5. In the hexapole case, 3 DOF or more are almost guaranteed. However, as expected earlier in this chapter from the near-field free-space scenario, the full-rank 6 DOF have never been achieved, even in this rigorously modeled multipath-rich environment. The reason for having less than full 6 DOF is attributed to the coupling between the electric and magnetic fields, which impacts the independence between the vectorial and functional orthogonality.

For the tripole scenario, the full-rank 3 DOF can be closely approached. Nevertheless, there are few occurrences of PID<2. In spite of the 2 DOF of each plane-wave component, their summation may accidentally yield lower dimensionality. As pointed out in chapter 3 (sub-section 3.1.4), this observation can be explained by a destructive interference that suppresses one out of the available 3 components of the electric field while there is a discrepancy in the values of the other 2 components (similar to case 3 and 4 in Table 4.1). In the hexapole case, such suppression of 3 or more out of the 6 components of the electric and magnetic fields is very unlikely.

Similar to the canonical near-field free-space scenario, we can easily find the impact of the FED on the DOF by applying the plane-wave expansion on the propagating modes. In spite of the 2 DOF associated with each plane-wave component, the *summation* of all the plane wave contributions *can* yield higher DOF if the environment is sufficiently multipath-rich.

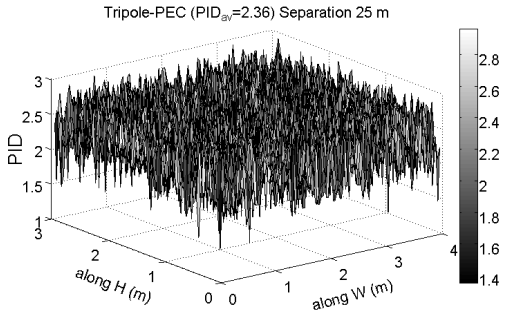

(a)

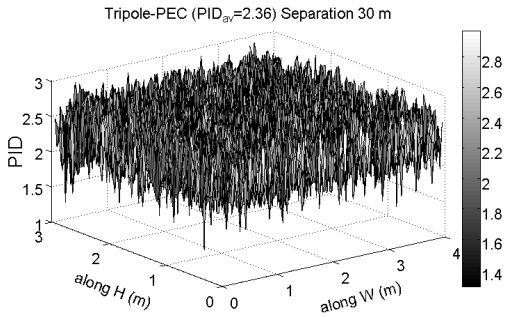

(b)

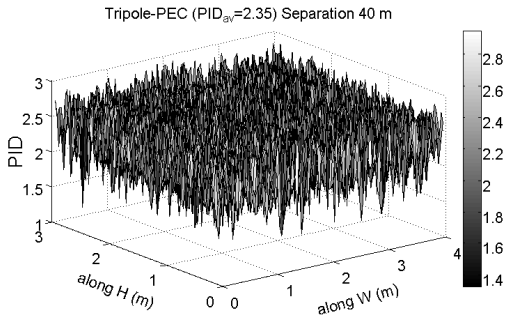

(c)

Fig. 4.4

PID of a tripole system in a PEC corridor. The receive grid is located at different separations along L

(a) 25 m (b) 30 m. (c) 40 m.

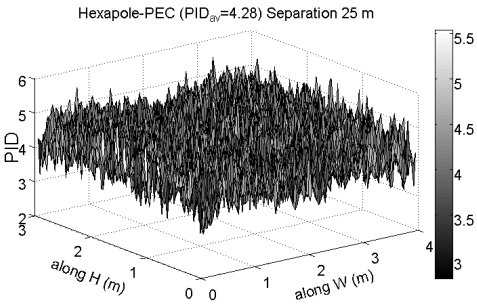

(a)

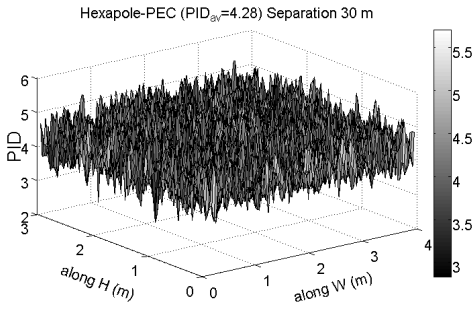

(b)

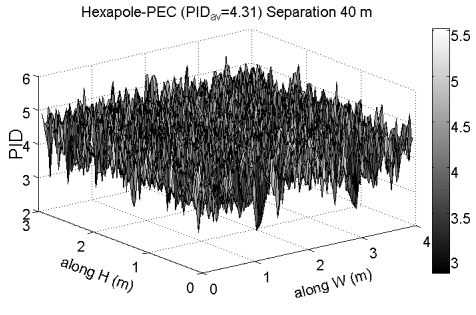

(c)

Fig. 4.5

PID of a hexapole system in a PEC corridor. The receive grid is located at different separations along L

(a) 25 m (b) 30 m (c) 40 m.

4.4 Multi-Polarization in a Lossy-Wall Corridor Scenario: IRT Simulation

The multi-polarization DOF gain is now investigated in a more practical indoor scenario. The environment is a rectangular corridor of dimensions $100\times4\times3$ m along (L,W,H), respectively. The walls thickness is 15 cm with a dielectric constant of 4 and a loss tangent of 0.02. The ceiling and floor thicknesses are 30 cm with a dielectric constant of 6 and a loss tangent of 0.05. In order to have comparable scenarios to the PEC corridor in section 4.3, the multi-polarized transmit is located at (50, 2, 2.8) along (L,W,H), respectively. The operating frequency is also 2.4123 GHz. The multi-polarized receive is moving over a grid of equidistant 20×20 points on the whole cross-section of the corridor. The simulation is repeated over 3 receive grids situated at 75, 80, 90 m along the L-axis as sketched in Fig. 4.3.

Such lossy-reflection corridor is a LOS environment and does not enjoy the same multipath richness as the PEC counterpart. We employ the IRT, discussed in chapter 3, to evaluate the channel matrix at each receive grid point. We borrow the general spherical ray expansion from (3.8) in chapter 3 to construct $\mathbf{H}^{(hexa)}$ such that each element h_{mn} is expressed as

$$h_{mn}=\sum_{l=1}^{\infty}\mathbf{e}_{ml}^{(r)T}\cdot\bar{\mathbf{D}}_{l}^{(rt)}\cdot\mathbf{e}_{nl}^{(t)}\frac{\exp(-jk_0R_l)}{R_l}, \tag{4.20}$$

where the index l represents the ray order; $\mathbf{e}_{nl}^{(t)}$ and $\mathbf{e}_{ml}^{(r)}$ are the transmit/receive vector effective length; and $\bar{\mathbf{D}}_{l}^{(rt)}$ is the far-field environment ray-dyad (2×2), which models the reflection loss and the polarization rotation along the l^{th} ray path and excludes the free space spherical propagation factor $\exp(-jk_0R_l)/R_l$. Since the 6 multipole elements are located at the same physical location, we omitted the subscripts m,n from the dyad $\bar{\mathbf{D}}_{l}^{(rt)}$, which depends only on the ray DOD/DOA, and the environment geometrical/electrical properties.

The far-field pattern/polarization of each polarized element is found through vector potential or coordinate transformation according to the framework of [SJW04]. Otherwise, we can use (3.27) in chapter 3 to get the normalized *electric* effective length of a point electric current source polarized in the $\hat{\mathbf{a}}_\xi$ direction

$$\mathbf{e} = -(\hat{\mathbf{a}}_\xi \cdot \hat{\mathbf{a}}_\theta)\hat{\mathbf{a}}_\theta - (\hat{\mathbf{a}}_\xi \cdot \hat{\mathbf{a}}_\varphi)\hat{\mathbf{a}}_\varphi \tag{4.21}$$

and then apply the duality principle to get that of a point magnetic source. The normalized effective length of each polarized element is shown in Table 4.2.

Table 4.2. Far-Field Pattern/Polarization of the Multipoles [SJW04]

	Electric point source			Magnetic point source		
Axis	x	y	z	x	y	z
i	1	2	3	4	5	6
$e_{i\theta}$	$-\cos\theta\cos\varphi$	$-\cos\theta\sin\varphi$	$\sin\theta$	$\sin\varphi$	$-\cos\varphi$	0
$e_{i\varphi}$	$\sin\varphi$	$-\cos\varphi$	0	$\cos\theta\cos\varphi$	$\cos\theta\sin\varphi$	$-\sin\theta$

Since there is a linear algebraic dependence between the transverse components of the magnetic and electric field along each ray, the multipole PID *per ray* can never exceed 2 (the partial vectorial orthogonality of one field) and thus the IRT simulator needs to trace the *electric field* only. However, the summation (4.20) introduces a third vectorial DOF [AMC01] as well as the functional orthogonality due to the pattern orthogonal weighting (pattern diversity or FED), which is modeled by $\mathbf{e}_{nl}^{(t)}$ and $\mathbf{e}_{ml}^{(r)}$.

In chapter 3, we found out that few hundred rays are sufficient to yield a convergent solution in the case of transparent walls (small LT). We employ in the simulations herein the most significant 1000 rays, which are traced from the fixed multi-polarization transmit to the moving multi-polarization receive at each grid point. Fig. 4.6a-c and 4.7a-c show the PID over the grid locations using tripoles and hexapoles, where the average PID is 1.9 and 2.4, respectively.

The lack of multipath-richness due to the transparent (lossy) walls has significantly reduced the DOF in comparison with the PEC corridor. Rapid fluctuation of the PID over short distances can also be seen similar to the PEC case. The standard deviation of the Frobenius norm (in dB) of the channel matrix over the 400 receive points in each cross-section grid scenario is about 6 dB for both the hexapole and tripole systems. Therefore, the assumption of essentially power-similar scenarios is valid, which makes the PID results acceptable.

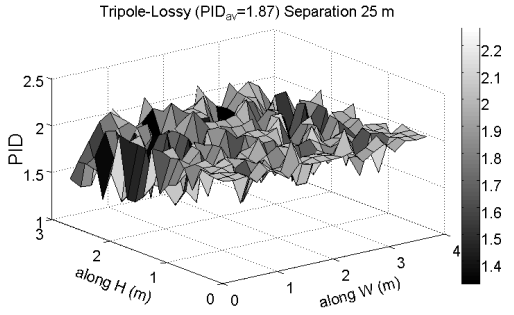

(a)

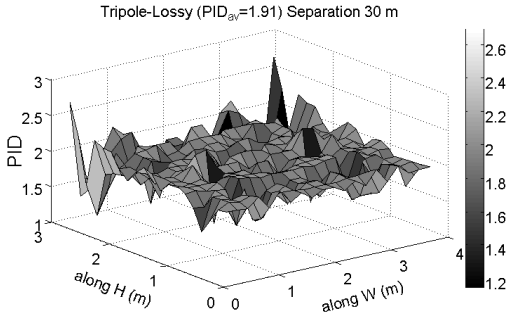

(b)

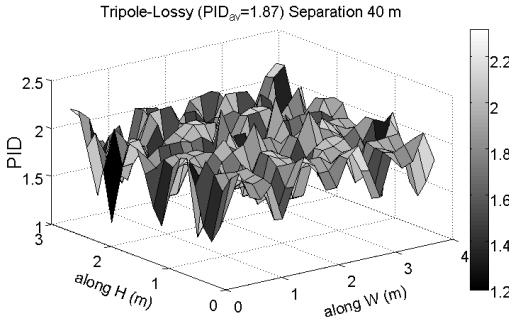

(c)

Fig. 4.6

PID of a tripole system in a lossy corridor. The receive grid is located at different separations along L

(a) 25 m (b) 30 m (c) 40 m.

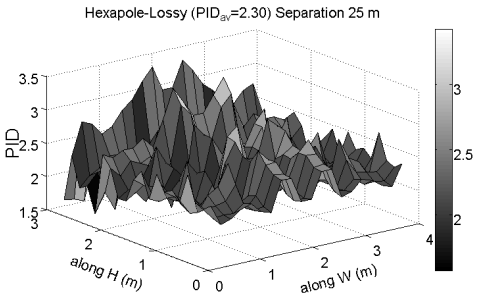

(a)

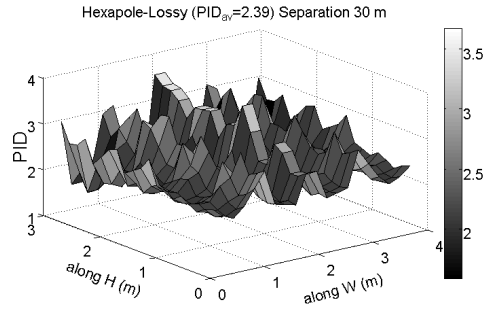

(b)

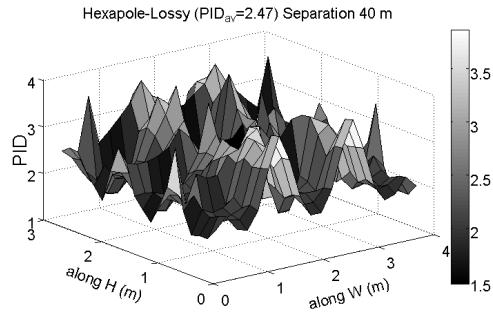

(c)

Fig. 4.7

PID of a hexapole system in a lossy corridor. The receive grid is located at different separations along L

(a) 25 m (b) 30 (c) 40 m.

4.5 Summary and Discussion

In this chapter we investigated the DOF gain provided by a collocated multi-polarization antenna system in 3 case studies. The first 2 canonical cases, the near-field free-space and PEC corridor, represent a rigorously derived multipath scenario which is very rich, however, the full-rank 6 DOF was never achieved through a hexapole system. Therefore, the stochastic modeling of the channel matrix in the literature is not adequate to draw some conclusions regarding the DOF performance of the multipole system since it disregards the coupling between the electric and magnetic fields.

Also, by applying the plane-wave (or spherical ray) expansion on the field in all the 3 studied cases, we showed that the individual 2 DOF per plane-wave component is not automatically a bottle-neck to the system DOF. The incoming plane waves at different directions result in a higher DOF of the system, which is attributed to the FED (also known as far-field pattern diversity or functional orthogonality) in addition to the obvious vectorial (polarization) orthogonality by creating one more component in the resultant field. However, it can happen that the plane wave contribution yields less than 2 DOF as observed in the case of the tripole system in the multipath rich PEC waveguide.

A rich scattering environment is needed in order to achieve an acceptable DOF performance through a multipole system. We repeated the PEC corridor simulations with the transmit multipole situated at various locations and we obtained the same average PID for the tripole and hexapole systems as those of Fig. 4.4-5. One can argue that the open-ended PEC waveguide has only a hemi-spherical angular spread of the rays and thus it is not as multipath-rich as the optimum PEC enclosure. In order to examine this argument, we made other simulations in a PEC corridor with only one open end. We placed the transmit multipole and the receive grid at L=50 and L=75m, respectively and a PEC wall is located at L=100 m. Therefore, we have full receive angular spread over the

spherical solid angle. We repeated the modal analysis (the multipole source and its image) and we obtained very similar results to Fig. 4.4-5.

We show a comparison between the PID normalized histogram of the PEC and lossy-wall (LT~0.01) corridor multipole scenarios in Fig. 4.8. At each cross-section grid, we have 10^4 and 400 points for the PEC and lossy-wall corridor, respectively. The bin size for the normalized histogram, spanning the PID values from 1 to 6, is 0.1. In the multipath-rich PEC case, the histogram in Fig. 4.8 indicates that by using a tripole system, there is some probability of achieving a PID close to the full-rank 3 DOF and also the PID can happen to be less than 2. On the other hand, the hexapole system almost guarantees more than 3 DOF, however, it never attains the full 6 DOF. The lossy-wall corridor, lacking multipath richness, yielded significant PID reduction and the gap between the tripole and hexapole PID average value decreases.

We conclude by summarizing the concepts and findings of this chapter:

- There are 2 types of orthogonality (vectorial and functional) responsible for the diversity when using electric and magnetic multipole systems. These 2 types of orthogonality are inter-winded due to the inevitable coupling between the electric and magnetic field components.
- In a sufficiently multipath-rich environment, a tripole system may provide very close PID to the maximum full-rank 3 DOF. A hexapole system does not automatically double the tripole dimensionality (6 DOF were never achieved), however, the hexapole system produces, in general, higher DOF (more than 3 DOF are almost guaranteed).
- The average PID is environment-dependent and seems to be independent of the geometrical setup (location of the transmit/receive multipole elements). The gap between the hexapole and tripole PID values decreases as the multipath richness decreases.

In the next chapter, we will combine the multipole system with a spatial array to form a multi-polarized spatial MIMO *sampler* (in contrast to the point multipoles investigated herein). Given a specific size of the array (1D, 2D or 3D), we investigate the upper limit of DOF when using all the available spatial diversity (space, pattern and polarization).

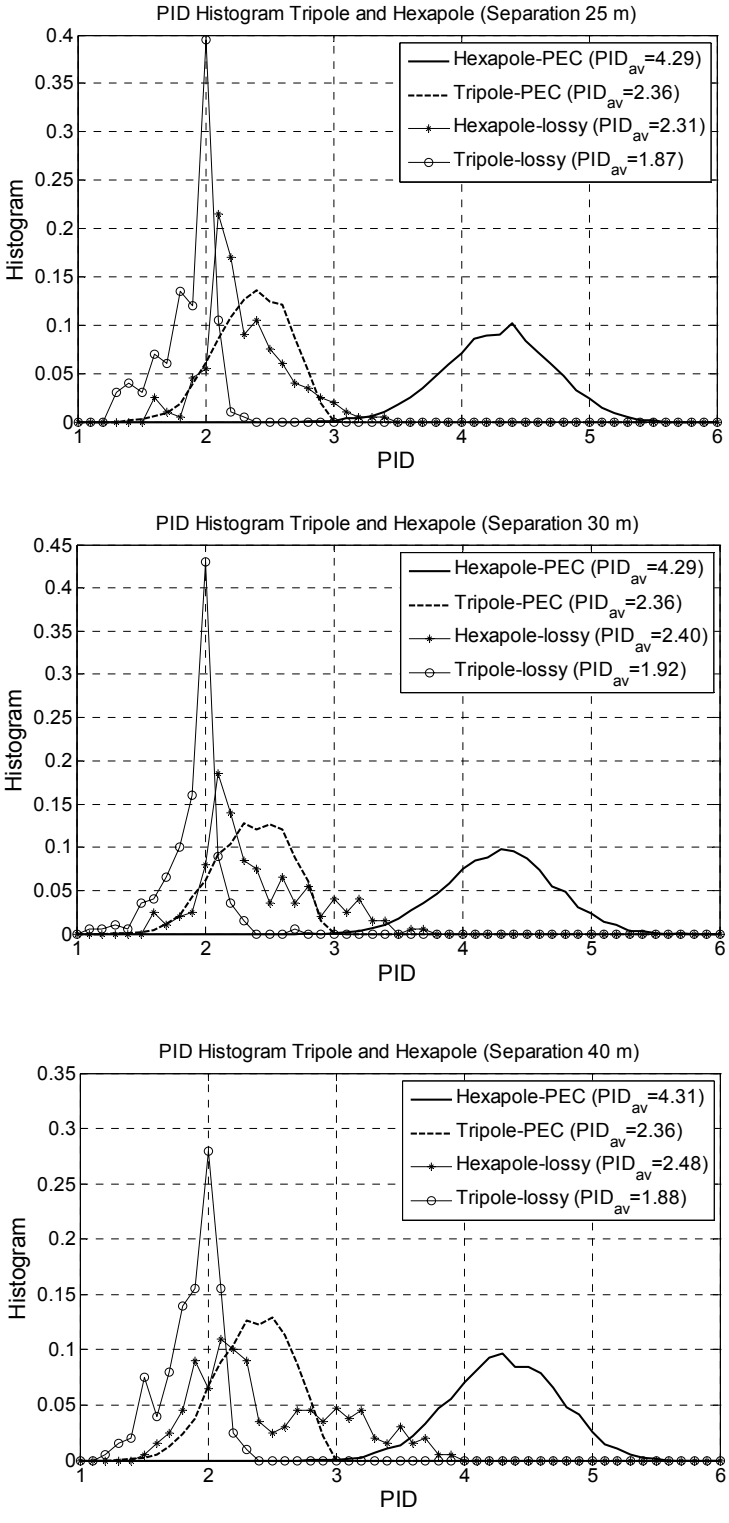

Fig. 4.8

Normalized histogram of the tripole and hexapole systems PID in the PEC and lossy corridor. The receive grid is located at different separations along L (a) 25 m (b) 30 m (c) 40 m.

Chapter 5
Dimensionality of Size-Specific Multi-Antenna Systems

In chapter 2, we developed the dimensionality metric required to measure the parallel sub-channels performance (DOF) of MIMO systems. We modeled the electromagnetic propagation in chapter 3. The collocated multi-polarization effect (Maxwellian framework) was studied in chapter 4. We are ready to explore in this chapter the maximum dimensionality performance of MIMO systems. Given an array of a fixed size in a site-specific environment, we investigate the maximum achievable PID through the combination of both the spatial and the pattern/polarization diversity. The target is two-fold: evaluate the maximum available dimensionality according to the information-carrying ability of the electromagnetic field, then get an estimate of the minimum number of antennas required to achieve it.

We start by showing the region of existence (ROE) of the spatial frequency spectrum for the generic 3D arrays, which can be promptly reduced to the 1D or 2D array cases by a simple projection. Accordingly, we show the effect of the

environment properties and array orientation on the DOF in the context of the k-domain ROE. Next, we compare the optimum sampling results to the DOF of essentially time-limited bandlimited 1D functions. Afterward, we extend the 1D optimum sampling results to the 2D and 3D array cases, sustained by numerical simulation based on the PID metric. Finally, we present numerical results for the PID of multi-polarized MIMO system of a given array size (1D, 2D and 3D) in a PEC and lossy-walls corridor.

5.1 ROE of the EM Fields Angular Spectrum

In appendix C, we present the spatial-frequency domain (also known as the k-domain or angular domain) of the electromagnetic fields. At any source-free point of space, such as where the electromagnetic detector will be installed, the electromagnetic homogeneous wave equation implies that the ROE of the spectral domain is as shown in Fig. 5.1. An arbitrary direction of wave propagation/evanescence is selected (in Fig. 5.1 it is the positive z-axis) in order to make the plane-wave expansion. Accordingly, the hemispherical *surface* $k_z = +\sqrt{k_0^2 - k_x^2 - k_y^2}$ for $k_x^2 + k_y^2 \le k_0^2$ represents the ROE of propagating plane-wave spectrum. The evanescent spectrum is not considered since the transmit/receive separation is assumed large enough to suppress these components. When the environment forms an enclosure structure (e.g. a cavity), an additional lower hemispherical surface should be considered as well to account for the propagating wave components down the negative z-axis. Therefore, in a source-free region, the general *propagation* ROE of electromagnetic wave spectrum is the spherical *surface* $k_x^2 + k_y^2 + k_z^2 = k_0^2$, which represents the full visible angular spectrum ($\theta \in [0, \pi]$ and $\varphi \in [0, 2\pi]$).

In Fig. 5.1, we show the location of high and low order propagation modes in a waveguide structure. Around the pole of the sphere, the components represent low order modes or in ray tracing analysis, this is equivalent to rays

traveling almost along a LOS or with few encountered reflections [RWV94]. On the other hand, as we approach the equator at the traveling/evanescent boundary, we find the high order modes (approaching the cut-off frequency), which are equivalent to rays encountering many bounces. Thus for lossy-walls environments, after choosing the LOS direction as the propagation axis, the expansion components located around the pole have a more significant contribution than those near the equator since the latter suffer from heavy power loss due to the multi-reflection. Hence, the lossy-wall environment effect can be viewed as reducing the effective k-bandwidth [BF87, BF89].

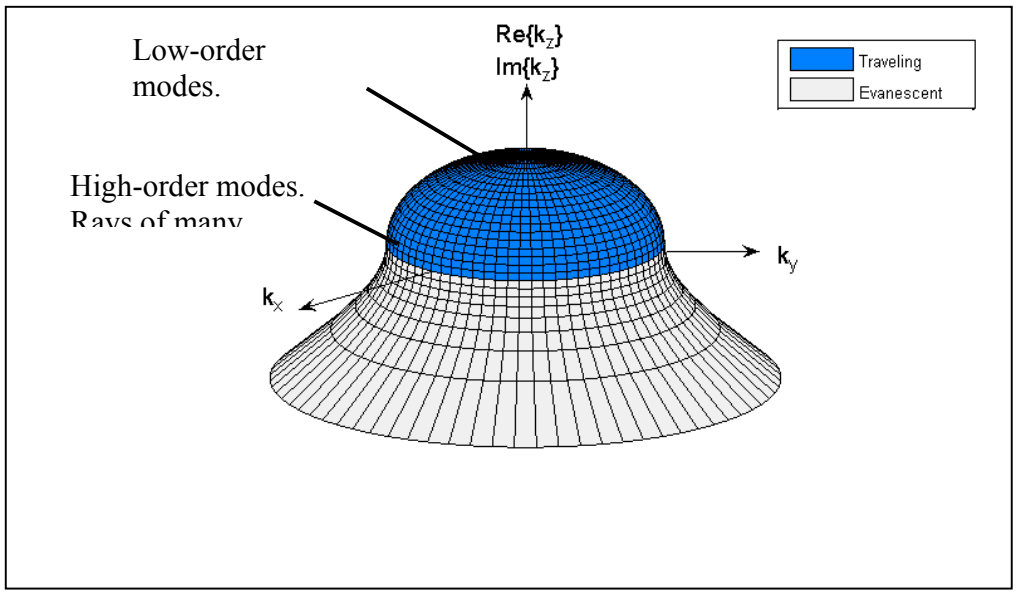

Fig. 5.1 Region of existence (ROE) of the EM fields spectrum in the k-domain for the half-space z>0. The locations of low and high order modes in a waveguide are indicated.

From now on, we will use the spatial frequency domain [Goo96], which is a scaled version of the k-domain: $(f_x, f_y, f_z) = \frac{1}{2\pi}(k_x, k_y, k_z)$. As explained in appendix C, The ROE intercepts each axis of the f-domain at $\frac{1}{\lambda}$, where λ is the free space wavelength. The f-domain spectrum is obtained through the Fourier

transform of the field along the axis of interest. In general, the 3D transform pairs are given by

$$\overline{\overline{E}}(f_x,f_y,f_z)=\int_{-\infty}^{\infty}\int_{-\infty}^{\infty}\int_{-\infty}^{\infty}\overline{E}(x,y,z)e^{j2\pi(f_x x+f_y y+f_z z)}dxdydz \tag{5.1}$$

$$\overline{E}(x,y,z)=\iiint_{\mathrm{ROE}}\overline{\overline{E}}(f_x,f_y,f_z)e^{-j2\pi(f_x x+f_y y+f_z z)}df_x df_y df_z\ . \tag{5.2}$$

If a 1D array is oriented along the x-axis, we are interested in the f_x spectrum of the field. This can be readily obtained from the general 3D f-domain as follows

$$\begin{aligned}\overline{E}(x,y,z)&=\int_{\mathrm{ROE}_{f_x}}df_x e^{-j2\pi f_x x}\iint_{\mathrm{ROE}_{f_y,f_z}}df_y df_z\,\overline{\overline{E}}(f_x,f_y,f_z)e^{-j2\pi(f_y y+f_z z)}\\&=\int_{\mathrm{ROE}_{f_x}}df_x e^{-j2\pi f_x x}\,\overline{\overline{E}}(f_x,y,z)\end{aligned}\ , \tag{5.3}$$

showing that we are performing a 1D Fourier transform. The 1D ROE is the projection of the 3D spherical shell on the f_x axis. In this case, ROE_{f_x} is $|f_x|\le\frac{1}{\lambda}$, characterizing a 1D f_x-bandlimited field.

For a 2D array oriented along the x- and y-axis, we follow the same approach to obtain

$$\begin{aligned}\overline{E}(x,y,z)&=\iint_{\mathrm{ROE}_{f_x,f_y}}df_x df_y e^{-j2\pi(f_x x+f_y y)}\int_{\mathrm{ROE}_{f_z}}df_z\,\overline{\overline{E}}(f_x,f_y,f_z)e^{-j2\pi f_z z}\\&=\iint_{\mathrm{ROE}_{f_x,f_y}}df_x df_y e^{-j2\pi(f_x x+f_y y)}\,\overline{\overline{E}}(f_x,f_y,z)\end{aligned} \tag{5.4}$$

and in this case, the 2D ROE is the projection of the 3D spherical shell on the (f_x,f_y) plane and ROE_{f_x,f_y} is ${f_x}^2+{f_y}^2\le\frac{1}{\lambda^2}$, characterizing a disc (bandlimited field) in the (f_x,f_y) plane. When the spectrum cuts off at the same spatial frequency magnitude in all directions, it is called isotropic [PM62], i.e. its ROE is a hypersphere in the general N-dimensional domain.

Based on the previous discussion, the array geometry (being 1D, 2D or 3D) and orientation determine the ROE. In a waveguide environment, of longitudinal direction along $\hat{\mathbf{a}}_\eta$, we have only one propagating hemisphere. A 1D linear array orthogonal to $\hat{\mathbf{a}}_\eta$ (broadside array) makes the 1D spectrum f-bandwidth equal to $\frac{2}{\lambda}$, whereas for a 1D linear array parallel to $\hat{\mathbf{a}}_\eta$ (endfire array), the bandwidth is $\frac{1}{\lambda}$. Similarly, for 2D array orthogonal to $\hat{\mathbf{a}}_\eta$, the ROE is a *disc* of radius $\frac{1}{\lambda}$, while for a 2D array oriented parallel to $\hat{\mathbf{a}}_\eta$, the ROE is a *semi-disc* of radius $\frac{1}{\lambda}$. These ROE shapes have a crucial role in determining the DOF of the size-specific multi-antenna systems, as will be discussed in the next section.

5.2 DOF and Optimum Sampling over a Finite-Array Size: Scalar Isotropic Sampler

In this section, we investigate the DOF of the electromagnetic fields for 1D, 2D and 3D arrays subject to the ROE of the spectrum, by using isotropic scalar sampling element (i.e. neglecting the multi-polarization effect for the moment). We will link the prolate spheroidal wave function (PSWF) results presented in appendix A to the optimum sampling of the 1D problem. Afterward, we extend the optimum sampling results, as a measure of the DOF, to the 2D and 3D arrays.

5.2.1 Electromagnetic DOF Problem in the Literature

It is a well-known fact in the optics community that the space-bandwidth product [Goo96], also known as the Shannon number [Tor55, Gab61, Tor69,

GG73], determines the DOF of the function within the aperture. The information transfer mechanism in optics is based on the *scalar* diffraction theory [Goo96] in *free space* according to the source resolution. In the electromagnetic propagation, the information transfer obeys the more rigorous Maxwellian framework and deviates from the optics assumptions regarding the *vectorial* nature of the fields which propagate in *bounded* environments. However, there is a common concept in both: the spectrum bandlimitedness. Therefore, we expect that the concept of the space-bandwidth product still applies for the electromagnetic propagation with some modification.

The EM-DOF problem was investigated and re-investigated several times. Bucci et al. [BF87, BF89, BGS98] investigated the non-redundant number of samples to represent the electromagnetic fields over arbitrary surfaces. Some recent MIMO-DOF works are following this approach (e.g. [Mig06]), where it is implicitly assumed that the environment and transmitter (source) are treated as one entity and therefore, such results are more suitable for *outdoor* MIMO systems. Both the *significant* number of singular values and the capacity were used as a measure of dimensionality in [Mig06].

Miller and Piestun [Mil00, PM00] investigated the orthogonal communication channels between 2 *volumes* based on the PSWF framework, originally for scalar wave followed by the vectorial electromagnetic fields. They reported the similarity of the PSWF approach and the singular value decomposition. Nevertheless, their results were basically for the open free-space (no boundary), with possible scatterers between the transmit/receive ends. This environment assumption is more suitable for optics. This is the reason why in [PM00], only 2 DOF for the hexapole system were reported, in the absence of noise, since the system is equivalent to one ray in the far-field. Recently, Xu and Janaswamy [XJ06] followed this approach for MIMO-DOF investigation in 2D environments. They defined a SNR-based DOF which is the maximum number of transmit modes that can excite receive modes stronger than the noise level,

under the transmit power constraint. They also reported an observation which is consistent with the tight bound property of the PID matrix product inequality (2.8) when the 2 matrices are of widely different dimensionalities. However, the multi-polarization or array orientation effects were not clearly investigated

Poon et al. [PBT05] tackled this problem, deterministically at the the transmit/receive geometry level and statistically at the environment level, based on the angular domain approach. They employed the MIMO capacity as a dimensionality measure at a given SNR. They reported the same space-bandwidth product result of the optics community and they considered the array orientation effect. However, their approach does not rigorously consider the multi-polarization effect as mentioned in chapter 4, neither do they explicitly link the DOF to the array dimension (being 1D, 2D or 3D).

Based on the modal orthogonality in a PEC waveguide, Loyka [Loy05] essentially used the number of propagating modes to measure the MIMO-DOF. However, this requires that the array aperture be situated across the *whole cross-section* of the guide or at least over one dimension of its cross-section. More recently, Loyka and Mosig [LM06] tackled the link between the electromagnetism and information theory based on the bandlimitedness of the f-domain, which is the same path we are following in this chapter. They reported the supreme DOF limit assuming a perfect scattering environment. Nevertheless, the link with multi-dimensional sampling and the multi-polarization effect were not clearly stated.

5.2.2 PSWF-DOF and Optimum Sampling of 1D Bandlimited Functions

In appendix A, we report the celebrated result of Landau and Pollak [LP62] regarding the DOF of "essentially" time- and frequency- limited functions. The beauty of this theorem is that it rigorously quantifies the ambiguous term

"essentially", which was previously used in studying the DOF from a sampling point of view. The complexity arises from the fact that we can not have a function $y(t)$ which is both time-limited and bandlimited unless it is identically zero everywhere. Therefore, for the spectrum of $y(t)$ strictly limited to $|f|<W$, we assume that most of the energy of $y(t)$ is confined within $|t|<T/2$ such that

$$\frac{\int_{-T/2}^{T/2} |y(t)|^2\, dt}{\int_{-\infty}^{\infty} |y(t)|^2\, dt} = 1-\varepsilon_T^2, \tag{5.5}$$

where ε_T^2 represents the negligible portion of "tail" energy outside the time window [LP62]. Therefore, $y(t)$ can be reconstructed, *over the entire t-domain*, through $\lfloor 2WT+1 \rfloor$ *optimum* basis functions (scaled PSWFs) such that the reconstruction square error is bounded by

$$\int_{-\infty}^{\infty} |y(t) - \sum_{n=0}^{\lfloor 2WT \rfloor} a_n \psi_n(c,t)|^2\, dt < 12\varepsilon_T^2, \tag{5.6}$$

where $\lfloor x \rfloor$ is the largest integer $\le x$.

Next, let us consider the DOF problem from an optimum sampling perspective. The sampling theorem was investigated since the early 20th century by Whittaker, Nyquist, Kotel'nikov, Shannon and others [Whi15, Nyq28, Kot33, Sha49]. It states that we can perfectly reconstruct (interpolate) the bandlimited function $y(t)$ from its uniform discrete samples provided that the later are taken at a rate $\ge \frac{1}{2W}$ samples/sec (the Nyquist rate). By choosing the slowest sampling rate (optimum sampling), we have

$$y(t) = \sum_{n=-\infty}^{\infty} y\left(\frac{n}{2W}\right) \mathrm{sinc}\left(2W\left(t - \frac{n}{2W}\right)\right), \tag{5.7}$$

where $\text{sinc}(x)=\frac{\sin(\pi x)}{\pi x}$ and is also known as the "sampling" [LP62] or "cardinal" [PM62] function. The perfect reconstruction in (5.7) requires an infinite number of samples. However, we know that each sinc function has a tail of decaying amplitude, which means that it has a local effect mostly concentrated around its sample location. Consequently, when we are only interested in the time-window $|t|<T/2$, we can expect that truncating the series in (5.7) to $|n|\le\lfloor WT \rfloor$ will yield a good approximation. Hence, using $\lfloor 2WT+1\rfloor$ samples can reconstruct the original signal well enough so that we again have $\lfloor 2WT+1\rfloor$ DOF, now from a sampling perspective.

In particular, this truncation yields good approximation when the energy confining condition (5.5) is met because the combined effect of the decaying tail of the discarded sinc functions and their small weighting amplitude for $|t|>T/2$ results in smaller truncation error within $|t|<T/2$. In [LP62 theorem 2], it is shown that the reconstruction square error using a finite series of shifted sinc functions (as a basis) is bounded by $\pi\varepsilon_T+\varepsilon_T^2$, which is worse than the case with the PSWFs, confirming the optimality of the latter as a reconstruction basis. However, the error with the sinc reconstruction is still quite acceptable in practical problems, given the advantage of the simpler expansion coefficients $y(\frac{n}{2W})$ in (5.7) in comparison with the more sophisticated a_n in (5.6) which are given by (A.11) or (A.12).

With either the PSWF or the optimum sampling, we rigorously have $\lfloor 2WT+1\rfloor$ DOF (which we will call the $2WT$ limit henceforth) for the bandlimited $y(t)$ within the window $|t|<T/2$ as long as its energy is confined according to (5.5). The condition of (5.5) is of paramount importance in setting the rigorous $2WT$ limit because otherwise, we can incorrectly "show" that it is exceeded as described in the following case.

In [FK06], the energy bound for the "superoscillation" phenomenon was reported. It is shown that the aforementioned finite-energy bandlimited $y(t)$ can have an arbitrary number N of superoscillations within $|t|<T/2$ provided that its energy increases exponentially with N. How comes that N could surpass the $2WT$ limit? The answer is that there is a huge increase in the amplitude of the superoscillating function for $|t|>T/2$ [FK06] and thus (5.5) is breached leading to an incorrect $2WT$ estimate in the first place. In fact, these superoscillating functions resemble a PSWF of higher order ψ_N, $N >> 2WT$ as reported in [FK06], where most of its energy is confined *outside* the time-window of interest.

In spite of the fact that the example just mentioned is an extreme case, it raises an important question: if there is a non-trivial energy fraction of the bandlimited signal for $|t|>T/2$, but we are *only interested* in detecting the DOF *within* $|t|<T/2$, is the $2WT$ estimate still good enough? A qualitative answer can be provided as follows: By hypothetically multiplying $y(t)$ by a smooth truncation function (say a Gaussian function), we try to preserve the region of interest $|t|<T/2$ almost intact while suppressing the irrelevant fat tail outside. Such truncation in the time domain will inevitably increase the bandwidth in the frequency domain by convolution with a reciprocally compressed version of the Gaussian function. If the dynamic range in the tail zone is not exaggeratingly higher than within $|t|<T/2$ (unlike the superoscillation for example), then the required truncating function is smooth enough in the time-domain such that the increase in the original signal bandwidth is small and the $2WT$ limit is thus acceptable. From a sampling perspective, the weighting of the sinc in the outside tail zone will not be exaggeratingly high such that the decaying tail of the discarded sinc functions will not influence the reconstruction inside the window of interest. Consequently, truncating the outer terms of the sinc

reconstruction makes a small error. In [LM06], it is reported that a slight oversampling is needed in this case in order to reduce the truncation error.

In summary, either approach (PSWF or *optimum* sampling) provides that there are $\lfloor 2WT+1 \rfloor$ dimensions for the bandlimited $y(t)$ within $|t|<T/2$. As long as the dynamic range of $y(t)$ outside the window of interest is smaller than or comparable to that within $|t|<T/2$, the $2WT$ limit is still practically correct. Accordingly, we will use the optimum sampling approach in the next sub-section to evaluate the DOF for the 1D, 2D and 3D arrays of a specific size.

5.2.3 Optimum Sampling of 1D, 2D and 3D Arrays

For a 1D linear array of size D, the DOF can be readily evaluated according to the ROE of the field spectrum. For a spatial bandwidth of $\frac{1}{\lambda}$ or $\frac{2}{\lambda}$ (endfire or broadside orientation), the optimum sampling yields $\left(1+\lfloor D/\lambda \rfloor\right)$ or $\left(1+\lfloor 2D/\lambda \rfloor\right)$ samples within the array aperture, respectively.

For the optimum sampling of the N-Dimensional space V, we employ the framework of Petersen and Middleton [PM62]. We consider a function $y(\mathbf{v}) \equiv y(v_1, v_2, ..., v_N)$ defined over V, which has its Fourier transform $\widetilde{y}(\mathbf{u}) \equiv \widetilde{y}(u_1, u_2, ..., u_N)$ in the spectral domain U according to the transform pairs

$$\widetilde{y}(\mathbf{u}) = \int_V y(\mathbf{v}) e^{-j2\pi \mathbf{u}\cdot\mathbf{v}} d\mathbf{v} \tag{5.8a}$$

$$y(\mathbf{v}) = \int_U \widetilde{y}(\mathbf{u}) e^{j2\pi \mathbf{u}\cdot\mathbf{v}} d\mathbf{u}\,. \tag{5.8b}$$

We assume that the N-Dimensional signal spectrum is bandlimited. Similar to the 1D case, we use N-Dimensional delta functions, located over the periodic N-Dimensional basis of the space V, to pick samples in the space domain. Let the

vector set $\{\mathbf{v}_1, \mathbf{v}_2, ..., \mathbf{v}_N\}$ describe the sampling basis location. Such sampling results in a corresponding repetition of the N-dimensional bandlimited spectrum, where the repetition basis is given by the vector set $\{\mathbf{u}_1, \mathbf{u}_2, ..., \mathbf{u}_N\}$ in the spectral domain U. The 2 vector sets $\{\mathbf{v}_1, \mathbf{v}_2, ..., \mathbf{v}_N\}$ and $\{\mathbf{u}_1, \mathbf{u}_2, ..., \mathbf{u}_N\}$ are related by the following *vector reciprocal* relation as given by Miyakawa [Miy59]

$$\mathbf{v}_m \cdot \mathbf{u}_n = \delta_{mn}, \tag{5.9}$$

where δ_{mn} is the Kronecker's delta. The vectors of each set $\{\mathbf{v}_1, \mathbf{v}_2, ..., \mathbf{v}_N\}$ and $\{\mathbf{u}_1, \mathbf{u}_2, ..., \mathbf{u}_N\}$ are not necessarily mutually orthogonal. Hence, from (5.9), each basis vector $\mathbf{v}_k$ is orthogonal to all $\mathbf{u}_{l \neq k}$ and its magnitude is given by $|\mathbf{v}_k| = \dfrac{1}{|\mathbf{u}_k| \cos\theta_k}$, where the N-dimensional angle θ_k is given by $\cos^{-1}(\hat{\mathbf{v}}_k \cdot \hat{\mathbf{u}}_k)$.

The optimum sampling necessitates that there be no aliasing while the repeated spectrum is closely packed in U. Therefore, to perform an optimum sampling for an N-dimensional bandlimited signal, we follow these steps:

1. Based on the bandlimited spectrum, we perform an N-dimensional optimum packing with the original spectrum and its repeated images.
2. We find the basis set $\{\mathbf{u}_1, \mathbf{u}_2, ..., \mathbf{u}_N\}$ according to the optimum packing.
3. We find the sampling basis set $\{\mathbf{v}_1, \mathbf{v}_2, ..., \mathbf{v}_N\}$ from (5.9).

Next, we perform the optimum sampling for the 2D arrays. For an endfire 2D array orientation, we know from section 5.1 that the ROE is a semi-disc of radius $\dfrac{1}{\lambda}$. After following the optimum sampling steps, we get the sampling lattice as shown in Fig. 5.2. Accordingly, a $D \times D$ square array aperture contains $\left(1 + \lfloor 2D/\lambda \rfloor\right)\left(1 + \lfloor D/\lambda \rfloor\right)$ samples.

For a 2D broadside array orientation, the ROE is a disc of radius $\frac{1}{\lambda}$. Optimum sampling in this case involves the close-packing of 2D hyperspheres (discs) [PM62] as shown in Fig. 5.3. Accordingly, it can be shown that a $D \times D$ square array aperture contains $\left\lceil \frac{1}{2}\left(1+\lfloor 2D/\lambda \rfloor\right)\left(1+\lfloor 2\sqrt{3}D/\lambda \rfloor\right) \right\rceil$ samples, where $\lceil x \rceil$ is the smallest integer $\geq x$.

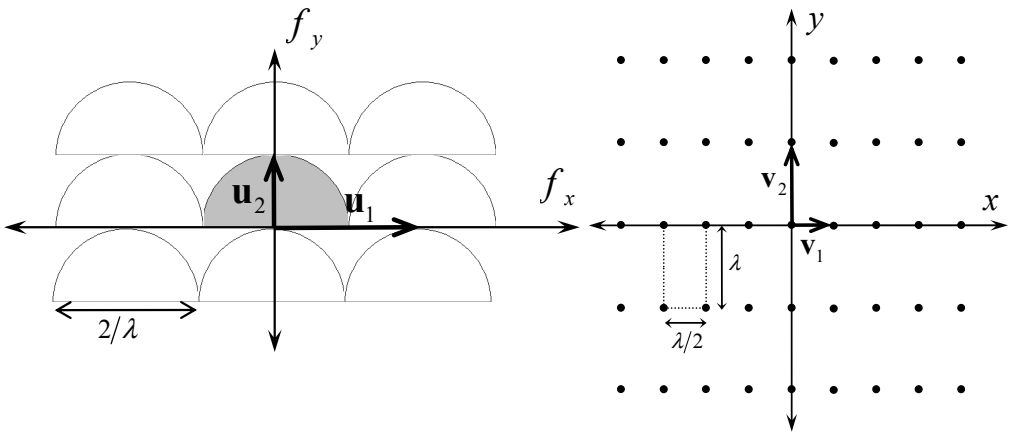

Fig. 5.2 Optimum sampling within an endfire 2D aperture.

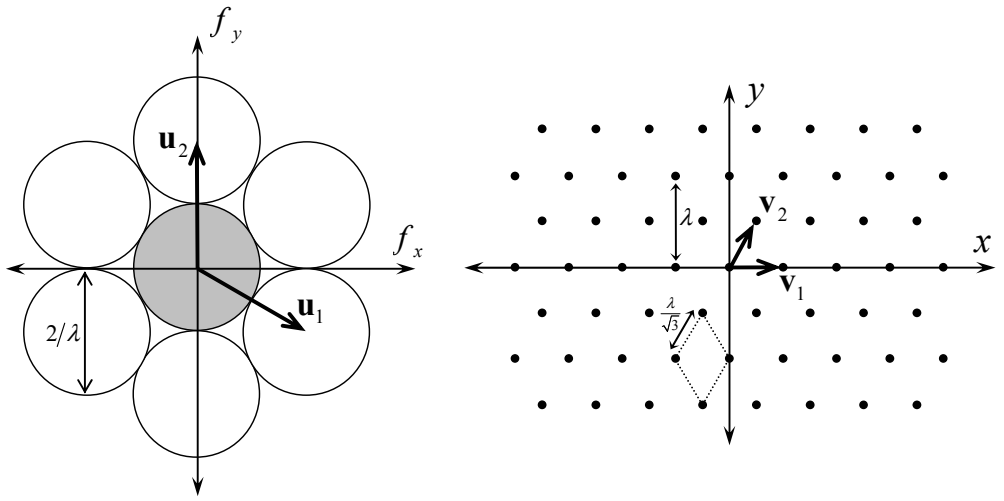

Fig. 5.3 Optimum sampling within a broadside 2D aperture [PM62].

For 3D arrays, we note that the ROE is either a spherical or hemispherical *surface* $k_x^2 + k_y^2 + k_z^2 = k_0^2$. In other words, the 3D sampling of electromagnetic fields is in fact an extended 2D one, the only difference being that the spatial bandwidth becomes quadrupled (semi-disc and disc become hemispherical and spherical surfaces, respectively). Therefore, we heuristically conjecture that the number of samples within the 3D regular array (say of a $D \times D \times D$ cube aperture) is 4 times that in the case of the corresponding 2D array ($D \times D$ square aperture). We present shortly some statistical simulations which agree with this conjecture. The number of samples (through optimum sampling) for the 1D, 2D and 3D array cases, using isotropic elements, is summarized in Table 5.1. This number can be viewed as the *scalar* DOF within the given aperture size as discussed earlier in sub-section 5.2.2. We point out that these DOF are for the scalar sampling i.e. the multi-polarization effect is not considered.

Table 5.1 DOF (Optimum Sampling) for Several Array Sizes and Orientations

Orientation	Array Size	ROE	DOF (Optimum Sampling)
Endfire	D	BW $= 1/\lambda$	$1+\lfloor D/\lambda \rfloor$
Broadside	D	BW $= 2/\lambda$	$1+\lfloor 2D/\lambda \rfloor$
Endfire	$D \times D$	Semi-disc ($R = 1/\lambda$)	$\left(1+\lfloor 2D/\lambda \rfloor\right)\left(1+\lfloor D/\lambda \rfloor\right)$
Broadside	$D \times D$	Disc ($R = 1/\lambda$)	$\left\lceil \frac{1}{2}\left(1+\lfloor 2D/\lambda \rfloor\right)\left(1+\left\lfloor 2\sqrt{3}D/\lambda \right\rfloor\right) \right\rceil$
	$D \times D \times D$	Hemispherical surface ($R = 1/\lambda$)	$4\left(1+\lfloor 2D/\lambda \rfloor\right)\left(1+\lfloor D/\lambda \rfloor\right)$
	$D \times D \times D$	Spherical surface ($R = 1/\lambda$)	$4\left\lceil \frac{1}{2}\left(1+\lfloor 2D/\lambda \rfloor\right)\left(1+\left\lfloor 2\sqrt{3}D/\lambda \right\rfloor\right) \right\rceil$

In order to examine the stated DOF results, we use the identical-element model developed in chapter 3 to compare the DOF results obtained through the PID and the optimum sampling. From the multi-keyhole form [LL06a, LL06b] in (3.14) we have

$$\mathbf{H} = \mathbf{H}^{(r)}\mathbf{A}^{(rt)}\mathbf{H}^{(t)T}. \tag{5.10}$$

We perform Monte-Carlo simulations at *one end* (say the receive end) in order to evaluate the PID of a given array size. $\mathbf{H}^{(r)} \in \mathbb{C}^{N_R \times L}$ and is constructed such that $\mathbf{H}^{(r)} = \left[\mathbf{v}_1^{(r)} ... \mathbf{v}_L^{(r)}\right]$, where

- N_R is the number of the array elements and L is the number of rays,
- $\mathbf{v}_l^{(r)}$ is the receive phase shift vector for the l^{th} ray,
- the elements of $\mathbf{v}_l^{(r)}$ are given by $v_{ml}^{(r)} = \exp[jk_0 \mathbf{a}_m^{(r)} \cdot \hat{\mathbf{a}}_l^{(r)}]$,
- $\mathbf{a}_m^{(r)}$ is the position vector of the m^{th} array element referred to the receive phase-centre (PC), and
- $\hat{\mathbf{a}}_l^{(r)}$ is the unit vector for the l^{th} ray direction of arrival under plane wavefront approximation.

We assume a total number of rays $L = 10^4$ for the 1D and 2D arrays which makes the environment quite multipath rich. Due to computational time considerations we choose $L = 5000$ for the 3D array simulations. Moreover, we assume that the azimuth angle φ of the DOA is uniformly distributed over $[0, 2\pi)$ whereas the elevation angle θ of the DOA is uniformly distributed over $[0, \pi/2)$ and $[0, \pi)$ for the hemispherical and spherical ROE, respectively, with the array orientation properly adjusted. We compute the PID of $\mathbf{H}^{(r)}$ for each case and the results (approximated to the nearest integer) are shown in Fig. 5.4.

We can observe that both the statistical PID results and the DOF based on the optimum sampling agree well enough. The largest deviation between the 2 results occurs for the 3D array with full spherical ROE. In general, the

discrepancy between the results decreases as the array size increases. So far, the polarization effect was not considered and we inherently assumed that the elements were isotropic. The multi-polarization consideration needs deterministic simulations, which are presented in the next section.

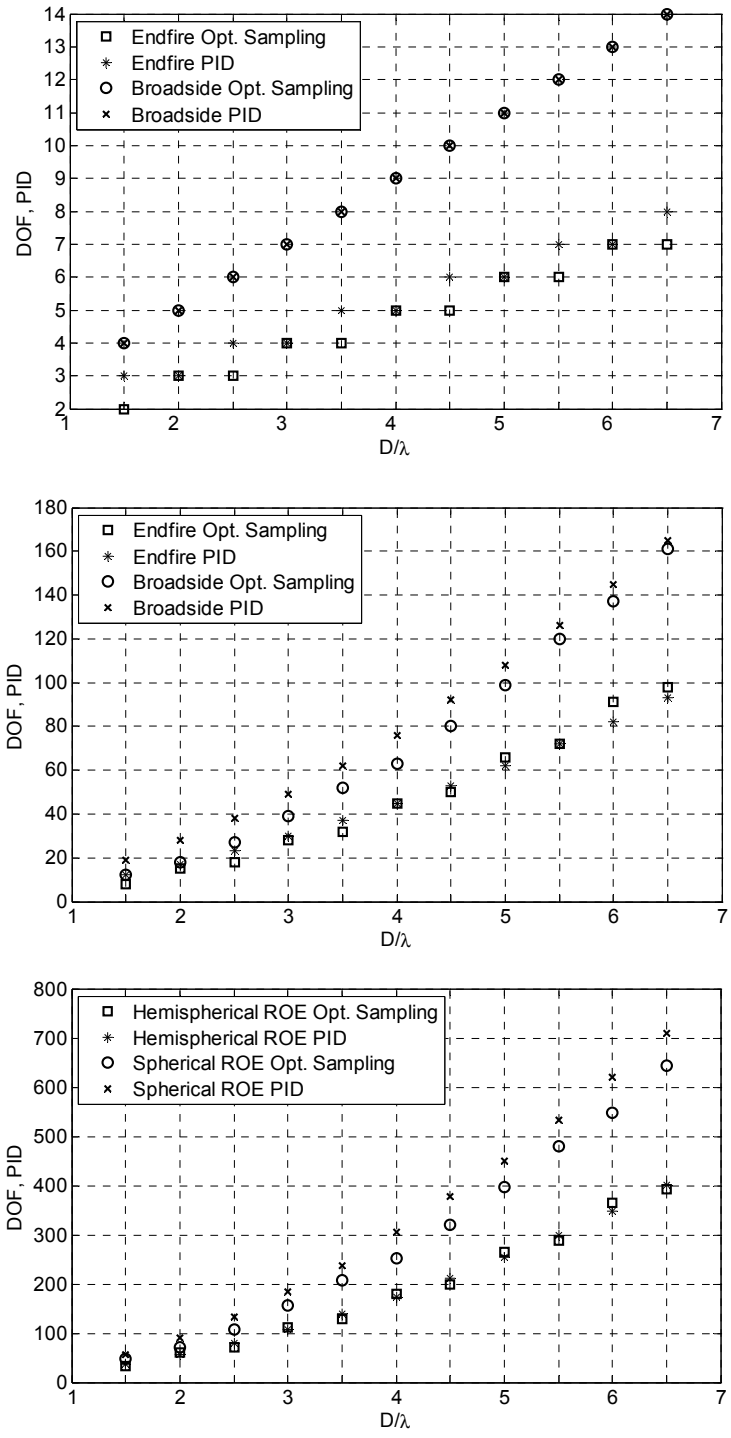

Fig. 5.4

DOF comparison using optimum sampling and PID for arrays of scalar isotropic elements (different sizes and orientations). (a) 1D array (size *D*) (b) 2D array (size *D*x*D*) (c) 3D array (size *D*x*D*x*D*).

5.3 DOF of Multi-Polarization Array in a Deterministic Scenario

In order to deterministically examine the multi-polarization effect, we perform the simulations in the PEC and lossy-wall corridor environments previously described in chapter 3 and 4. The axis along the corridor length, width and height are designated by (L,W,H), respectively. The lossy-wall rectangular corridor dimensions are $100\times4\times3$ m along (L,W,H), respectively. The transmit and receive phase-centres are located at (50, 2, 2.8) and (75, 1.5, 1.7) along (L,W,H), respectively. The walls thickness is 15 cm with a dielectric constant of 4. The ceiling and floor thicknesses are 30 cm with a dielectric constant of 6. Similarly, the PEC open-ended corridor dimensions are 4×3 m along (W,H), respectively; the transmit and receive PCs are located at (2, 2.8) and (1.5, 1.7) along (W,H), respectively and are separated 25 m along the L-axis. The operating frequency is 2.4123 GHz and correspondingly, there are 2495 propagating modes. Fig. 5.5 depicts a setup of a 2D square array of aperture size $D\times D$ and oriented along WL-WL at the transmit and receive locations. Each spatial point thereof accommodates 3 collocated infinitesimal electrical dipoles forming 3 independent ports.

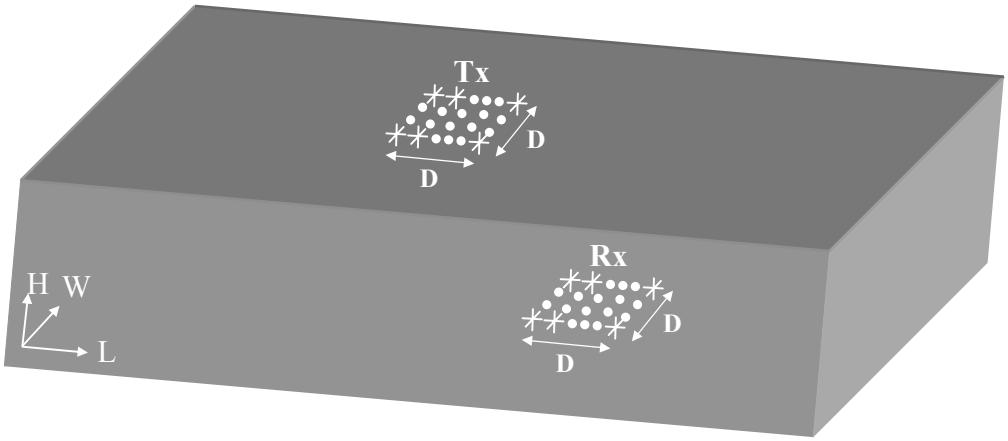

Fig. 5.5

Size-specific 2D MIMO array along WL-WL in a corridor. At each spatial point, there is a collocated tripole (3 physical ports).

In the PEC corridor, we make a 1D spatial Fourier transform of the electric field modal solution (given in appendix B) in response to a tripole excitation located at (2, 2.8) along (W,H). The spectrum along (f_W, f_L, f_H) is shown in Fig. 5.6 for all the transmit/receive polarization combination. $|E_{ij}(f_k)|$ denotes the electric field amplitude spectrum, after performing the Fourier transform along the axis k, when the transmit and receive are polarized along the axes j and i, respectively.

From Fig. 5.6, it is obvious that spatial bandwidth is as expected ($\frac{2}{\lambda}$ and $\frac{1}{\lambda}$ for broadside and endfire orientations, respectively). However, the spectrum is not uniform over the bandwidth. In other words, the effective bandwidth is smaller than the maximum value based on the ROE which leads to that the PID of a uni-polarized array is smaller than the isotropic scalar case. This is an inevitable consequence of working under the Maxwellian framework, where the polarized point source must have a pattern (null at the end-fire direction of the infinitesimal dipole) [SSWB03, SBY+06]. We also note that there could be a large gap between the spatial spectral power density for different polarizations.

We plot the PID results in the described scenario versus the number of tripoles (equidistantly packed within the given aperture size) for 3 orientations of the 1D transmit-receive arrays along W-W, L-L, and H-H in Fig. 5.7-9, respectively. For each orientation, we use different array lengths. In the lossy-wall scenario, we repeat the simulations for various loss-tangent (LT) values of the walls ranging from "transparent" lossy-dielectric ($\mathrm{LT} \sim 10^{-2}$) to "reflective" lossy-conductor ($\mathrm{LT} \sim 10^{2}$). The PID in the IRT simulations is evaluated using 10^4 rays, which are ordered according to their contribution significance as discussed in chapter 3.

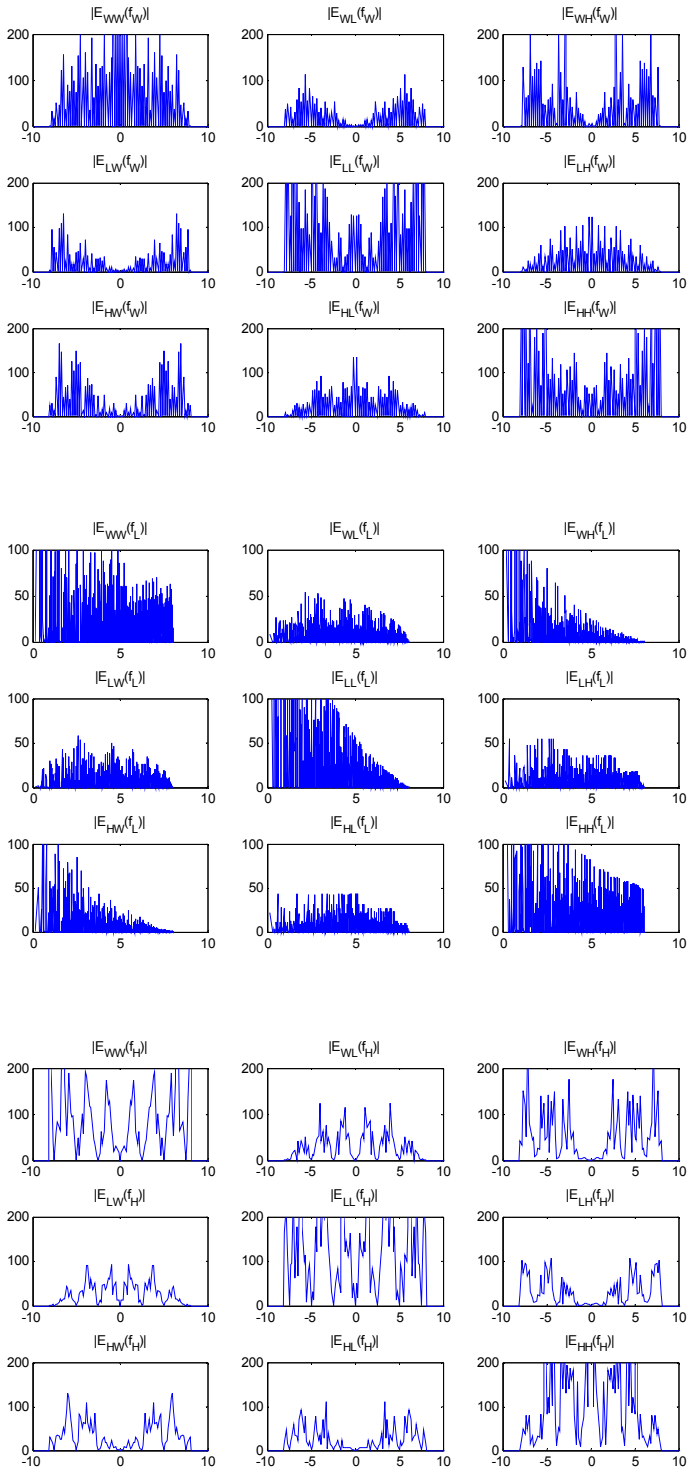

Fig. 5.6

1D spatial frequency spectrum of a multi-polarized system in a PEC open-ended corridor. (a) over W-axis (b) over L-axis (c) over H-axis.

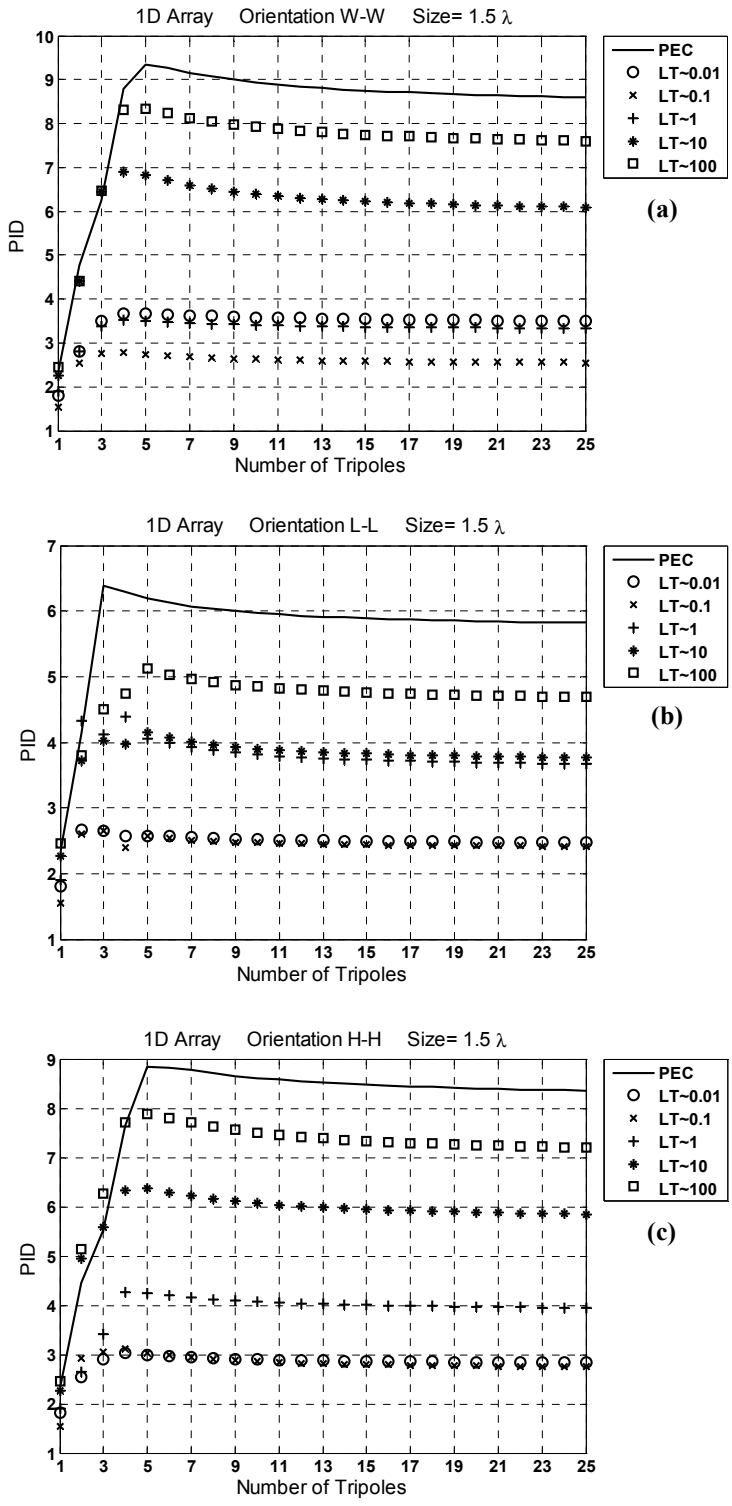

Fig. 5.7

PID of multi-polarization 1D MIMO system of aperture size 1.5λ in PEC and lossy-walls corridor. The array is oriented as (a) W-W (b) L-L (c) H-H.

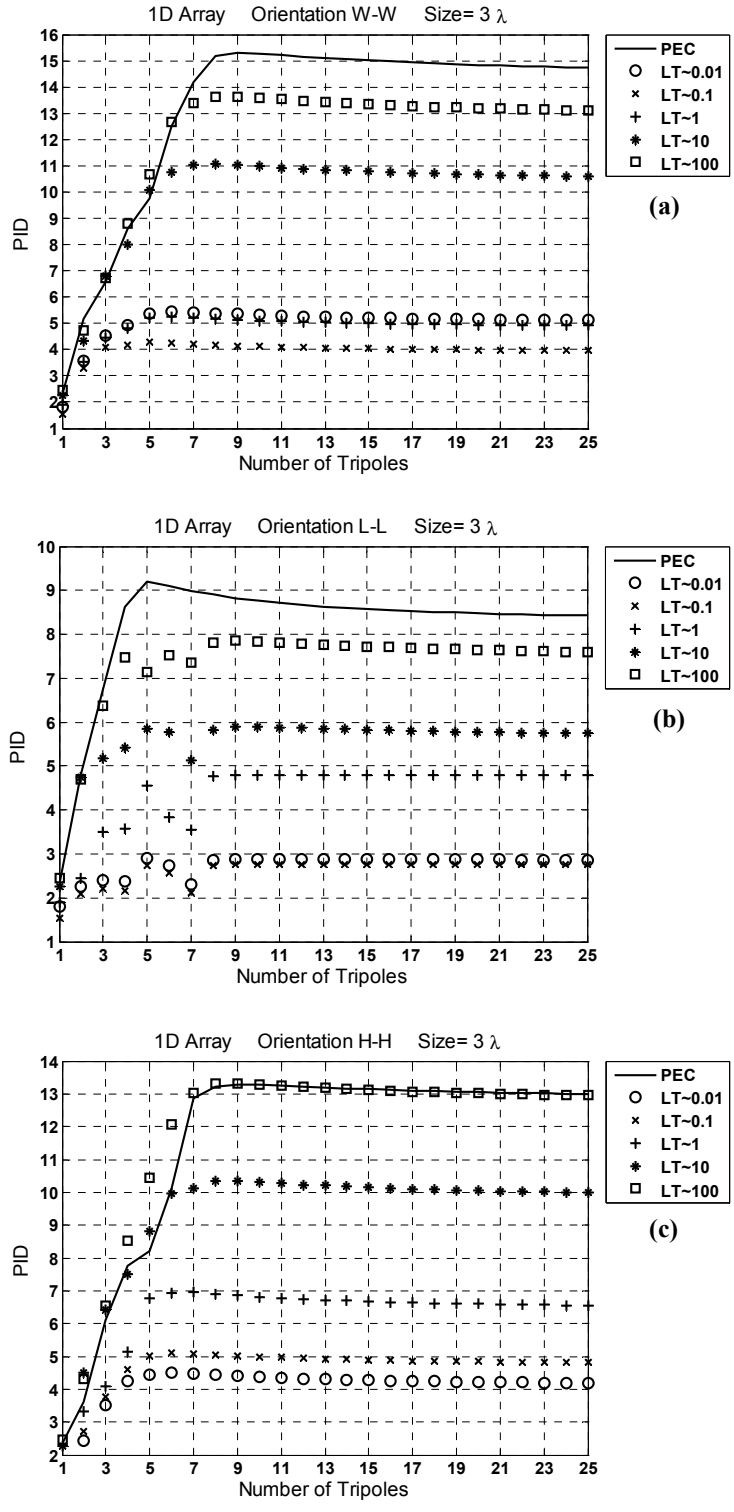

Fig. 5.8

PID of multi-polarization 1D MIMO system of aperture size 3λ in PEC and lossy-walls corridor. The array is oriented as (a) W-W (b) L-L (c) H-H.

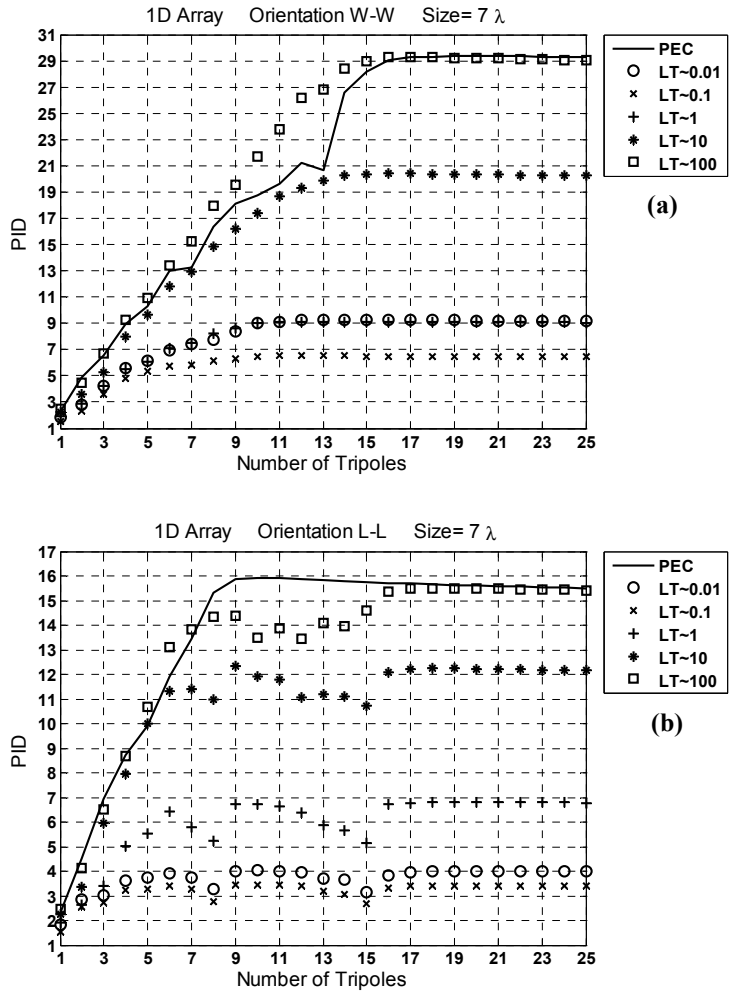

Fig. 5.9

PID of multi-polarization 1D MIMO system of aperture size 7λ in PEC and lossy-walls corridor. The array is oriented as (a) W-W (b) L-L.

In Fig. 5.10-11, we plot the PID results when using 2D square arrays of sizes $1.5\times1.5\lambda^2$ and $3\times3\lambda^2$ having different orientations at the transmit/receive ends. The tripole elements are uniformly deployed over both dimensions of the square aperture. Although this is not the optimum sampling as pointed out before for the 2D cases, we deliberately introduced some oversampling to accurately capture the saturation PID value. For the IRT simulations, we use 10^4 rays. Due to the heavy computational cost, we only simulated up to 8 tripoles per array edge (64 tripoles per aperture) for the lossy-walls cases.

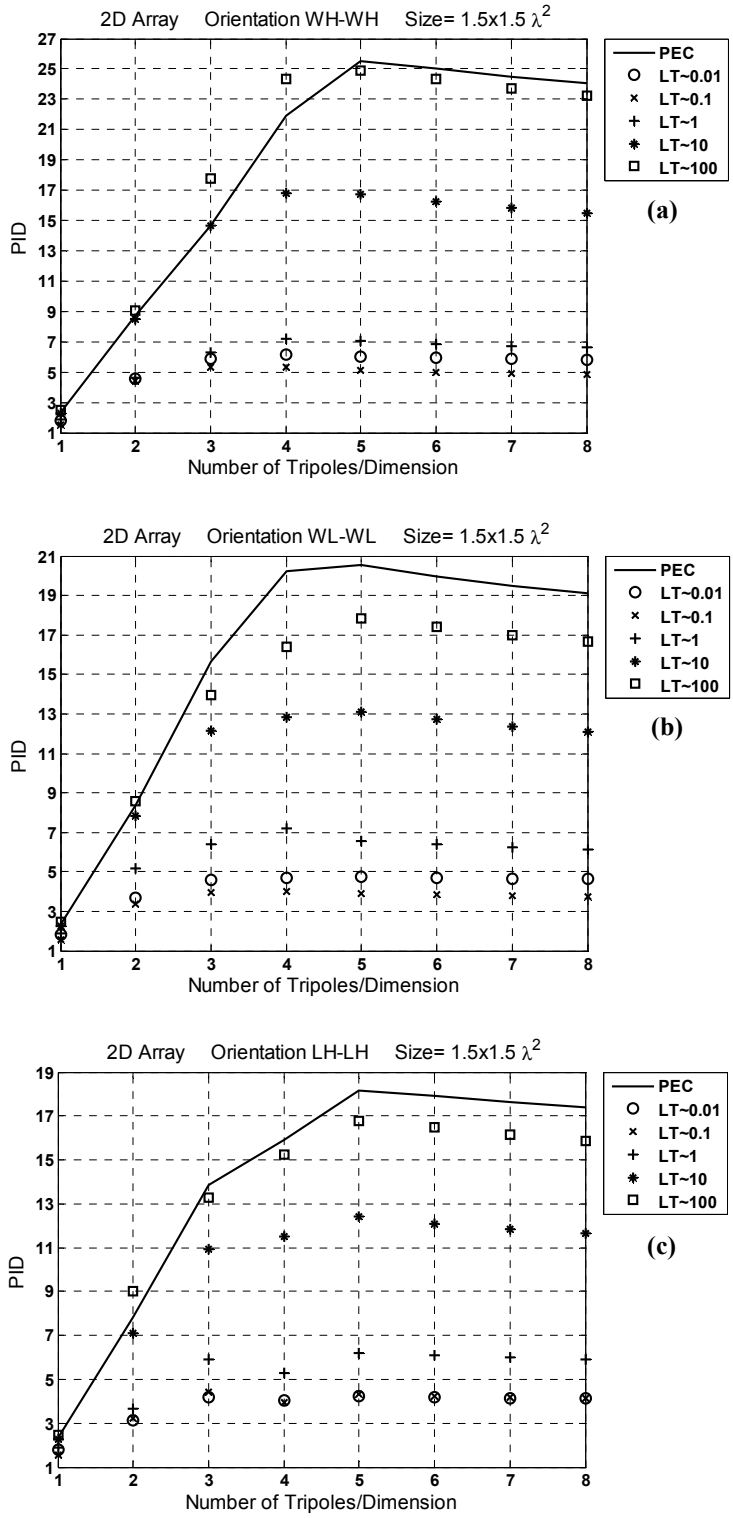

Fig. 5.10

PID of multi-polarization 2D MIMO system of aperture size $1.5\times1.5\lambda^2$ in PEC and lossy-walls corridor. The array is oriented as (a) WH-WH (b) WL-WL (c) LH-LH.

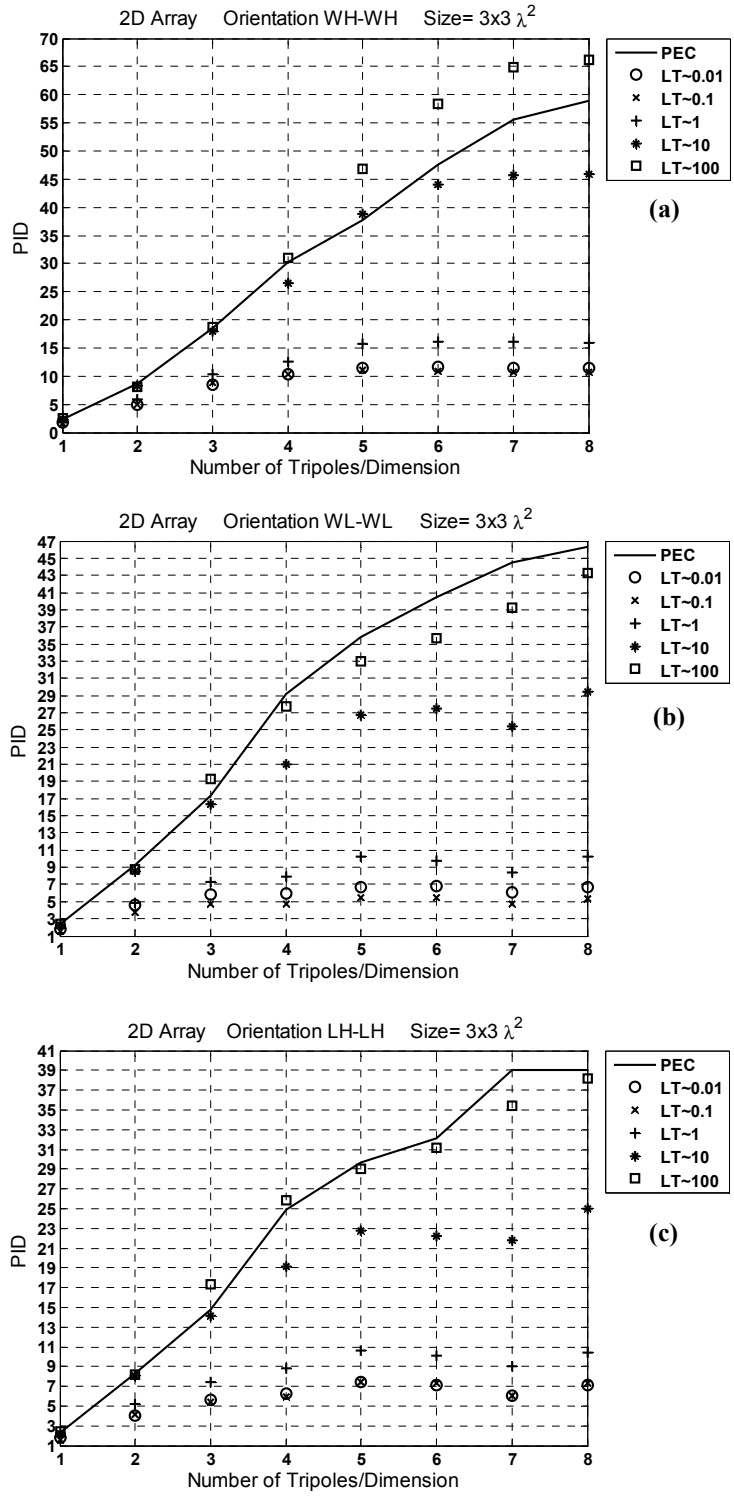

Fig. 5.11

PID of multi-polarization 2D MIMO system of aperture size $3\times3\lambda^2$ in PEC and lossy-walls corridor. The array is oriented as (a) WH-WH (b) WL-WL (c) LH-LH.

Finally, we show the PID results for 3D cubic arrays (sizes $1.5\times1.5\times1.5\lambda^3$ and $3\times3\times3\lambda^3$) in Fig. 5.12. The tripole elements are uniformly deployed over the W- and H-axes and we fix the number of tripoles over the L-axis to the optimum 1D number of 3 and 5 for the small and large array cube, respectively. The computational burden in this tripole 3D array sampling is tremendously heavy and can reach up to 87 hours per simulation on a 1.5 GHz processor with 8 GB RAM. In fact, the memory requirement of the simulation is modest; however, the processor speed requirement is voracious. We only simulated up to 7 tripoles per W- and H- array edge (147 and 245 tripoles for the small and large cube, repectively) for the lossy-walls cases. For the IRT simulations, we use 10^4 and 2000 rays for the small and large array cube, respectively.

Lots of information can be obtained from Fig. 5.7-12. We observe that the PID values indeed saturates after a certain number of tripoles is reached within the aperture. This optimum sampling number depends on the orientation and the environment as pointed out before in [PBT05, LM06]. The PEC corridor is multipath rich and the maximum element separation agrees with the $\frac{\lambda}{2}$ and λ spacing for the 1D broadside and endfire array, repectively.

In the lossy-wall corridor of small LT, the effective spatial bandwidth is reduced because of the power loss suffered by the rays of high-order reflection (mostly through transmission through the walls). Such bandwidth reduction leads to a larger spacing between the optimum samples and a reduced PID value. Also, as pointed out in chapter 3, we notice that for the reflective walls scenarios ($\mathrm{LT} \sim 10^2$), the PID results of the IRT simulation are approaching those obtained through rigorous modal solution in the PEC open waveguide. The possible reasons for the slight discrepancy were reported in chapter 3.

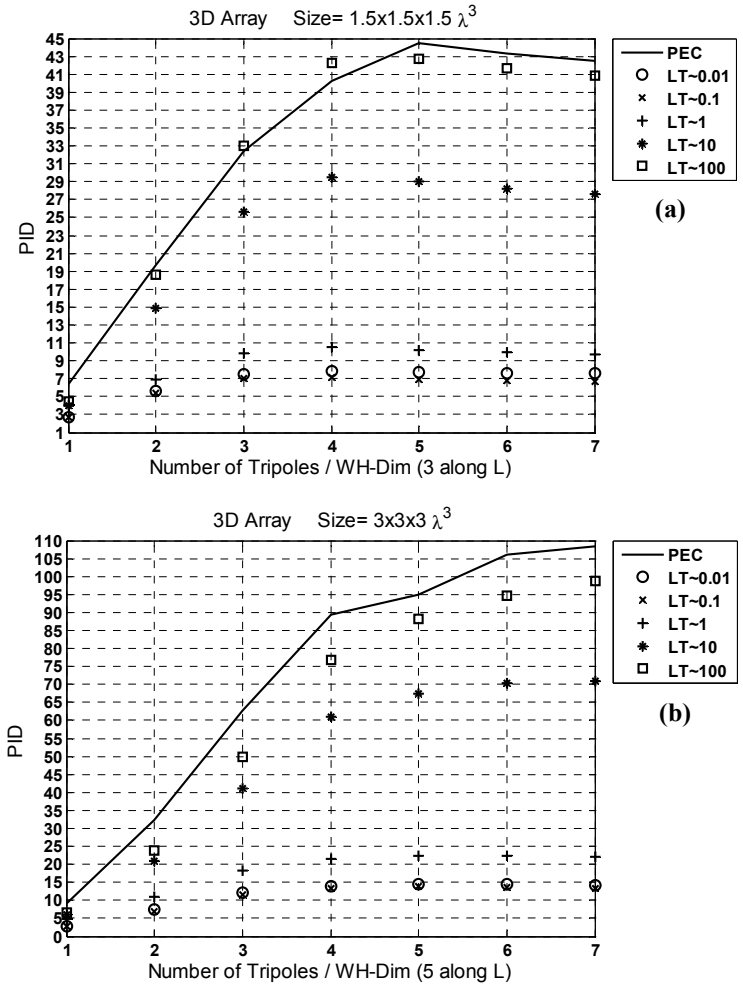

Fig. 5.12

PID of multi-polarization 3D MIMO system in PEC and lossy-walls corridor. Aperture size: (a) $1.5\times1.5\times1.5\lambda^3$ **(b)** $3\times3\times3\lambda^3$**.**

The PID value itself sheds some light on the multi-polarization impact when combined with the spatial diversity under the deterministic Maxwellian framework, which was overlooked in the statistical modeling using scalar isotropic elements (sub-section 5.2.3). In order to clarify this point, we repeated the simulations with hexapole array elements in the PEC waveguide for the 1D and 2D arrays. We also performed simulations with electrical uni-polarized point radiators as sampling elements over the array aperture (the 9 uni-

polarization combinations of tripoles at the transmit/receive ends were considered).

The maximum PID value obtained was recorded (rounded to the nearest integer) for hexapole, tripole and unipole sampling elements (the latter maximized over the 9 polarization combinations). We tabulate these results along with those obtained in sub-section 5.2.3 (optimum sampling and statistical PID) using the isotopic scalar samplers for the spherical and hemispherical ROE (according to the array orientation). Tables 5.2-3 show the DOF results for the 1D and 2D arrays scenarios, repectively.

It is evident that there is a discrepancy between the DOF results, evaluated by the scalar isotropic sampler, and those of the unipole point sources. The discrepancy becomes larger as the DOF increases (wider aperture or 2D array). There are 2 independent reasons for such a discrepancy:

1. The unipole pattern is omnidirectional over the broadside plane. However, it exhibits a null in the endfire direction (along its own linear polarization). This is equivalent to reducing the effective spatial bandwidth and hence the DOF.
2. The isotropic sampling was performed only at one end. From (5.10), we have 3 matrices (modeling the transmit, receive and environment) whose minimum PID will determine the upper bound PID of the channel matrix as discussed in (2.8) (matrix product inequality of chapter 2). The environment dimensionality $\mathrm{PID}(\mathbf{A}^{(rt)})$ is very large in the multipath rich PEC corridor, thus the individual transmit and receive dimensionalities will determine the upper bound PID. Since the transmit/receive apertures have the same size and orientation, we get $\mathrm{PID}(\mathbf{H}^{(r)}) \approx \mathrm{PID}(\mathbf{H}^{(t)})$. Consequently, the dimensionality upper bound $\min\{\mathrm{PID}(\mathbf{H}^{(r)}), \mathrm{PID}(\mathbf{H}^{(t)})\}$ becomes loose as pointed out in chapter 2 (see Fig. 2.1). The loose upper bound is more apparent as the PID increases at both ends. On the other hand, if there were a large

discrepancy between PID($\mathbf{H}^{(r)}$) and PID($\mathbf{H}^{(t)}$) (for example different transmit/receive aperture sizes), the PID upper bound would be tighter. The later case could explain the observation in [XJ06] that increasing the array size at one end makes a slight DOF increase up to the strict limit dictated by the other end of smaller aperture size.

We also note the multi-polarization gain in comparison to the unipole sampler. Referring to Table 5.2, the tripole and hexapole samplers in the multipath rich corridor can enhance the unipole PID of a 1D array by up to 3 and 5 times, respectively. For the 2D arrays, Table 5.3 shows that an enhancement factor of up to 2.71 and 3.88 can be achieved by using the tripole and hexapole samplers, respectively. Thus, a larger array aperture is generally better in exploiting the spatial diversity with a unipole sampler. These enhancement factors are consistent with the average values obtained in chapter 4.

Table 5.2 DOF for 1D Arrays (Different Sizes and Orientations) Using Isotropic and Multi-Polarized Samplers

Array length (in λ)	7		3			1.5		
Orientation (Tx and Rx)	W	L	W	L	H	W	L	H
Isotropic Scalar Opt. Sampling (number of samples within aperture)	15	8	7	4	7	4	2	4
Isotropic Scalar PID (Monte-Carlo multi-keyhole model)	15	8	7	4	7	4	3	4
Opt. Number of Elements (Deterministic)	16	8	8	5	8	5	3	5
Max PID Unipole (Deterministic)	10	7	6	4	5	3	3	3
Max PID Tripole (Deterministic)	29	16	15	9	13	9	6	9
Max PID Hexapole (Deterministic)	47	28	25	15	23	15	10	13

Table 5.3 DOF for 2D Square Arrays (Different Sizes and Orientations) Using Isotropic and Multi-Polarized Samplers

Array Edge Size (in λ)	3			1.5		
Orientation (Tx and Rx)	WH	WL	LH	WH	WL	LH
Isotropic Scalar Opt. Sampling (number of samples within aperture)	39	28	28	12	8	8
Isotropic Scalar PID (Monte-Carlo multi-keyhole model)	49	30	30	19	12	12
Opt. Number of Elements (Deterministic)	8×8	8×5	5×8	5×5	5×3	3×5
Max PID Unipole (Deterministic)	28	18	17	11	8	7
Max PID Tripole (Deterministic)	59	48	40	26	21	19
Max PID Hexapole (Deterministic)	82	69	66	35	31	27

5.4 Summary

We investigated in this chapter the effect of the spectral domain ROE on the DOF of multi-antenna systems. We showed the dependence of the ROE on the array orientation and geometry (being 1D, 2D or 3D). We presented the optimum sampling (scalar isotropic) of 1D, 2D and 3D array apertures and compared the number of samples to the PID obtained through Monte-Carlo simulations for given array orientations.

Next we performed deterministic simulations for multi-polarization arrays in a PEC corridor (modal analysis) and lossy-wall corridor (IRT) of different electrical properties. The results show that unipole samplers PID deviates from that of the scalar isotropic samplers, particularly for large DOF. We also showed the enhancement which the multi-polarization samplers can provide in comparison to the unipole ones.

Chapter 6
Conclusion and Future Work

6.1 Contributions

In this dissertation, we have explored the dimensionality (also called DOF, PID or parallel sub-channels performance) that can be supplied by the natural carrier of the wireless signals: the electromagnetic field. Based on the 3D spatial and vectorial nature of the electric and magnetic fields, we have investigated the fundamental upper limit of the number of parallel data channels that can be provided by exploiting all the possible available diversity resources (space, pattern and polarization). Specifically, the contributions of this research are listed as follows:

- A well-defined power-independent dimensionality (PID) metric has been developed in order to measure the parallel sub-channels performance according to the channel singular values. The novel PID metric was compared to some power-dependent metrics in the literature. The merits and properties of the PID have been discussed, in particular its matrix-

size independence and matrix product inequality, which makes it a very suitable measure to quantify the EM-DOF problem at hand.

- The EM ray propagation model was modified to exhaustively include the available multi-polarization and spatial diversity. We also linked it to the recent multi-keyhole model [LL06a, LL06b], which yields a closed-form expression of matrix product rather than an infinite summation of matrices. The multi-keyhole model was shown to be intuitive in evaluating the MIMO dimensionality upper bound, when the array elements have identical pattern/polarization, through the PID matrix product inequality.
- The multi-polarization effect has been thoroughly investigated in deterministic environments, under the Maxwellian framework. In a multipath rich environment, we showed that a hexapole system is almost guaranteed to provide more than 3 DOF, however the claimed 6 DOF have never been achieved. The tripole system was shown to be able to provide up to 3 DOF. Therefore, a clear answer was provided, in deterministic environments, regarding the ability of the dual fields (electric and magnetic) to carry independent information. This is a fundamental link between the electromagnetism and information theory that has not been well explored in the literature to the best of our knowledge.
- The EM-DOF of a finite array size has been studied in a deterministic environment using rigorous modal analysis and approximate ray tracing. We have emphasized the dependence of the spectral domain ROE on the array geometry (being 1D, 2D or 3D) and its orientation. The optimum sampling of 2D and 3D arrays has been carefully examined. We have also reported novel results of the multi-polarization dimensionality gain (compared to uni-polarized elements) when combined with the spatial diversity of the array.

6.2 Future Work

We believe that the framework proposed in this thesis is just the beginning of future ambitious research work. The following areas would be good candidates to expand on the present work:

- In order to find a fundamental PID limit, we have employed the ideal electromagnetic sampler, which is the polarized (electric or magnetic) point source. This choice was motivated by the requirement to exclude the finite length of each element, the field distortion due to the presence of the detector as well as the inter-element mutual coupling effect. Certainly, this choice is too theoretical. An interesting practical problem would be how to implement miniaturized collocated multi-polarized elements, with acceptable matching over the frequency band of operation, while taking the mutual coupling into consideration. Some recent advances in this direction are reported in [KGK+05, RGK+07]. How would the dimensionality of such practical structures compare with the theoretical limit of this work? This is a problem of a chief industrial importance, which targets the minimum number of miniaturized antennas required to exploit all the available dimensionality of the electromagnetic field.
- A major assumption throughout this thesis was the narrow-band operation. This makes the results valid for frequency flat channels at a single operating frequency. Recent interest in multi-antenna systems is directed toward the wide-band operation [e.g. Mol05]. How the dimensionality, including the multi-polarization effect, will be affected in such a case? We expect that a sub-band in the higher temporal-frequency region will make the aperture size electrically wider, thus promising higher DOF over this sub-band. However, the environment electrical properties and the ray propagation are dispersive as well. In other words, each temporal frequency sub-band of operation has its own

ROE and effective spatial bandwidth. This interesting problem is still open for investigations.

- At the electromagnetic modeling level, there is room for lots of new findings. How can one develop an acceptable statistical model of propagation, using multi-polarization systems, while still obeying the rigorous Maxwellian framework? How can such a model be extended to the wide-band systems? This problem is not yet satisfactorily investigated. Some recent work targeted this multi-polarization problem from statistical perspective [SZM+06]. Another topic of interest is the difference between the indoor and outdoor models. The former exploits several propagation mechanisms (transmission, reflection, diffraction), whereas the latter relies heavily on the diffraction and reflections. In this thesis, we deterministically investigated one canonical structure (empty enclosure). How would the outdoor PID results compare to the indoor ones under the Maxwellian framework?
- All the power issues have been overlooked throughout this work, in the intention to only focus on the dimensionality performance. However, through joint dimensionality- and power-adaptive MIMO systems, it is expected that the general performance of the system (evaluated through a global power-dependent measure such as the capacity or BER) would significantly improve. An interesting project would be to implement an adaptive multi-antenna system (adaptive BFN and/or polarization), focusing first on the PID as the optimization parameter and then applying the optimum power assignment at the transmit elements.

Appendix A
Prolate Spheroidal Wave Functions and DOF Evaluation

In this appendix, we review the definitions and relations of the eigen-functions and eigen-values (prolate spheroidal wave functions PSWF) which are relevant to the DOF evaluation of essentially time- temporal_frequency- bandlimited functions. The functions, whose DOF is under investigation, are assumed to be bandlimited having a bandwidth of $2W$ Hz in the frequency domain. They are entire over the time-domain, however, the majority of their energy is "essentially" confined within a time window of T sec.

A.1 PSWF Definitions and Relations

After separating the 3-D scalar wave equation in a prolate spheroidal coordinate system and expressing $u(t)$ as a function of time rather than a spatial coordinate (so as to be consistent with our objective hereafter), the second order eigen value differential equation

$$\frac{d}{dt}(1-t^2)\frac{d}{dt}u(c,t)+(\chi(c)-c^2t^2)u(c,t)=0, \tag{A.1a}$$

which is equivalent to

$$(1-t^2)\frac{d^2u}{dt^2}-2t\frac{du}{dt}+(\chi-c^2t^2)u=0, \tag{A.1b}$$

has bounded solutions (over the entire t) only when $\chi=\chi_n(c)$, where $\chi_n(c)$ takes discrete real positive values [SP61, Sle83]. Under this condition, the *angular* PSWF $S_{0n}(c,t)$ provides one solution set. The other independent solution set is the angular PSWF of the second kind $S_{0n}^{(2)}(c,t)$ [Fla57, AS72].

A useful solution set is the *radial* PSWF $R_{0n}^{(1)}(c,t)$, which is related to the angular PSWF by a real scale factor $k_n(c)$ [SP61, AS72] such that

$$R_{0n}^{(1)}(c,t)=k_n(c)S_{0n}(c,t). \tag{A.2}$$

$R_{0n}^{(1)}(c,t)$ is normalized so that [SP61]

$$R_{0n}^{(1)}(c,t)\xrightarrow[t\to\infty]{}\frac{1}{ct}\cos[ct-(n+1)\pi/2]. \tag{A.3}$$

A.2 Optimum Basis Functions

Consider a function $y(t)$, entire over t, whose Fourier transform $\tilde{y}(f)$ has a bandwidth of $2W$ (i.e. $\tilde{y}(f)=0, |f|>W$), and whose energy is mostly concentrated over a time window T such that

$$\frac{\int_{-T/2}^{T/2}|y(t)|^2\,dt}{\int_{-\infty}^{\infty}|y(t)|^2\,dt}=1-\varepsilon_T^2, \tag{A.4}$$

where ε_T^2 represents the negligible portion of energy outside the time window (tail energy) [LP62].

The problem of how many degrees of freedom (DOF) are available in $y(t)$ can be stated as follows: given only the knowledge of $y(t)$ within the time-window T, what is the minimum number of independent expansion functions (basis functions) required to reconstruct $y(t)$ subject to an error (over the entire time-domain) which is dependent on the neglected tail energy ε_T^2? The aforementioned problem can be divided into 3 questions:

1. What are the optimum basis functions (in the sense of their ability to best concentrate their energy within and being orthogonal over $|t| < T/2$ [Sle83])?
2. How many of them do we need?
3. What is the greatest lower bound (over all expansion coefficients) of the reconstruction error in terms of ε_T^2?

These questions were answered in the celebrated paper of Landau and Pollak [LP62]. The optimum basis functions are a scaled version of the PSWF's, where $\lfloor 2WT + 1 \rfloor$ such functions ($\lfloor x \rfloor$ is the largest integer $\leq x$) are needed to express $y(t)$ such that the upper bound of the reconstruction square error is $12\varepsilon_T^2$.

The above result is formally stated as [LP62]

$$\int_{-\infty}^{\infty} |y(t) - \sum_{n=0}^{\lfloor 2WT \rfloor} a_n \psi_n(c,t)|^2 \, dt < 12\varepsilon_T^2, \tag{A.5}$$

where [SP61]

$$c = \pi WT \tag{A.6}$$

$$\lambda_n(c) = 2WT \left(R_{0n}^{(1)}(c,1)\right)^2 \tag{A.7}$$

$$\psi_n(c,t) = \sqrt{\lambda_n(c)} \frac{S_{0n}\left(c, \frac{t}{T/2}\right)}{\sqrt{\int_{-T/2}^{T/2} S_{0n}^2\left(c, \frac{t}{T/2}\right) dt}}. \tag{A.8}$$

The important properties of $\{\psi_n(c,t)\}$ and $\{\lambda_n(c)\}$ are listed in the next section.

A.3 Properties of the Optimum Basis Functions

We define the following useful functions and operators:

- $\Pi(t) = \begin{cases} 1 & |t| < \frac{1}{2} \\ 0 & |t| > \frac{1}{2} \end{cases}$: Pulse of unit height and unit area centered at the origin.
- $\text{sinc}(t) = \frac{\sin \pi t}{\pi t}$: Nyquist sampling function (also called the cardinal function [PM62]).
- $\underset{t \to t}{D_T}\{y(t)\} \equiv y(t)\Pi\left(\frac{t}{T}\right)$: Time truncation of width T sec centered at the origin.
- $\underset{t \to f}{F}\{\bullet\}$ and $\underset{f \to t}{F^{-1}}\{\bullet\}$: Fourier and inverse Fourier transform, respectively.
- $\underset{t \to t}{B_{2W}}\{\bullet\} \equiv \underset{f \to t}{F^{-1}} \underset{f \to f}{D_{2W}} \underset{t \to f}{F}\{\bullet\}$: Convolution with an ideal low-pass filter of band-width $2W$ Hz.
- $\underset{t \to t}{C_A}\{y(t)\} \equiv y(At)$: Compression by a factor A.
- $\langle y_1, y_2 \rangle \equiv \int_{-\infty}^{\infty} y_1(t) y_2^*(t) dt$: the inner product of $y_1(t)$ and $y_2(t)$.

Next, we present the properties of $\{\psi_n(c,t)\}$ and $\{\lambda_n(c)\}$.

A.3.1 Bandlimitedness and Double-Orthogonality

$\{\psi_n(c,t)\}$ are band-limited in the frequency domain (their Fourier transform $\{\tilde{\psi}_n(c,f)\}$ has a bandwidth of $2W$ Hz). In the time domain, they possess a very unique property of being orthogonal over 2 different intervals [SP61]:

orthonormal over the real line: $\langle \psi_i , \psi_j \rangle = \delta_{ij}$ (A.9)

orthogonal over $|t| \le T/2$: $\langle D_T \psi_i , D_T \psi_j \rangle = \lambda_i \delta_{ij}$, (A.10)

where δ_{ij} is the Kronecker delta. Besides, $\{\psi_n(c,t)\}$ and $\{D_T \psi_n(c,t)\}$ are respectively complete in the 2 spaces of square-integrable functions spanned by: 1) the band-limited functions of bandwidth $2W$ Hz and 2) the time domain T-truncated functions $D_T y(t)$. Consequently, (A.9) can be used to expand the band-limited square-integrable function $y(t)$ yielding

$$y(t) = \sum_{n=0}^{\infty} \langle y , \psi_n \rangle \psi_n(c,t) . \quad (A.11)$$

Similarly, we can expand $y(t)$ using (A.10)

$$y(t) = \sum_{n=0}^{\infty} \frac{\langle D_T y , D_T \psi_n \rangle}{\lambda_n(c)} \psi_n(c,t) . \quad (A.12)$$

We point out that the expansion coefficients in (A.11) require the full knowledge of $y(t)$ over the entire t. More interestingly in (A.12), we can theoretically extrapolate $y(t)$ over the entire t given only the accurate values of $y(t)$ over $|t| \le T/2$ [SP61].

We note form (A.10) that $\lambda_n(c)$ is the fractional energy of $\psi_n(c,t)$ within $|t| \le T/2$ and is always a real positive number < 1. $\{\lambda_n(c)\}$ are indexed such that their values are in a decreasing order $1 > \lambda_0 > \lambda_1 > \lambda_2 > \cdots$ and correspond to the increasingly-ordered $\chi_0 < \chi_1 < \chi_2 < \cdots$ in (A.1) [Sle83].

A.3.2 Eigen Functions of 2 Finite Kernels

The first eigen integral relation of $\psi_n(c,t)$, in operator notation, is [SP61, LP62]

$$B_{2W} D_T \{\psi_n(c,t)\} = \lambda_n(c) \psi_n(c,t) , \quad (A.13a)$$

which is equivalent to the convolution

$$\int_{-\infty}^{\infty} 2W \text{ sinc } 2W\,(t-s)\Pi\left(\frac{s}{T}\right)\psi_n(c,s)ds = \lambda_n(c)\psi_n(c,t). \qquad \text{(A.13b)}$$

Therefore, $\psi_n(c,t)$ and $\lambda_n(c)$ are the eigen functions and eigen values, respectively, of the *finite shifted sinc* kernel

$K_1(t,s,2W,T) = 2W \text{ sinc } 2W\,(t-s)\Pi\left(\frac{s}{T}\right)$.

The second eigen integral relation of $\psi_n(c,t)$ is linked to the Fourier transform operation [SP61]

$$\int_{-\infty}^{\infty} e^{j2\pi ft}\psi_n(c,\frac{f}{2W/T})\Pi\left(\frac{f}{2W}\right)df = j^n\sqrt{2W/T}\sqrt{\lambda_n(c)}\psi_n(c,t), \qquad \text{(A.14)}$$

which, after some manipulations, can be expressed as

$$\int_{-\infty}^{\infty} e^{-j2\pi f\frac{2W}{T}t}\Pi\left(\frac{t}{T}\right)\psi_n(c,t)dt = \frac{(-j)^n}{\sqrt{2W/T}}\sqrt{\lambda_n(c)}\psi_n(c,f), \qquad \text{(A.15a)}$$

or, in operator notation,

$$C_{2W/T}FD_T\{\psi_n(c,t)\} = \frac{(-j)^n}{\sqrt{2W/T}}\sqrt{\lambda_n(c)}\psi_n(c,f). \qquad \text{(A.15b)}$$

Hence, the eigen functions and eigen values of the *finite compressed Fourier transform* kernel $K_2(t,f,2W,T) = e^{-j2\pi f\frac{2W}{T}t}\Pi\left(\frac{t}{T}\right)$ are

$\psi_n(c,t)$ and $\frac{(-j)^n}{\sqrt{2W/T}}\sqrt{\lambda_n(c)}$, respectively.

A.3.3 Further Properties

$S_{0n}(c,t)$ is even/odd (with respect to t) when n is even/odd [SP61] and accordingly

$$\psi_n(c,-t) = (-1)^n\psi_n(c,t). \qquad \text{(A.16)}$$

Also, $\psi_n(c,t)$ has exactly n zeros within $|t| \le T/2$.

Using the orthonormality property, the Fourier transform kernel $e^{-i\,2\pi ft}$ can be expanded using $\{\psi_n(c,t)\}$ yielding

$$e^{-i\,2\pi ft} = \sum_{n=0}^{\infty} \psi_n(c,t)\tilde{\psi}_n(c,f) \qquad \text{all } t\,; |f| \le W \ . \tag{A.17}$$

Similarly, using the band-limitedness of $\tilde{\psi}_n(c,f)$, one can show that $2W$ sinc $2W(t-s)$ can be expanded as [LP62]

$$2W \text{ sinc } 2W(t-s) = \sum_{n=0}^{\infty} \psi_n(c,t)\psi_n(c,s) \qquad \text{all } t,s \ . \tag{A.18}$$

Setting $t = s$ in (A.18), we get

$$\sum_{n=0}^{\infty} \psi_n{}^2(c,t) = 2W \qquad \text{every } t \ . \tag{A.19}$$

Finally, integrating both sides of (A.19) $\int_{-T/2}^{T/2} (\bullet)dt$ and using (A.10) yield [LP62]

$$\sum_{n=0}^{\infty} \lambda_n(c) = 2WT \qquad \text{every } c \ , \tag{A.20}$$

which means that the summation of all the confined energy fraction of $\psi_n(c,t)$ within $|t| \le T/2$ yield the DOF of $y(t)$ (i.e. its Shannon number [GG73]).

In fact, $\lambda_n(c)$ has a step-like distribution: for $n \ll 2WT$, most of $\lambda_n(c)$ are close to unity whereas for $n \gg 2WT$, most of $\lambda_n(c)$ are close to zero. The interval of transition from 1 to 0, around $n \sim 2WT$, grows as $\log(c)$ [LP62, Sle83]. For large $2WT$, a useful asymptotic approximation of $\lambda_n(c)$ was reported [Sle65, Sle83]

$$\lim_{2WT\to\infty} \lambda_n = \frac{1}{1+e^{\pi b}} \qquad n = \left\lfloor 2WT + \frac{b}{\pi}\log(\pi WT) \right\rfloor, \tag{A.21}$$

where b can take positive, negative or zero value.

Similarly, for large $2WT$, due to the step-like behavior of $\{\lambda_n(c)\}$ and the transition from approximately unity to zero values, we expect that

$$\sum_{n=0}^{\infty} \lambda_n{}^k(c) \xrightarrow[c\to\infty]{} 2WT \qquad k > 0, \tag{A.22}$$

where the approaching speed is governed by k . For $k = 1$, the identity (A.20) holds for all c .

Appendix B
Multi-Polarization Excitation in PEC Rectangular Structures: Modal Analysis

This appendix includes the modal solution of the field excited by an infinitesimal dipole (also known as point source or Hertzian dipole) in a perfect electric conductor (PEC) rectangular environment. We show the solution for a rectangular cavity and for a rectangular waveguide as a response to multi-polarized electrical excitation. The time convention employed for the harmonic field is $e^{j\omega t}$ and consequently, e^{-jkr} denotes an outwardly propagating wave.

B.1 PEC Rectangular Cavity

The PEC rectangular cavity has dimensions of (X, Y, Z) along the x, y and z axis, respectively. The infinitesimal dipole is z-directed and located at (x_0, y_0, z_0), as shown in Fig. B.1, and has unit current density. In such configuration (TM^Z), the electric vector potential $\overline{F}$ may be chosen to be null and the z-component of the magnetic vector potential $\overline{A}$ is sufficient to

determine the field solution [Str41, Bal89, Col90, Eom04]. Therefore, we have one non-homogeneous Helmholz scalar equation

$$(\nabla^2 + k_0{}^2)A_z = -\mu_0 \delta(x - x_0)\delta(y - y_0)\delta(z - z_0), \tag{B.1}$$

where k_0 and μ_0 are the free space wave number and permeability, respectively. The boundary conditions (BC) are the vanishing tangential electric field at the PEC boundaries i.e. at $x = \{0, X\}$; $y = \{0, Y\}$; $z = \{0, Z\}$.

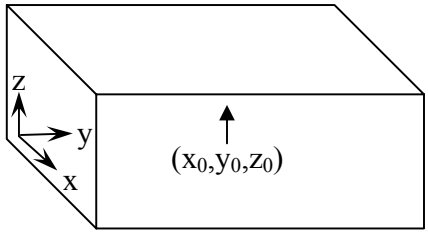

Fig. B.1 Z-directed infinitesimal dipole in a rectangular structure

The solution is based on eigen function expansion [Col90, Eom04]. We choose the following orthonormal eigen functions, which will satisfy the BC,

$$\psi_{mnp}(x, y, z) = \sqrt{\frac{2}{X}\frac{2}{Y}\frac{2}{Z}\varepsilon_p}\,\sin(\frac{m\pi}{X}x)\sin(\frac{n\pi}{Y}y)\cos(\frac{p\pi}{Z}z), \tag{B.2}$$

where the Neumann factor ε_p is given by $\varepsilon_p = \begin{cases} 0.5 & p = 0 \\ 1 & p \neq 0 \end{cases}$.

We expand A_z and $\delta(x-x_0)\delta(y-y_0)\delta(z-z_0)$ in (B.1) using $\psi_{mnp}(x,y,z)$ to obtain

$$A_z = \sum_0^\infty \sum_0^\infty \sum_0^\infty a_{mnp}(x_0, y_0, z_0)\psi_{mnp}(x, y, z) \tag{B.3}$$

$$\delta(x-x_0)\delta(y-y_0)\delta(z-z_0) = \sum_0^\infty \sum_0^\infty \sum_0^\infty \psi_{mnp}(x_0, y_0, z_0)\psi_{mnp}(x, y, z). \tag{B.4}$$

Substituting (B.3-4) in (B.1) and applying mode-matching, we get

$$a_{mnp}(x_0, y_0, z_0) = -\mu_0 \frac{\psi_{mnp}(x_0, y_0, z_0)}{k_0{}^2 - (\frac{m\pi}{X})^2 - (\frac{n\pi}{Y})^2 - (\frac{p\pi}{Z})^2}. \tag{B.5}$$

Substituting (B.5) in (B.3) we get

$$A_z = -\mu_0 \sum_0^\infty \sum_0^\infty \sum_0^\infty \frac{\psi_{mnp}(x_0, y_0, z_0)\psi_{mnp}(x, y, z)}{k_0^2 - (\frac{m\pi}{X})^2 - (\frac{n\pi}{Y})^2 - (\frac{p\pi}{Z})^2}. \tag{B.6}$$

In order to derive the field components from A_z, we have

$$\overline{H} = \frac{1}{\mu_0} \nabla \times \overline{A}, \tag{B.7}$$

then, in a source free region, $\overline{E}$ can be obtained from the second curl Maxwell's equation [Bal89]

$$\overline{E} = \frac{1}{j\omega\varepsilon_0} \nabla \times \overline{H}. \tag{B.8}$$

Both (B.7) and (B.8) are expanded, in cartesian coordinates, into the following field components

$$\begin{aligned} H_x &= \frac{1}{\mu_0}\frac{\partial A_z}{\partial y} & E_x &= \frac{1}{j\omega\varepsilon_0\mu_0}\frac{\partial^2 A_z}{\partial z \partial x} \\ H_y &= -\frac{1}{\mu_0}\frac{\partial A_z}{\partial x} & E_y &= \frac{1}{j\omega\varepsilon\mu_0}\frac{\partial^2 A_z}{\partial z \partial y} \\ H_z &= 0 & E_z &= \frac{-1}{j\omega\varepsilon_0\mu_0}\left(\frac{\partial^2 A_z}{\partial x^2} + \frac{\partial^2 A_z}{\partial y^2}\right) \end{aligned} \tag{B.9}$$

Finally, from (B.6) and (B.9), we get the field solution of the problem

$$H_x = -\frac{8}{XYZ} \sum_0^\infty \sum_0^\infty \sum_0^\infty \varepsilon_p \frac{n\pi}{Y} \frac{\sin(\frac{m\pi}{X}x_0)\sin(\frac{n\pi}{Y}y_0)\cos(\frac{p\pi}{Z}z_0)\sin(\frac{m\pi}{X}x)\cos(\frac{n\pi}{Y}y)\cos(\frac{p\pi}{Z}z)}{k_0^2 - (\frac{m\pi}{X})^2 - (\frac{n\pi}{Y})^2 - (\frac{p\pi}{Z})^2} \tag{B.10a}$$

$$H_y = \frac{8}{XYZ} \sum_0^\infty \sum_0^\infty \sum_0^\infty \varepsilon_p \frac{m\pi}{X} \frac{\sin(\frac{m\pi}{X}x_0)\sin(\frac{n\pi}{Y}y_0)\cos(\frac{p\pi}{Z}z_0)\cos(\frac{m\pi}{X}x)\sin(\frac{n\pi}{Y}y)\cos(\frac{p\pi}{Z}z)}{k_0^2 - (\frac{m\pi}{X})^2 - (\frac{n\pi}{Y})^2 - (\frac{p\pi}{Z})^2} \tag{B.10b}$$

$$H_z = 0 \tag{B.10c}$$

$$E_x = \frac{1}{j\omega\varepsilon_0} 8Y \left(\frac{\pi}{XYZ}\right)^2 \sum_0^\infty \sum_0^\infty \sum_0^\infty \varepsilon_p mp \frac{\sin(\frac{m\pi}{X}x_0)\sin(\frac{n\pi}{Y}y_0)\cos(\frac{p\pi}{Z}z_0)\cos(\frac{m\pi}{X}x)\sin(\frac{n\pi}{Y}y)\sin(\frac{p\pi}{Z}z)}{k_0^2 - (\frac{m\pi}{X})^2 - (\frac{n\pi}{Y})^2 - (\frac{p\pi}{Z})^2} \quad \text{(B.10d)}$$

$$E_y = \frac{1}{j\omega\varepsilon_0} 8X \left(\frac{\pi}{XYZ}\right)^2 \sum_0^\infty \sum_0^\infty \sum_0^\infty \varepsilon_p np \frac{\sin(\frac{m\pi}{X}x_0)\sin(\frac{n\pi}{Y}y_0)\cos(\frac{p\pi}{Z}z_0)\sin(\frac{m\pi}{X}x)\cos(\frac{n\pi}{Y}y)\sin(\frac{p\pi}{Z}z)}{k_0^2 - (\frac{m\pi}{X})^2 - (\frac{n\pi}{Y})^2 - (\frac{p\pi}{Z})^2} \quad \text{(B.10e)}$$

$$E_z = -\frac{1}{j\omega\varepsilon_0} \frac{8\pi^2}{XYZ} \sum_0^\infty \sum_0^\infty \sum_0^\infty \varepsilon_p \left[\left(\frac{m}{X}\right)^2 + \left(\frac{n}{Y}\right)^2\right] \frac{\sin(\frac{m\pi}{X}x_0)\sin(\frac{n\pi}{Y}y_0)\cos(\frac{p\pi}{Z}z_0)\sin(\frac{m\pi}{X}x)\sin(\frac{n\pi}{Y}y)\cos(\frac{p\pi}{Z}z)}{k_0^2 - (\frac{m\pi}{X})^2 - (\frac{n\pi}{Y})^2 - (\frac{p\pi}{Z})^2} \quad \text{(B.10f)}$$

where ε_0 is the permittivity of the free space.

For excitation with an x- or y-polarized source, the field solution is similar to (B.10) with simple coordinate transformation. From (B.10), one can clearly see that there is no real power propagation since $\frac{1}{2}\mathrm{Re}\{\overline{E} \times \overline{H}^*\} = 0$. This result should not be surprising because the radiator (infinitesimal dipole) is completely surrounded by a PEC enclosure and thus all the power is reflected back to the source. Both the evanescent nature of the field and the difficult convergence of (B.10) explain why we do not use this PEC enclosure in our simulations in spite of being a super multipath-rich environment [LM06].

B.2 PEC Rectangular Waveguide

In this section we present the field solution in a PEC waveguide excited by an infinitesimal dipole. We assume that the waveguide propagation direction is down the y-axis and the waveguide cross-section dimensions along the x- and z-axis are (X, Z) respectively as depicted in Fig. B.1. The infinitesimal dipole is located at (x_0, y_0, z_0)

B.2.1 Transverse Source

We assume that the infinitesimal source is z-polarized. For an x-polarized source, the solution needs straightforward coordinate transformation. The non-

homogeneous Helmholz scalar equation is exactly the same as (B.1) (TM^Z). We have PEC boundaries at $x = \{0, X\}$; $z = \{0, Z\}$ and we require that the field components vanish at $y \to \pm\infty$ (radiation BC). Since the waveguide is open along the y-axis, we expect a continuous spectrum along this direction [Col90, Eom04]. Accordingly, we define the Fourier Transform (FT) pairs

$$\tilde{g}(\eta) = \int_{-\infty}^{\infty} g(y) e^{j\eta y} dy \ . \tag{B.11a}$$

$$g(y) = \frac{1}{2\pi} \int_{-\infty}^{\infty} \tilde{g}(\eta) e^{-j\eta y} d\eta \tag{B.11b}$$

Applying FT over the y-axis on both sides of (B.1) and using (B.11a), we get

$$(\nabla_{xz}^2 - \eta^2 + k_0^2)\tilde{A}_z(\eta, x, z, x_0, y_0, z_0) = -\mu_0 \delta(x - x_0)\delta(z - z_0) e^{j\eta y_0}, \tag{B.12}$$

where $\nabla_{xz}^2 \equiv \frac{\partial^2}{\partial x^2} + \frac{\partial^2}{\partial z^2}$.

Subsequently, as we did in the cavity case, we choose the following orthonormal eigen functions, which will satisfy the BC,

$$\psi_{mp}(x, z) = \sqrt{\frac{2}{X}\frac{2}{Z}\varepsilon_p} \sin(\frac{m\pi}{X}x)\cos(\frac{p\pi}{Z}z), \tag{B.13}$$

and we make the orthonormal expansion similar to section B.1 to obtain

$$\tilde{A}_z(\eta, x, z, x_0, y_0, z_0) = -\mu_0 \sum_{m=0}^{\infty}\sum_{p=0}^{\infty} \psi_{mp}(x_0, z_0)\psi_{mp}(x, z) \frac{e^{j\eta y_0}}{\kappa_{mp}^2 - \eta^2}, \tag{B.14}$$

where

$$\kappa_{mp}^2 = k_0^2 - (\frac{m\pi}{X})^2 - (\frac{p\pi}{Z})^2. \tag{B.15}$$

Then, we apply the inverse FT (B.11b) on (B.14) to obtain $A_z(x, y, z, x_0, y_0, z_0)$

$$A_z = -\frac{\mu_0}{2\pi} \sum_{m=0}^{\infty}\sum_{p=0}^{\infty} \psi_{mp}(x_0, z_0)\psi_{mp}(x, z) \underbrace{\int_{-\infty}^{\infty} \frac{e^{-j\eta(y - y_0)}}{\kappa_{mp}^2 - \eta^2} d\eta}_{I},$$

where the integral I is evaluated using the residue theory. We point out that both k and κ_{mp} have a small negative imaginary parts accounting for losses (satisfying

the vanishing fields at $y \to \pm\infty$). We use the residue theory for the contours shown in Fig. B.2 such that for $y > y_0$, we use C_0 and C_1 and for $y < y_0$, we use C_0 and C_2. Therefore, $I = -j2\pi \dfrac{e^{-j\kappa_{mp}|y-y_0|}}{2\kappa_{mp}}$ yielding

$$A_z = j\mu_0 \sum_{m=0}^{\infty}\sum_{p=0}^{\infty} \psi_{mp}(x_0, z_0)\psi_{mp}(x, z)\frac{e^{-j\kappa_{mp}|y-y_0|}}{2\kappa_{mp}}, \tag{B.16}$$

where

$$\kappa_{mp} = \begin{cases} \sqrt{k_0^2 - (\frac{m\pi}{X})^2 - (\frac{p\pi}{Z})^2} & k_0^2 > (\frac{m\pi}{X})^2 + (\frac{p\pi}{Z})^2 \\ -j\sqrt{(\frac{m\pi}{X})^2 + (\frac{p\pi}{Z})^2 - k_0^2} & k_0^2 < (\frac{m\pi}{X})^2 + (\frac{p\pi}{Z})^2 \end{cases}. \tag{B.17}$$

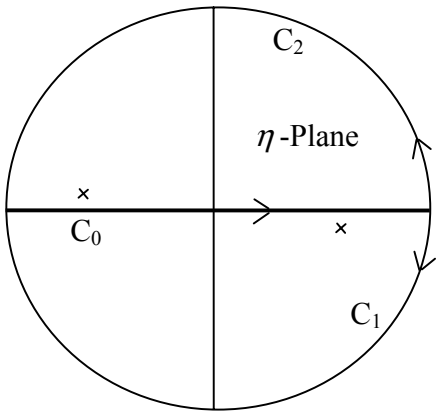

Fig. B.2 Complex η-plane and integration contours

The field solution is then found from (B.16) and (B.9) yielding

$$H_x = \mathrm{sgn}(y-y_0)\frac{2}{XZ}\sum_{m=0}^{\infty}\sum_{p=0}^{\infty}\varepsilon_p \sin(\frac{m\pi}{X}x_0)\sin(\frac{m\pi}{X}x)\cos(\frac{p\pi}{Z}z_0)\cos(\frac{p\pi}{Z}z)e^{-j\kappa_{mp}|y-y_0|} \tag{B.18a}$$

$$H_y = -j\frac{2}{XZ}\sum_{m=0}^{\infty}\sum_{p=0}^{\infty}\varepsilon_p \frac{m\pi}{X}\sin(\frac{m\pi}{X}x_0)\cos(\frac{m\pi}{X}x)\cos(\frac{p\pi}{Z}z_0)\cos(\frac{p\pi}{Z}z)\frac{e^{-j\kappa_{mp}|y-y_0|}}{\kappa_{mp}} \tag{B.18b}$$

$$H_z = 0 \tag{B.18c}$$

$$E_x = -\frac{1}{\omega\varepsilon_0}\frac{2}{XZ}\sum_{m=0}^{\infty}\sum_{p=0}^{\infty}\varepsilon_p \frac{m\pi}{X}\frac{p\pi}{Z}\sin(\frac{m\pi}{X}x_0)\cos(\frac{m\pi}{X}x)\cos(\frac{p\pi}{Z}z_0)\sin(\frac{p\pi}{Z}z)\frac{e^{-j\kappa_{mp}|y-y_0|}}{\kappa_{mp}} \quad \text{(B.18d)}$$

$$E_y = j\,\mathrm{sgn}(y-y_0)\frac{1}{\omega\varepsilon_0}\frac{2}{XZ}\sum_{m=0}^{\infty}\sum_{p=0}^{\infty}\varepsilon_p \frac{p\pi}{Z}\sin(\frac{m\pi}{X}x_0)\sin(\frac{m\pi}{X}x)\cos(\frac{p\pi}{Z}z_0)\sin(\frac{p\pi}{Z}z)e^{-j\kappa_{mp}|y-y_0|} \quad \text{(B.18e)}$$

$$E_z = \frac{1}{\omega\varepsilon_0}\frac{2}{XZ}\sum_{m=0}^{\infty}\sum_{p=0}^{\infty}\varepsilon_p \sin(\frac{m\pi}{X}x_0)\sin(\frac{m\pi}{X}x)\cos(\frac{p\pi}{Z}z_0)\cos(\frac{p\pi}{Z}z)\frac{e^{-j\kappa_{mp}|y-y_0|}}{\kappa_{mp}}\left[k_0{}^2-(\frac{p\pi}{Z})^2\right] \quad \text{(B.18f)}$$

In (B.18), $\mathrm{sgn}(\xi)=\begin{cases}1 & \xi>0\\ -1 & \xi<0\end{cases}$. We assume that $|y-y_0|$ is large enough (compared to the wavelength) such that the evanescent mode effect is negligible in the simulations. Thus, according to the operation frequency, only the propagating modes of (B.18) are considered and there is no convergence problem as long as we are far enough from the source. We note from $\frac{1}{2}\mathrm{Re}\{\overline{E}\times\overline{H}^*\}$ in (B.18) that there is a real power transfer along the propagation direction (y-axis) without any decay (lossless walls). We also note that the solution is space-invariant with respect to the y-axis i.e. function of $(y-y_0)$.

For an x-polarized infinitesimal excitation dipole, coordinate transformation readily gives the field solution

$$H_x = 0 \quad \text{(B.19a)}$$

$$H_y = j\frac{2}{XZ}\sum_{m=0}^{\infty}\sum_{p=0}^{\infty}\varepsilon_m \frac{p\pi}{Z}\cos(\frac{m\pi}{X}x_0)\cos(\frac{m\pi}{X}x)\sin(\frac{p\pi}{Z}z_0)\cos(\frac{p\pi}{Z}z)\frac{e^{-j\kappa_{mp}|y-y_0|}}{\kappa_{mp}} \quad \text{(B.19b)}$$

$$H_z = -\mathrm{sgn}(y-y_0)\frac{2}{XZ}\sum_{m=0}^{\infty}\sum_{p=0}^{\infty}\varepsilon_m \cos(\frac{m\pi}{X}x_0)\cos(\frac{m\pi}{X}x)\sin(\frac{p\pi}{Z}z_0)\sin(\frac{p\pi}{Z}z)e^{-j\kappa_{mp}|y-y_0|} \quad \text{(B.19c)}$$

$$E_x = \frac{1}{\omega\varepsilon_0}\frac{2}{XZ}\sum_{m=0}^{\infty}\sum_{p=0}^{\infty}\varepsilon_m \cos(\frac{m\pi}{X}x_0)\cos(\frac{m\pi}{X}x)\sin(\frac{p\pi}{Z}z_0)\sin(\frac{p\pi}{Z}z)\frac{e^{-j\kappa_{mp}|y-y_0|}}{\kappa_{mp}}\left[k_0{}^2-(\frac{m\pi}{X})^2\right] \quad \text{(B.19d)}$$

$$E_y = j\,\mathrm{sgn}(y-y_0)\frac{1}{\omega\varepsilon_0}\frac{2}{XZ}\sum_{m=0}^{\infty}\sum_{p=0}^{\infty}\varepsilon_m \frac{m\pi}{X}\cos(\frac{m\pi}{X}x_0)\sin(\frac{m\pi}{X}x)\sin(\frac{p\pi}{Z}z_0)\sin(\frac{p\pi}{Z}z)e^{-j\kappa_{mp}|y-y_0|} \quad \text{(B.19e)}$$

$$E_z = -\frac{1}{\omega\varepsilon_0}\frac{2}{XZ}\sum_{m=0}^{\infty}\sum_{p=0}^{\infty}\varepsilon_m \frac{m\pi}{X}\frac{p\pi}{Z}\cos(\frac{m\pi}{X}x_0)\sin(\frac{m\pi}{X}x)\sin(\frac{p\pi}{Z}z_0)\cos(\frac{p\pi}{Z}z)\frac{e^{-j\kappa_{mp}|y-y_0|}}{\kappa_{mp}} \quad \text{(B.19f)}$$

B.2.2 Longitudinal Source

We conclude this appendix by providing the field solution in a PEC waveguide, which is excited by an infinitesimal y-polarized source (along the direction of propagation). The same procedure in sub-section B.2.1 is repeated with the non-homogeneous Helmholz scalar equation (TM^Y mode)

$$(\nabla^2 + k_0{}^2)A_y = -\mu_0\delta(x - x_0)\delta(y - y_0)\delta(z - z_0) \tag{B.20}$$

under the same PEC-BC at $x = \{0, X\}$; $z = \{0, Z\}$ and the requirement that the field components vanish at $y \to \pm\infty$.

Accordingly, we apply FT along the y-axis and we choose the following orthonormal eigen functions, which will satisfy the BC,

$$\psi_{mp}(x, z) = \sqrt{\frac{2}{X}\frac{2}{Z}}\sin(\frac{m\pi}{X}x)\sin(\frac{p\pi}{Z}z). \tag{B.21}$$

After repeating the same steps of sub-section B.2.1, we get the following field solution

$$H_x = -j\frac{2}{XZ}\sum_{m=0}^{\infty}\sum_{p=0}^{\infty}\frac{p\pi}{Z}\sin(\frac{m\pi}{X}x_0)\sin(\frac{m\pi}{X}x)\sin(\frac{p\pi}{Z}z_0)\cos(\frac{p\pi}{Z}z)\frac{e^{-j\kappa_{mp}|y-y_0|}}{\kappa_{mp}} \tag{B.22a}$$

$$H_y = 0 \tag{B.22b}$$

$$H_z = j\frac{2}{XZ}\sum_{m=0}^{\infty}\sum_{p=0}^{\infty}\frac{m\pi}{X}\sin(\frac{m\pi}{X}x_0)\cos(\frac{m\pi}{X}x)\sin(\frac{p\pi}{Z}z_0)\sin(\frac{p\pi}{Z}z)\frac{e^{-j\kappa_{mp}|y-y_0|}}{\kappa_{mp}} \tag{B.22c}$$

$$E_x = -j\,\mathrm{sgn}(y - y_0)\frac{1}{\omega\varepsilon_0}\frac{2}{XZ}\sum_{m=0}^{\infty}\sum_{p=0}^{\infty}\frac{m\pi}{X}\sin(\frac{m\pi}{X}x_0)\cos(\frac{m\pi}{X}x)\sin(\frac{p\pi}{Z}z_0)\sin(\frac{p\pi}{Z}z)e^{-j\kappa_{mp}|y-y_0|} \tag{B.22d}$$

$$E_y = \frac{1}{\omega\varepsilon_0}\frac{2}{XZ}\sum_{m=0}^{\infty}\sum_{p=0}^{\infty}\left[(\frac{m\pi}{X})^2 + (\frac{p\pi}{Z})^2\right]\sin(\frac{m\pi}{X}x_0)\sin(\frac{m\pi}{X}x)\sin(\frac{p\pi}{Z}z_0)\sin(\frac{p\pi}{Z}z)\frac{e^{-j\kappa_{mp}|y-y_0|}}{\kappa_{mp}} \tag{B.22e}$$

$$E_z = -j\,\mathrm{sgn}(y - y_0)\frac{1}{\omega\varepsilon_0}\frac{2}{XZ}\sum_{m=0}^{\infty}\sum_{p=0}^{\infty}\frac{p\pi}{Z}\sin(\frac{m\pi}{X}x_0)\sin(\frac{m\pi}{X}x)\sin(\frac{p\pi}{Z}z_0)\cos(\frac{p\pi}{Z}z)e^{-j\kappa_{mp}|y-y_0|} \tag{B.22f}$$

Appendix C
Spatial-Frequency Domain of Electromagnetic Fields

In this appendix, we review the spectral domain (spatial frequency) transform of the electromagnetic fields, which is also known as the plane wave expansion [Cle66]. Two useful properties of this transform, governed by the vectorial electromagnetic wave equation, are employed throughout this thesis:

1. The 2 DOF associated with each vectorial spectral component of $\overline{E}$ and $\overline{H}$.
2. The region of existence (ROE) of the 3D spatial-Fourier transform of the electromagnetic fields.

At any source-free point of space, such as where the electromagnetic detector will be installed, the electromagnetic vectorial homogeneous wave equation must be satisfied

$$\nabla^2 \overline{E} + k_0{}^2 \overline{E} = 0 \qquad \text{(C.1a)}$$

$$\nabla^2 \overline{H} + k_0{}^2 \overline{H} = 0, \qquad \text{(C.1b)}$$

where k_0 is the free space wave number and is related to the free space wavelength λ by $k_0 = \frac{2\pi}{\lambda}$. The homogeneous wave equation (C.1) is another form of the 2 source-free curl Maxwell's equations after decoupling $\overline{E}$ and $\overline{H}$.

By applying the 3D spatial Fourier transform on (C.1a), in Cartesian coordinates, we obtain

$$(-k_x{}^2 - k_y{}^2 - k_z{}^2 + k_0{}^2)\overline{\overline{E}}(k_x, k_y, k_z) = 0, \tag{C.2}$$

where the transform vector pairs are related by

$$\overline{\overline{E}}(k_x, k_y, k_z) = \int_{-\infty}^{\infty}\int_{-\infty}^{\infty}\int_{-\infty}^{\infty} \overline{E}(x, y, z) e^{j(k_x x + k_y y + k_z z)} dx dy dz \tag{C.3}$$

$$\overline{E}(x, y, z) = \frac{1}{(2\pi)^3}\int_{-\infty}^{\infty}\int_{-\infty}^{\infty}\int_{-\infty}^{\infty} \overline{\overline{E}}(k_x, k_y, k_z) e^{-j(k_x x + k_y y + k_z z)} dk_x dk_y dk_z \tag{C.4}$$

The kernel in (C.4) represents a plane wave (traveling or evanescent), thus the transform (C.4) can be regarded as a plane wave expansion. There are 2 useful normalizations for the k-domain, namely, the spatial frequency domain [Goo96]

$$(f_x, f_y, f_z) = \frac{1}{2\pi}(k_x, k_y, k_z) \tag{C.5a}$$

yielding

$$\overline{E}(x, y, z) = \int_{-\infty}^{\infty}\int_{-\infty}^{\infty}\int_{-\infty}^{\infty} \overline{\overline{E}}(f_x, f_y, f_z) e^{-j2\pi(f_x x + f_y y + f_z z)} df_x df_y df_z \; ; \tag{C.5b}$$

and the complex direction cosine (also known as the complex unit vector) domain [Cle66]

$$\hat{\mathbf{k}} = \frac{\lambda}{2\pi}(k_x, k_y, k_z) \tag{C.6a}$$

yielding

$$\overline{E}(x, y, z) = \frac{1}{\lambda^3}\int_{-\infty}^{\infty} \overline{\overline{E}}(\hat{\mathbf{k}}) e^{-jk_0 \hat{\mathbf{k}}\cdot\mathbf{r}} d^3\hat{\mathbf{k}}, \tag{C.6b}$$

where $\mathbf{r} = (x, y, z)$.

From (C.2), the values of (k_x, k_y, k_z) are not arbitrary since they must satisfy

$$k_x^2 + k_y^2 + k_z^2 = k_0^2, \tag{C.7}$$

otherwise, $\overline{\overline{E}}$ will vanish over the whole k-domain. Consequently, the ROE of $\overline{\overline{E}}$ is a surface in the 3D k-domain, over which (C.7) is satisfied. In other words, the 3D Fourier transform can be reduced to a 2D one. Typically, we pick a direction (say the positive z-axis), which will become the decay direction of the evanescent plane-wave components in the half-space z>0, and express its corresponding k-component (k_z) in terms of (k_x, k_y) so that

$$k_z = \begin{cases} +\sqrt{k_0^2 - k_x^2 - k_y^2} & k_x^2 + k_y^2 \le k_0^2 \\ -j\sqrt{k_x^2 + k_y^2 - k_0^2} & k_x^2 + k_y^2 > k_0^2 \end{cases}. \tag{C.8}$$

As depicted in Fig. C.1, when k_z is real, the ROE is the upper hemispherical *shell*, each point over which represents a plane-wave component *traveling* in the direction $\hat{\mathbf{k}}$. For negative imaginary k_z, the ROE is the lower semi-hyperboloid *surface* (of one-sheet), each point over which represents an *evanescent* plane-wave component decaying in the positive z-direction at a rate of $e^{-|k_z|z}$. In the evanescent case, the unit vector $\hat{\mathbf{k}}$ is complex such that $\hat{\mathbf{k}} \cdot \hat{\mathbf{k}} = 1$; and its real and imaginary vector components are orthogonal [Cle66]. The ROE intercepts each axis of the k-domain at k_0 (corresponding to $\frac{1}{\lambda}$ and 1 for the f- and $\hat{\mathbf{k}}$-domains, respectively).

The transform ROE above covers only one half-space (z>0). In order to cover the other half-space, there is a symmetrical ROE (hemisphere and semi-hyperboloid in the negative and positive k_z directions, respectively) which accounts for the propagation/evanescence components in the half-space z<0. The propagation spherical shell (the 2 hemispheres) of the k-domain represents the full visible angular spectrum ($\theta \in [0, \pi]$ and $\varphi \in [0, 2\pi]$), which is encountered in closed structures such as cavities. In the far-field region, the

effect of the evanescent components on the semi-hyperboloid surfaces is negligible, hence we focus only on the propagation sphere ROE in practical scenarios.

The 3D inverse Fourier transform (C.4) over the ROE surface is thus equivalent to a 2D one

$$\overline{E}(x,y,z)=\frac{1}{(2\pi)^2}\int_{-\infty}^{\infty}\int_{-\infty}^{\infty}\overline{\overline{E}}(k_x,k_y)e^{-j(k_x x+k_y y\pm(k_0^2-k_x^2-k_y^2)^{1/2}z)}dk_x dk_y \quad \text{(C.9)}$$

where the upper/lower signs describe the propagation along the positive/negative z-direction, respectively.

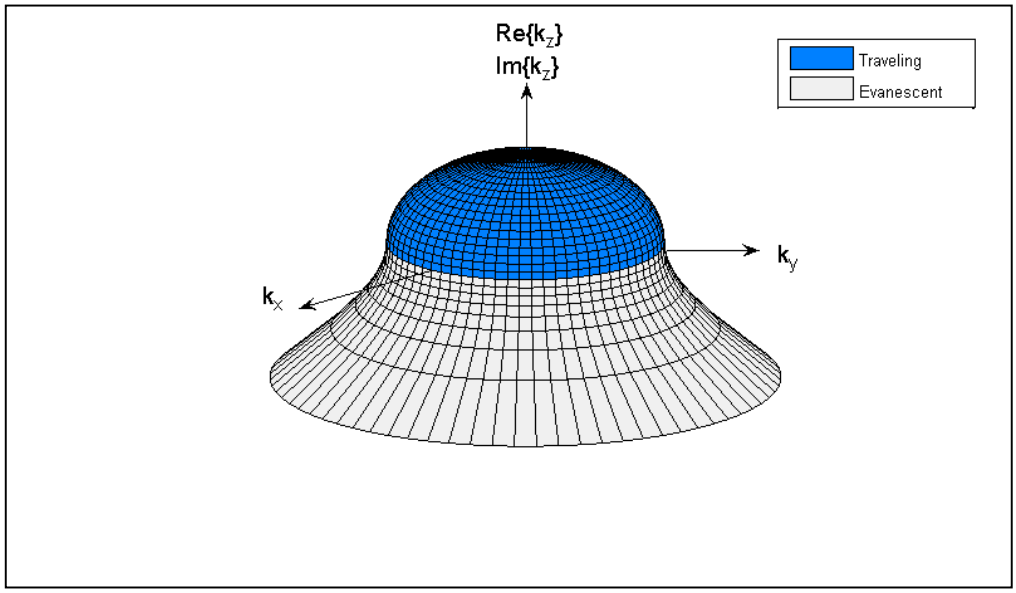

Fig. C.1 Region of existence (ROE) of the electromagnetic fields spectrum in the k-domain for the half-space z>0

Next, we proceed to find the relation between $\hat{\mathbf{k}}$ and the 2 transform vectors $\overline{\overline{E}}$ and $\overline{\overline{H}}$ [Bal97]. In a source-free region, $\nabla\cdot\overline{E}(x,y,z)=0$. Therefore, by applying the divergence operation on (C.6b) and interchanging the differentiation and integration order, we get

$$\int_{-\infty}^{\infty} \nabla \cdot \left(\overline{\overline{E}}(\hat{\mathbf{k}}) e^{-jk_0 \hat{\mathbf{k}} \cdot \mathbf{r}} \right) d^3 \hat{\mathbf{k}} = 0 . \tag{C.10}$$

Using the vector identity $\nabla \cdot (\alpha \overline{A}) = \alpha \nabla \cdot \overline{A} + \overline{A} \cdot \nabla \alpha$ and noting that $\nabla \cdot \overline{\overline{E}}(\hat{\mathbf{k}}) = 0$, (C.10) yields

$$\overline{\overline{E}}(\hat{\mathbf{k}}) \cdot \nabla e^{-jk_0 \hat{\mathbf{k}} \cdot \mathbf{r}} = -jk_0 e^{-jk_0 \hat{\mathbf{k}} \cdot \mathbf{r}} \overline{\overline{E}}(\hat{\mathbf{k}}) \cdot \hat{\mathbf{k}} = 0 , \tag{C.11}$$

that is for real $\hat{\mathbf{k}}$ (traveling waves), $\overline{\overline{E}}(\hat{\mathbf{k}})$ is orthogonal to the direction of propagation. From (C.11), given $\hat{\mathbf{k}}$ and 2 components of $\overline{\overline{E}}(\hat{\mathbf{k}})$, the third component can be readily derived and thus each $\overline{\overline{E}}(\hat{\mathbf{k}})$ has only 2 DOF.

Finally, in order to obtain $\overline{\overline{H}}(\hat{\mathbf{k}})$, we plug (C.6b) in the following Maxwell's equation and we switch the order of the integration and curl operation to get

$$\begin{aligned} \overline{H}(x, y, z) &= -\frac{1}{j\omega\mu_0} \nabla \times \overline{E}(x, y, z) \\ &= -\frac{1}{jk_0\eta_0} \frac{1}{\lambda^3} \int_{-\infty}^{\infty} \nabla \times \left(\overline{\overline{E}}(\hat{\mathbf{k}}) e^{-jk_0 \hat{\mathbf{k}} \cdot \mathbf{r}} \right) d^3 \hat{\mathbf{k}} \end{aligned} , \tag{C.12}$$

where $\eta_0 = 120\pi$ is the free-space impedance. Using the vector identity $\nabla \times (\alpha \overline{A}) = \alpha \nabla \times \overline{A} + \nabla \alpha \times \overline{A}$ and noting that $\nabla \times \overline{\overline{E}}(\hat{\mathbf{k}}) = 0$, (C.12) yields

$$\begin{aligned} \overline{H}(x, y, z) &= \frac{1}{\lambda^3} \int_{-\infty}^{\infty} -\frac{1}{jk_0\eta_0} \nabla e^{-jk_0 \hat{\mathbf{k}} \cdot \mathbf{r}} \times \overline{\overline{E}}(\hat{\mathbf{k}}) d^3 \hat{\mathbf{k}} \\ &= \frac{1}{\lambda^3} \int_{-\infty}^{\infty} \frac{\hat{\mathbf{k}} \times \overline{\overline{E}}(\hat{\mathbf{k}})}{\eta_0} e^{-jk_0 \hat{\mathbf{k}} \cdot \mathbf{r}} d^3 \hat{\mathbf{k}} \\ &\equiv \frac{1}{\lambda^3} \int_{-\infty}^{\infty} \overline{\overline{H}}(\hat{\mathbf{k}}) e^{-jk_0 \hat{\mathbf{k}} \cdot \mathbf{r}} d^3 \hat{\mathbf{k}} \end{aligned} . \tag{C.13}$$

Therefore, $\overline{\overline{H}}(\hat{\mathbf{k}}) = \dfrac{\hat{\mathbf{k}} \times \overline{\overline{E}}(\hat{\mathbf{k}})}{\eta_0}$, confirming that each spatial component is indeed a plane wave (traveling or evanescent). Consequently, for each *individual* component, $\overline{\overline{H}}(\hat{\mathbf{k}})$ does not provide any further DOF since it can be fully known from $\overline{\overline{E}}(\hat{\mathbf{k}})$. However, through the integration of *all* plane-wave components, both $\overline{E}$ and $\overline{H}$ *can* provide higher DOF as discussed in chapter 4.

Bibliography

[AMC01] M. R. Andrews, P. Mitra, and R. deCarvalho, "Tripling the Capacity of Wireless Communications Using Electromagnetic Polarization," *Nature*, vol. 409, pp. 316-318, Jan. 2001.

[AN00] G. Athanasiadou and A. Nix, "A Novel 3-D Indoor Ray-Tracing Propagation Model: the Path Generator and Evaluation of Narrow-Band and Wide-Band Predictions," *IEEE Trans. Vehicular Technology*, vol. 49, pp. 1152-1168, July 2000.

[AS72] M. Abramowitz and I. A. Stegun, *Handbook of Mathematical Functions with Formulas, Graphs, and Mathematical Tables*, Washington, D.C.: U.S. Dept. of Commerce, 1972.

[ATKM03] P. Almers, F. Tufvesson, P. Karlsson, and A. F. Molisch, "The Effect of Horizontal Array Orientation on MIMO Channel Capacity," *IEEE Vehicular Technology Conference*, vol. 1, pp. 34-38, Apr. 2003.

[ATM06] P. Almers, F. Tufvesson, and A. F. Molisch, "Keyhole Effect in MIMO Wireless Channels: Measurements and Theory," *IEEE Trans. Wireless Comm.*, vol. 5, pp. 3596-3604, Dec. 2006.

[Bal89] C. Balanis, *Advanced Engineering Electromagnetics*, John Wiley & Sons, 1989.

[Bal97] C. Balanis, *Antenna Theory Analysis and Design*, John Wiley & Sons, 1997.

[BF87] O. M. Bucci and G. Franceschetti, “On the Spatial Bandwidth of Scattered Fields,” *IEEE Trans. Antennas Propagation*, vol. 35, pp. 1445-1455, Dec. 1987.

[BF89] O. M. Bucci and G. Franceschetti, “On the Degrees of Freedom of Scattered Fields,” *IEEE Trans. Antennas Propagation*, vol. 37, pp. 918-925, July 1989.

[BGS98] O. M. Bucci, C. Gennarelli, and C. Savarese, “Representation of Electromagnetic Fields over Arbitrary Surfaces by a Finite and Nonredundant Number of Samples,” *IEEE Trans. Antennas Propagation*, vol. 46, pp. 351-359, Mar. 1998.

[CFGV02] D. Chizhik, G. J. Foschini, M. J. Gans, and R. A. Valenzuela, "Keyholes, Correlations, and Capacities of Multielement Transmit and Receive Antennas," *IEEE Trans. Wireless Comm.*, vol. 1, pp. 361-368 , Apr. 2002.

[Cle66] P. C. Clemmow, *The Plane Wave Spectrum Representation of Electromagnetic Fields*, Oxford Pergamon Press, 1966.

[Col90] R. E. Collin, *Field Theory of Guided Waves*, John Wiley & Sons, 1990.

[CT91] T. M. Cover and J. A. Thomas, *Elements of Information Theory*, John Wiley & Sons, 1991.

[Eln03] M. Elnaggar, “Electromagnetic Theoretical Capacity Evaluation of MIMO Antenna Systems in Simple Indoor Environments,” M.A.Sc. Thesis, Dept. Electrical and Computer Eng., Univ. Waterloo, ON, 2003.

[Eom04] H. J. Eom, *Electromagnetic Wave Theory for Boundary-Value Problems*, Springer, 2004.

[ESC04a] M. Elnaggar, S. Safavi-Naeini and S. K. Chaudhuri, "Effect of Oversimplifying the Simulated Indoor Propagation on the Deterministic MIMO Capacity," *IEEE Canadian Conference on Electrical and Computer Engineering (CCECE 2004)*, vol. 1, pp. 219-222, Niagara Falls, ON, May 2004.

[ESC04b] M. S. Elnaggar, S. Safavi-Naeini and S. K. Chaudhuri, "Simulation of the Achievable Indoor MIMO Capacity by Using an Adaptive Phased-Array," *IEEE Radio & Wireless Conference (RAWCON 2004)*, pp. 155-158, Atlanta, GA, Sept. 2004.

[ESC05] M. S. Elnaggar, S. Safavi-Naeini and S. K. Chaudhuri, "Site-Specific Indoor MIMO Capacity Using Adaptive Techniques," invited to a special session at *IEEE Antennas and Propagation Society International Symposium*, vol. 3B, pp. 426-429, Washington, D.C., July 2005.

[ESC06a] M. S. Elnaggar, S. Safavi-Naeini and S. K. Chaudhuri, "Site-Specific MIMO Channel Optimization Using Adaptive Polarization," *IEEE Radio and Wireless Symposium (RWS 2006)*, pp. 419-422, San Diego, CA, Jan. 2006.

[ESC06b] M. S. Elnaggar, S. Safavi-Naeini and S. K. Chaudhuri, "A Novel Dimensionality Metric for Multi-Antenna Systems," *Proceedings of Asia-Pacific Microwave Conference (APMC2006)*, Yokohama, Japan, Dec. 2006.

[ESC07a] M. S. Elnaggar, S. Safavi-Naeini and S. K. Chaudhuri, "A Power-Independent Dimensionality Metric for Multi-Antenna Systems," submitted.

[FG98] G. Foschini and M. Gans, "On Limits of Wireless Communications in a Fading Environment When Using Multiple Antennas," *Wireless Personal*

Communications, Kluwer Academic Publishers, vol. 6, no.3, pp. 311-335, Mar. 1998.

[FK06] P. J. S. G. Ferreira and A. Kempf, "Superoscillations: Faster Than the Nyquist Rate," *IEEE Trans. on Signal Processing*, vol. 54, pp. 3732-3740, Oct. 2006.

[Fla57] C. Flammer, *Spheroidal Wave Functions*, Stanford University Press, 1957.

[Fos96] G. Foschini, "Layered Space-Time Architecture for Wireless Communication in a Fading Environment when Using Multi-Element Antennas," *Bell Labs Technical Journal*, pp. 41-59, Autumn 1996.

[Gab61] D. Gabor, "Light and Information," in *Progress in Optics*, ed. E. Wolf, North-Holland, Amsterdam, vol. 1, pp. 109-153, 1961.

[GG73] F. Gori and G. Guattari, "Shannon Number and Degrees of Freedom of an Image," *Opt. Commun.*, vol. 7, pp. 163–165, Feb. 1973.

[Goo96] J. W. Goodman, *Introduction to Fourier Optics*, McGraw-Hill, 1996.

[Har28] R. V. L. Hartley, "Transmission of Information," *Bell System Technical Journal*, vol. 7, pp. 535-564, July 1928.

[Har61] R. F. Harrington, *Time-Harmonic Electromagnetic Fields*, McGraw-Hill, 1961.

[HJ87] R. A. Horn, and C. R. Johnson, *Matrix Analysis*, Cambridge University Press, 1987.

[HJ94] R. A. Horn, and C. R. Johnson, *Topics in Matrix Analysis*, Cambridge University Press, 1994.

[JI05] J. Jeng-Shiann and M.A. Ingram, "Spherical-Wave Model for Short-Range MIMO," *IEEE trans. Comm.*, vol. 53, pp. 1534 – 1541, Sept. 2005.

[JW04] M. A. Jensen and J. W. Wallace, "A Review of Antennas and Propagation for MIMO Wireless Communications," *IEEE Trans. Antennas Propagation*, vol. 52, pp. 2810-2824, Nov. 2004.

[Kem07] Private Communication with Prof. A. Kempf, Dept. of Applied Mathematics, Univ. Waterloo, ON, Canada.

[KGK+05] A. S. Konanur, K. Gosalia, S. H. Krishnamurthy, B. Hughes, and G. Lazzi, "Increasing Wireless Channel Capacity through MIMO Systems Employing Co-located Antennas," *IEEE Trans. Microwave Theory and Techniques*, vol. 53, pp. 1837-1844, June 2005.

[Kot33] V. A. Kotel'nikov, "On the Transmission Capacity of "Ether" and Wire in Electrocommunications," *All-Union Energetics Committee*, Izd. Red. Upr. Svyazi RKKA, Moscow, Jan. 1933. Translation available online: http://ict.open.ac.uk/classics/1.pdf (Accessed 8 Oct. 2007).

[KRK05] S. Krusevac, P. Rapajic, and R. Kennedy, "Channel Capacity of Multi-Antenna Communication Systems with Closely Spaced Antenna Elements," *IEEE Personal, Indoor and Mobile Radio Communications (PIMRC 2005)*, vol. 4, pp. 2366-2370, Sept. 2005.

[LCV01] J. Ling, D. Chizhik, R. A. Valenzuela, "Predicting Multi-element Receive & Transmit Array Capacity Outdoors with Ray Tracing," *IEEE Vehicular Technology Conference*, vol. 1 , pp. 392-394, May 2001.

[LDBD03] M. Lienard, P. Degauque, J. Baudet, and D. Degardin, "Investigation on MIMO Channels in Subway Tunnels," *IEEE J. Selected Areas in Communications*, vol. 21, pp. 332-339, Apr. 2003.

[LK03] S. Loyka and A. Kouki, "Dimensionality Loss in MIMO Communication Systems," *3rd IASTED International Conference on Wireless and Optical Communications (WOC 2003)*, Banff, Alberta, Canada, pp. 138-143, July 2003.

[LL06a] G. Levin and S. Loyka, "Multi-Keyholes and Measure of Correlation in MIMO Channels," *23rd Biennial Symposium on Communications*, pp. 22-25, June 2006.

[LL06b] G. Levin and S. Loyka, "Multi-Keyhole MIMO Channels: Asymptotic Analysis of Outage Capacity," *IEEE International Symposium on Information Theory*, pp. 1305-1309, July 2006.

[LM06] S. Loyka and J. Mosig, "Information Theory and Electromagnetism: Are They Related?," in G. Tsoulos Ed., *MIMO System Technology for Wireless Communications*, Chapter 3, CRC Press, 2006.

[Loy05] S. Loyka, "Multiantenna Capacities of Waveguide and Cavity Channels," *IEEE Trans. Vehicular Technology*, vol. 54, pp. 863-872, May 2005.

[LP62] H. Landau and H. Pollak, "Prolate Spheroidal Wave Functions, Fourier Analysis and Uncertainty: Part III: the Dimension of the Space of Essentially Time- and Band-limited Signals," *Bell System Technical Journal*, vol. 41, pp. 1295-1336, July 1962.

[Mar01] M. Martone, *Multiantenna Digital Radio Transmission*, Artech House, 2001.

[Mey00] R. P. Meys, "A Summary of the Transmitting and Receiving Properties of Antennas," *IEEE Antennas and Propagation Magazine*, vol. 42, pp. 49-53, June 2000.

[MH91] J. McKown and R. Hamilton Jr., "Ray Tracing as a Design Tool for Radio Networks," *IEEE Network Magazine*, vol. 5, no. 6, pp. 27-30, Nov. 1991.

[Mig06] M. D. Migliore, "On the Role of the Number of Degrees of Freedom of the Field in MIMO Channels," *IEEE Trans. Antennas Propagation*, vol. 54, pp. 620-628, Feb. 2006.

[Mil00] D. A. B. Miller, "Communicating with Waves Between Volumes: Evaluating Orthogonal Spatial Channels and Limits on Coupling Strengths," *Appl. Optics*, vol. 39, pp. 1681-1699, Apr. 2000.

[Miy59] H. Miyakawa, "Sampling Theorem of Stationary Stochastic Variables in Multi-Dimensional Space," *J. Inst. Elec. Commun. Engrs*, (in Japanese), vol. 42, pp. 421-427, 1959.

[MJW05] M. Morris, M. Jensen, and J. Wallace, "Superdirectivity in MIMO Systems," *IEEE Trans. Antennas Propagation*, vol. 53, pp. 2850 - 2857, Sept. 2005.

[Mol05] A. F. Molisch, "Ultrawideband Propagation Channels-Theory, Measurement, and Modeling," *IEEE Trans. Vehicular Technology*, vol. 54, pp. 1528-1545, Sept. 2005

[Nyq28] H. Nyquist, "Certain Topics in Telegraph Transmission Theory," *Trans. AIEE*, vol. 47, pp. 617-644, 1928. Available online: http://www.loe.ee.upatras.gr/Comes/Notes/Nyquist.pdf (Accessed 8 Oct. 2007).

[PBT05] A. S. Y. Poon, R. W. Brodersen, and D. N. C. Tse, "Degrees of Freedom in Multiple-Antenna Channels: a Signal Space Approach," *IEEE Trans. Information Theory*, vol. 51, pp. 523-536, Feb. 2005.

[PGN03] A. Paulraj, D. Gore, and R. Nabar, *Introduction to Space-Time Wireless Communications*, Cambridge University Press, 2003.

[PM62] D. P. Petersen and D. Middleton, "Sampling and Reconstruction of Wave-Number-Limited Functions in N-Dimensional Euclidean Spaces," *Information and Control*, vol. 5, pp. 279-323, 1962.

[PM00] R. Piestun and D. A. B. Miller, "Electromagnetic Degrees of Freedom of an Optical System," *Optical Society of America*, vol. 17, pp. 892-902, May 2000.

[RC98] G. G. Raleigh and J. M. Cioffi, "Spatio-Temporal Coding for Wireless Communication," *IEEE Trans. Comm.*, vol. 46, pp. 357-366, Mar. 1998.

[RGK+07] A. Rajagopalan, G. Gupta, A. S. Konanur, B. Hughes, and G. Lazzi, "Increasing Channel Capacity of an Ultrawideband MIMO System Using Vector Antennas," *IEEE Trans. Antennas Propagation*, vol. 55, pp. 2880-2887, Oct. 2007.

[RWV94] S. Ramo, J. R. Whinnery, and T. Van Duzer, *Fields and Waves in Communication Electronics*, John Wiley & Sons, 1994.

[SBY+06] T. K. Sarkar, S. Burintramart, N. Yilmazer, S. Hwang, Y. Zhang, A. De, and M. Salazar-Palma, "A Discussion about Some of the Principles/Practices of Wireless Communication under a Maxwellian Framework," *IEEE Trans. Antennas Propagation*, vol. 54, pp. 3727-3745, Dec. 2006.

[SFGK00] D. Shiu, G. Foschini, M. Gans, and J. Kahn, "Fading Correlation and its Effect on the Capacity of Multi-element Antenna System," *IEEE Trans. Commun.*, vol. 48, pp. 502-513, Mar. 2000.

[SGWJ01] A. Swindlehurst, G. German, J. Wallace, and M. Jensen, "Experimental Measurements of Capacity for MIMO Indoor Wireless Channels," *IEEE 3rd Workshop on Signal Processing Advances in Wireless Communications (SPAWC01)*, pp. 30-33, Mar. 2001.

[Sha49] C. E. Shannon, "Communication in the Presence of Noise," *Proc. IRE*, vol. 37, pp. 10-21, 1949. Available online: http://www.stanford.edu/class/ee104/shannonpaper.pdf (Accessed 8 Oct. 2007).

[SJW04] T. Svantesson, M. A. Jensen, and J. W. Wallace, "Analysis of Electromagnetic Field Polarizations in Multiantenna Systems," *IEEE Trans. Wireless Comm.*, vol. 3, pp. 641-646, Mar. 2004.

[Sle65] D. Slepian, "Some Asymptotic Expansions for Prolate Spheroidal Wave Functions," *J. Math. and Physics*, vol. 44, pp. 99-140, 1965.

[Sle83] D. Slepian, "Some Comments on Fourier Analysis, Uncertainty and Modeling," *SIAM Rev.*, vol. 25, pp. 379-393, July 1983.

[SP61] D. Slepian and H. Pollak, “Prolate Spheroidal Wave Functions, Fourier Analysis and Uncertainty: Part I,” *Bell System Technical Journal*, vol. 40, pp. 43-63, Jan. 1961.

[SSEV06] J. Salo, P. Suvikunnas, H. M. El-Sallabi, and P. Vainikainen, “Ellipticity Statistic as a Measure of MIMO Multipath Richness,” *IEE Electron. Lett.*, vol. 42, no. 3, pp. 160-161, Feb. 2006.

[SSWB03] T. K. Sarkar, M. Salazar-Palma, M. Wicks, and R. J. Bonneau, *Smart Antennas*, John Wiley & Sons, 2003.

[Str41] J. A. Stratton, *Electromagnetic Theory*, McGraw-Hill, 1941.

[Str88] G. Strang, *Linear Algebra and Its Applications*, Harcourt Brace Jovanovich, 1988.

[SV87] A. Saleh and R. Valenzuela, “A Statistical Model for Indoor Multipath Propagation,” *IEEE J. Selected Areas in Communications*, vol. SAC-5, pp. 128-137, Feb. 1987.

[SZM+06] M. Shafi, M. Zhang, A. L. Moustakas, P. J. Smith, A. F. Molisch, F. Tufvesson, and S. H. Simon, "Polarized MIMO Channels in 3-D: Models, Measurements and Mutual Information," *IEEE J. Selected Areas in Communications*, vol. 24, pp. 514-527, Mar. 2006.

[Tel95] I. E. Telatar, “Capacity of Multi-Antenna Gaussian Channels,” *AT&T Bell Laboratories, Lucent Technologies, Internal Technical Memorandum*, Oct. 1995. Available online:
http://mars.bell-labs.com/papers/proof (Accessed 17 Oct. 2007).
Published in *European Transactions on Telecommunications*, vol. 10, pp. 585-595, Nov/Dec 1999.

[Tor55] G. Toraldo di Francia, “Resolving Power and Information,” *J. Opt. Soc. Am.*, vol. 45, pp. 497-501, 1955.

[Tor69] G. Toraldo di Francia, “Degrees of Freedom of an Image,” *J. Opt. Soc. Am.*, vol. 59, pp. 799-804, 1969.

[TVD98] R. Torres, L. Valle, and M. Domingo, “Computer Tool to Analyze Radio Channel in Arbitrary Enclosed Spaces using Ray Tracing,” *IEEE Vehicular Technology Conference*, vol. 1, pp. 581-585, May 1998.

[TVDD99] R. Torres, L. Valle, M. Domingo, and M. Diez, “CINDOOR: an Engineering Tool for Planning and Design of Wireless Systems in Enclosed Spaces,” *IEEE Antennas and Propagation Magazine*, vol. 41, no.4, pp. 11-22, Aug. 1999.

[TVDL99] R. Torres, L. Valle, M. Domingo, and S. Loredo, “An Efficient Ray-Tracing Method for Radio Propagation Based on the Modified BSP Algorithm,” *IEEE Vehicular Technology Conference*, vol. 4, pp. 1967-1971, Sept. 1999.

[Whi15] E. T. Whittaker, “On the Functions Which Are Represented by the Expansions of the Interpolation Theory,” *Proc. Roy. Soc. Edinburgh*, Sect. A, vol. 35, pp. 181-194, 1915.

[Win87] J. H. Winters, “On the Capacity of Radio Communication Systems with Diversity in a Rayleigh Fading Environment,” *IEEE J. Selected Areas in Communications*, vol. 5, pp. 871–878, June 1987.

[WJ02] J. Wallace and M. Jensen, “Modeling the Indoor MIMO Wireless Channel,” *IEEE Trans. Antennas Propagation*, vol. 50, pp. 591-599, May 2002.

[WSC00] Y. Wang, S. Safavi-Naeini, and S. K. Chaudhuri, "A Hybrid Technique Based on Combining Ray Tracing and FDTD Methods for Site-Specific Modeling of Indoor Radio Wave Propagation," *IEEE Trans. Antennas Propagation*, vol. 48, pp.743-754, May 2000.

[XCV04] Hao Xu, D. Chizhik, and R. Valenzuela, "A Generalized Space-Time Multiple-Input Multiple-Output (MIMO) Channel Model," *IEEE Trans. Wireless Comm.*, vol. 3 , no. 3 , pp. 966-975, May 2004.

[XJ06] J. Xu and R. Janaswamy, "Electromagnetic Degrees of Freedom in 2-D Scattering Environments," *IEEE Trans. Antennas Propagation*, vol. 54, pp. 3882-3894, Dec. 2006.

[YIZ04] Z. Yun, M.F. Iskander, and Z. Zhijun, "Complex-Wall Effect on Propagation Characteristics and MIMO Capacities for an Indoor Wireless Communication Environment," *IEEE Trans. Antennas Propagation*, vol. 52, pp.914-922, Apr. 2004.

[ZFDW00] T. Zwick, C. Fischer, D. Didascalou, and W. Wiesbeck, "A Stochastic Spatial Channel Model Based on Wave-Propagation Modeling," *IEEE J. Selected Areas in Communications*, vol. 18, pp. 6-15, Jan. 2000.

[ZFW02] T. Zwick, C. Fischer, and W. Wiesbeck, "A Stochastic Multipath Channel Model Including Path Directions for Indoor Environments," *IEEE J. Selected Areas in Communications*, vol. 20, pp. 1178-1192, Aug. 2002.

List of Symbols and Notation

$\mathbf{M}$	Boldface upper case denotes a matrix
m_{ij}	Subscripted lower case denotes a scalar entry within $\mathbf{M}$ (row i and column j)
$[m_{ij}]$	Matrix constructed from the entries m_{ij}
$\bar{\mathbf{D}}$	Barred boldface upper case denotes a dyad
$\mathbf{v}$	Boldface lower case denotes a vector (in the exception of $\overline{E}$, $\overline{H}$, $\overline{A}$ and $\overline{F}$)
$[v_k]$	Vector constructed from the components v_k
$\hat{\mathbf{v}}$	Unit vector
$\overline{E}$	Electric field vector
$\overline{H}$	Magnetic field vector
$\overline{A}$	Magnetic vector potential
$\overline{F}$	Electric vector potential
$\bar{\nabla}\times\mathbf{M}$	Dyadic curl operating on the column vectors of $\mathbf{M}$
$\mathbb{C}^{m\times n}$	Set of $m-\text{by}-n$ complex matrices
diag($\mathbf{v}$)	Diagonal matrix whose diagonal entries are those of $\mathbf{v}$
$\sigma\{\bullet\}$	Singular values of a matrix
σ_i	i^{th} singular value
$N_p(\bullet)$	Schatten p-norm, $N_p(\mathbf{M}) \equiv \left(\sum_i \left(\sigma_i \{\mathbf{M}\} \right)^p \right)^{1/p} \quad 1 \le p < \infty$
$\|\bullet\|_{tr}$	Trace norm (Schatten 1-norm)
$\|\bullet\|_F$	Frobenius norm (Schatten 2-norm)

$\otimes$	Kronecker product (also called direct, tensor or outer product). For $\mathbf{A} \in \mathbb{C}^{m \times n}$ and $\mathbf{B} \in \mathbb{C}^{p \times q}$, $\mathbf{A} \otimes \mathbf{B} \equiv \begin{bmatrix} a_{11}\mathbf{B} & \cdots & a_{1n}\mathbf{B} \\ \vdots & \ddots & \vdots \\ a_{m1}\mathbf{B} & \cdots & a_{mn}\mathbf{B} \end{bmatrix} \in \mathbb{C}^{mp \times nq}$.
$\lfloor x \rfloor$	Largest integer $\leq x$
$\lceil x \rceil$	Smallest integer $\geq x$
det(**M**)	Determinant of a matrix
$\{\bullet\}^T$	Transpose operation
$\{\bullet\}^H$	Conjugate transpose operation
$\{\bullet\}^*$	Complex conjugate operation
$\widetilde{(\bullet)}$	Fourier transform of a scalar or vector function
Re{•}	Real part
Im{•}	Imaginary part
$\langle y_1, y_2 \rangle$	Inner product of the functions y_1 and y_2
θ	Elevation angle
φ	Azimuth angle
δ_{mn}	Kronecker delta
$\delta(\bullet)$	Delta function
η_0	Free space impedance
k_0	Free space wave number
λ	Free space wavelength
ω	Angular temporal frequency
ε_0	Free space permittivity
μ_0	Free space permeability

List of Acronyms and Nomenclatures

AOA	Angle of Arrival
AOD	Angle of Departure
BC	Boundary Conditions
BER	Bit Error Rate
BFN	Beamforming Network
BW	Bandwidth
CSI	Channel State Information
DOA	Direction of Arrival
DOD	Direction of Departure
DOF	Degrees of Freedom
ED	Effective Dimensionality
EDOF	Effective Degrees of Freedom
EM	Electromagnetic
ES	Ellipticity Statistic
FDTD	Finite Difference Time Domain
FED	Field Expansion Diversity
FT	Fourier Transform
Hexapole	Collocated electric and magnetic polarized point radiators making 6 independent ports
iid	Independent Identically Distributed
IRT	Image Ray Tracing
LOS	Line of Sight
LT	Loss Tangent
MIMO	Multiple Input Multiple Output
PC	Phase Centre
PEC	Perfect Electric Conductor
PID	Power Independent Dimensionality

PIEDOF	Power Independent Effective Degrees of Freedom
PSWF	Prolate Spheroidal Wave Function
PWA	Plane Wavefront Approximation
ROE	Region of Existence
Rx	Receiver
SISO	Single Input Single Output
SNR	Signal to Noise Ratio
SV	Singular Values
SVD	Singular Values Decomposition
TM	Transverse Magnetic
Tripole	Tri-polarized collocated point radiators (electric or magnetic) making 3 independent ports
Tx	Transmitter

"*... apprendre n'est pas savoir; il y a les sachants et les savants: c'est la mémoire qui fait les uns, c'est la philosophie qui fait les autres... La philosophie ne s'apprend pas; la philosophie est la réunion des sciences acquises au génie qui les applique...* "

L'abbé Faria, Le Comte de Monte-Cristo, Chapitre XVII, Alexandre Dumas père, 1844.

"*... to learn is not to know; there are the knowledgeable ones and the scientists. Memory makes the one, philosophy the other... Philosophy cannot be taught; philosophy is the reunion of the acquired sciences to the genie who applies them...*"